Title
Design and application of compliant III-nitride substrates using Porous GaN

Permalink
https://escholarship.org/uc/item/7w23f733

Author
Pasayat, Shubhra Shweta

Publication Date
2021

UNIVERSITY OF CALIFORNIA
Santa Barbara

Design and application of compliant III-nitride substrates using Porous GaN

A dissertation submitted in partial satisfaction of the
requirements for the degree Doctor of Philosophy
in Electrical and Computer Engineering

by

Shubhra Shweta Pasayat

Committee in charge:
Professor Umesh K Mishra, Chair
Professor Steven P DenBaars
Professor Shuji Nakamura
Professor Robert McMeeking
Dr Stacia Keller

June 2021

The dissertation of Shubhra Shweta Pasayat is approved.

Steven P. DenBaars

Shuji Nakamura

Robert McMeeking

Stacia Keller

Umesh K. Mishra, Committee Chair

May 2021

Design and application of compliant III-nitride substrates using Porous GaN

by

Shubhra Shweta Pasayat

DEDICATIONS

To my parents Kishore Kumar Pasayat and Sabita Pasayat for their endless love, support, and encouragement.

To my late paternal grandma Sarala, for her unparalleled emotional acumen, Maa your bedtime stories are dearly missed.

To my brother and sister-in-law for choosing the noblest profession of all and touching countless lives.

To my husband, for believing in me more than I did.

To the makers of the movie “Kung Fu Panda” for some invaluable life lessons.

ACKNOWLEDGEMENTS

My experience during graduate school at UCSB has been immensely enjoyable and during this time I have met numerous people who have collectively made this a memorable journey.

First, I would like to thank my advisor, Prof. Umesh K. Mishra for accepting me in his group and his continuous guidance every step of the way. He has always inspired me to push my boundaries, explore uncharted territories and continue learning. Our research group is lucky to have him as an advisor who is the epitome of perseverance, optimism, curiosity and excellence. I am also indebted to Dr Stacia Keller for introducing the electrical engineer in me to the fascinating world of crystal growth. Her unwavering support in risk assessment, experiment design and manuscript writing have shaped the core of my research personality. I would also like to thank Prof. Steven P. DenBaars and Prof. Shuji Nakamura for their insightful comments, direction and for helping in evaluating this substrate technology for optoelectronics devices especially long wavelength LEDs. I would also like to thank Prof. Robert McMeeking for his help in understanding the mechanics behind the substrates we designed which equipped us with the necessary ammunition to take this technology forward.

I would also like to thank the funding sources who made this project a reality: Office of Naval Research monitored by Dr. Paul Maki, the Szilagyi Energy Breakthrough Fellowship monitored by the Institute for Energy Efficiency at UC Santa Barbara, the Solid State Lighting and Energy Electronics Centre at UC Santa Barbara and the Google micro-LED grant monitored by Dr Aurelien David. Without their support, I won’t have been able to spend countless hours in the cleanroom or the x-ray lab characterizing my wafers. I would also like to thank the MRL staff members – Dr Feng Wu, Dr Tom Mates, Dr Youli Li and

Aidan Taylor, for their support with material characterization. Special thanks to Prof. Mike Gordon for welcoming me into his lab-space for micro-LED characterization.

Next, I would like to thank my colleagues at Mishra group with direct contribution towards this dissertation work – Chirag, Weiyi and Nirupam. It was fun developing this technology with your support. Special thanks to Weiyi for our countless discussions on authentic Sichuan cuisine, restaurants, and cooking. Onur, Brian R., Chirag and Matt G. for training me in the cleanroom, HFM lab and helping me understand device physics. Special thanks to Chirag for designing my micro-LED masks, helping me with course selections and mentoring me through the screening exam preparation. Yusuke, Haoran and Nirupam for training me on MOCVD reactors and teaching me the basics of growths. My colleagues from DenBaars and Nakamura group – Matt W. and Ryan L., for teaching me the fundamentals of micro-LED fabrication and characterization, helping me achieve swift device level demonstrations and record data acquisition possible. My interns Dillon, Yifan and Raina for performing tons of material and device characterizations. The entire nanofabrication facility staff for help with keeping the tools up and running for us all to perform our experiments.

I would also like to thank all MO5 growers – Abdullah, Caroline, Cheyenne, Chris, Hongjian, Jake, Jared, Michel, Nate, Panpan, Pavel, Ryan W., Ryan A., Vineetha, Yichao and Yusuke, for holding each other’s hands through the whole journey especially the reactor body upgrade in the summer of 2019. That was an extremely humbling experience, and we learned so much about the reactor. The coordination and problem-solving skills demonstrated by you all is unmatched. The support staff Mike, David and Brian C. have been exceptional in keeping the lab up and running.

I would also like to thank the rest of the Mishra group members for being extremely supportive and creating a fun environment to work in – Aditya R., Anchal, Athith, Christian, Christopher, Cory, Elaheh, Emmanuel, Emre, Henry, Islam, Pawana, Robert, Silvia, Steven, Wenjian and Xun. There is never a dull moment in the student office. Special thanks to Steven for his bravery in enduring my wedding and trying out the authentic local cuisine in India, your bollywood dance moves were on point!

I am grateful to my friends – Aditya D., Akshar, Anant, Anchal S., Divya, Geetak, Harsha, Hsing-Ying, Manik, Padma, Prashansa, Rohan and Stephanie, for making my life at Santa Barbara enjoyable through game nights, movie marathons, birthday celebrations and road trips. Special thanks to Prashansa for staying up with me multiple nights to clear out layout errors during chip design course and designing electromigration aware circuits.

I am greatly indebted to my parents (Kishore and Sabita), grandparents, brother (Parth), sisters-in-law (Swati and Paridhi), parents-in-law (Shivraj and Usha) for their continuous support. Finally, my husband, colleague, mentor, friend and confidant, Chirag, for teaching me the art of relaxation and always being there for me, always!

VITA OF SHUBHRA SHWETA PASAYAT
April 2021

EDUCATION

Ph.D., Electrical and Computer Engineering **2021**

University of California, Santa Barbara

M.S., Electrical and Computer Engineering **2019**

University of California, Santa Barbara

B.Tech., Electronics and Electrical Comm. Engrg. **2013**

Indian Institute of Technology (I.I.T.), Kharagpur

WORK EXPERIENCE

Graduate Student Researcher **Sept. 2015- Apr. 2021**

Dept. of Electrical & Computer Engineering, University of California, Santa Barbara
- Epitaxy and Process design, material growth (MOCVD), fabrication, and characterization of long wavelength (>500nm) InGaN/GaN Micro-LEDs sized between 3-10 µm
- Led the fundamental strain-relaxation research effort at UCSB in III-N materials to boost the performance of both electronic and optoelectronic devices beyond conventional design
- Part of multiple research projects involving InGaN/GaN LEDs and AlGaN/GaN HEMTs

Major highlights:

- Demonstrated the first InGaN red (632nm) micro-LED sized < 10 µm with measurable on-wafer EQE
- Invented and developed porous GaN-based compliant pseudo-substrates
- First demonstration of micron-scale elastic strain relaxation in III-N MOCVD materials

ASIC Verification Engineer (Summer Intern) **Jun. 2016-Sept. 2016**

Infinera Corporation, Sunnyvale, CA, USA
Framer Verification IP (VIP) optimization
- Flattened the hierarchy at the UVM component level, to speed up the verification environment.

- Reduced code complexity by 41% with a simulation time decrease of 14% in the full chip simulation
- Ensured backward compatibility, scalability, and portability of the new VIP

Senior Hardware Verification Engineer (Full-time) Apr. 2015-Aug. 2015

Memory Solutions team, Samsung R&D Institute, Bangalore, India
Controller module verification

- Owned functional verification, code and functional coverage analysis of Transport layer, Data Link Layer and PHY-Adapter Layer of MIPI-UNIPRO compliant Controller IP modules
- Owned regression analysis and debugging using third party Verification IPs for the same
- Automated regression environment creation using Python

Hardware Verification Engineer (Full time) Jun. 2013-Mar. 2015

Visual Display team, Samsung R&D Institute, Bangalore, India
Benchmarking and VIP creation

- Owned the ARM CPU Performance verification project involving Baremetal Benchmark set up and performance measurement
- Co-created OCP 2.0 UVC VIP: covering read, write, and handshake functionality

Undergraduate Researcher Aug. 2012-May. 2013

Indian Institute of Technology, Kharagpur

- Simulation and analytical modelling of Multi-junction InGaN/GaN based Blue LEDs to achieve an optimal LED structure using Silvaco-Blaze and MATLAB

PATENT APPLICATIONS

- S. Keller, U. K. Mishra, **S. S. Pasayat** and C. Gupta, "Advances in the use of porous materials for the fabrication of materials with arbitrary lattice constant", U.S. Provisional Patent Appl. Number: 62/962113, filed on 16th Jan. 2020.

- **S. S. Pasayat**, C. Gupta, S. Keller and U. K. Mishra, "Methods for achieving monolithic integration of color tunable light emitting diodes (LEDs) without etch damage or with minimal etch damage and including an improved method for relaxing semiconductor films for the fabrication of pseudo-substrates", U.S. Provisional Patent Appl. Number: 62/927,486, filed on 29th Oct. 2019.

- S. Keller, U. K. Mishra, **S. S. Pasayat** and C. Gupta, "Method for relaxing semiconductor films including the fabrication of pseudo-substrates and addition of previously un-accessible functionality to group III–nitrides", U.S. Provisional Patent Appl. Number: 62/898,178, filed on 10th Sept. 2019.

HONORS & AWARDS

- Qualcomm Innovation Fellowship finalist (Adv. Semiconductor Electronics) 2020
  Qualcomm Inc.
- Outstanding Teaching Assistant Award 2020
  UC Santa Barbara
- Facebook Research Fellowship finalist (AR/VR photonics and Optics) 2020
  Facebook Research
- Outstanding Graduate Student Research Achievement Award 2019
  Solid State Lighting and Energy Electronics Centre (UC Santa Barbara)
- Szilagyi Energy Breakthrough Fellowship 2019
  Institute of Energy Efficiency (UC Santa Barbara)
- Samsung Spot Award 2015
  Samsung R&D Institute, Bangalore, India
- Winner of Samsung Gear App Challenge 2014
  Samsung Electronics
- Gymkhana Award 2013
  I.I.T. Kharagpur
- Young Blood Award 2011
  Gopali Youth Welfare Society (NGO), for generating $10K in funds towards school construction for underprivileged children in India
- Gold medallist, Table Tennis 2010
  46th Inter-IIT sports meet, I.I.T. Delhi
- All India Rank 540 (out of ~400,000 students) 2009
  Indian Institute of Technology-Joint Entrance Examination 2009

INVITED TALK

- **S. S. Pasayat** "III-Nitride Strain relaxation enabled by Porous GaN for optoelectronic applications" *SPIE Photonic West*, Mar. 2021, San Francisco, CA, USA. https://doi.org/10.1117/12.2577008

JOURNAL PUBLICATIONS

- **S. S. Pasayat**, C. Gupta, M. S. Wong, R. Ley, M. J. Gordon, S. Nakamura, S. P. DenBaars, S. Keller and U. K. Mishra "Demonstration of ultra-small (< 10μm)

632nm red InGaN micro-LEDs with useful on-wafer external quantum efficiency (> 0.2%) for mini-displays", *Applied Physics Express*, vol. 14, no. 1 (2021). DOI : https://doi.org/10.35848/1882-0786/abd06f

- **S. S. Pasayat**, R. Ley, C. Gupta, M. S. Wong, C. Lynsky, Y. Wang, M. J. Gordon, S. Nakamura, S. P. DenBaars, S. Keller and U. K. Mishra "Color-tunable <10 μm square InGaN micro-LEDs on compliant GaN-on-porous-GaN pseudo-substrates", *Applied Physics Letters,* vol. 117, no. 6 (2020). DOI : https://doi.org/10.1063/5.0011203

- **S. S. Pasayat**, N. Hatui, W. Li, C. Gupta, S. Nakamura, S. P. DenBaars, S. Keller and U. K. Mishra "Method of growing elastically relaxed crack-free AlGaN on GaN as substrates for ultra-wide bandgap devices using porous GaN", *Applied Physics Letters,* vol. 117, no. 6 (2020). DOI : https://doi.org/10.1063/5.0017948

- **S. S. Pasayat**, C. Gupta, M. S. Wong, Y. Wang, S. Nakamura, S. P. DenBaars, S. Keller and U. K. Mishra "Growth of strain-relaxed InGaN on micron-sized patterned compliant GaN pseudo-substrates", *Applied Physics Letters,* vol. 116, no. 11 (2020). DOI : https://doi.org/10.1063/5.0001480

- **S. S. Pasayat**, C. Gupta, Y. Wang, S. P. DenBaars, S. Nakamura, S. Keller and U. K. Mishra, "Compliant micron-sized patterned InGaN pseudo-substrates utilizing porous GaN", *Materials,* vol. 13, No. 1 (2020). DOI : https://doi.org/10.3390/ma13010213

- **S. S. Pasayat**, C. Gupta, D. A. James, D. Cohen, S. P. DenBaars, S. Nakamura, S. Keller and U. K. Mishra, "Fabrication of relaxed InGaN pseudo-substrates composed of micron-sized pattern arrays with high fill factors using porous GaN", *Semiconductor Science and Technology,* vol. 34, No. 11 (2019) DOI: https://doi.org/10.1088/1361-6641/ab4372.

- **S. S. Pasayat**, C. Lund, Y. Tsukada, M. Catalano, L. Wang, M. J. Kim, S. Nakamura, S. Keller and U. K. Mishra, "Optimization of digital growth of thick N-polar InGaN by MOCVD", *Journal of Electronic Materials,* vol. 49, no. 6 (2019). DOI: https://doi.org/10.1007/s11664-019-07875-3.

- **S. S. Pasayat**, E. Ahmadi, B. Romanczyk, O. Koksaldi, A. Agarwal, M. Guidry, C. Gupta, C. Wurm, S. Keller, U. K Mishra, "First demonstration of RF N-polar GaN MIS-HEMTs grown on Bulk GaN using PAMBE", *Semiconductor Science and Technology,* vol. 34, No. 4. (2019). DOI: https://doi.org/10.1088/1361-6641/ab0761.

- W. Li, **S. S. Pasayat**, M. Guidry, B. Romanczyk, X. Zheng, C. Gupta, N. Hatui, S. Keller and U. K. Mishra, "First experimental demonstration and analysis of electrical transport characteristics of a GaN-based HEMT with a relaxed InGaN channel", *Semiconductor Science and Technology,* vol. 35, no. 7 (2020). DOI: https://doi.org/10.1088/1361-6641/ab860a

- P. Shrestha, M. Guidry, B. Romanczyk, N. Hatui, C. Wurm, A. Krishna, **S. S. Pasayat,** R. R. Karnaty, S. Keller, J. F. Buckwalter and U. K. Mishra, "High Linearity and High Gain Performance of N-Polar GaN MIS-HEMT at 30 GHz", *Electron Device Letters,* vol. 41, no. 5 (2020). DOI: https://doi.org/10.1109/LED.2020.2980841

- C. Gupta, Y. Tsukada, B. Romanczyk, **S. S. Pasayat**, D. A. James, E. Ahmadi, S. Keller and U. K. Mishra, "First demonstration of improvement in hole conductivity in c-plane III-Nitrides through application of uniaxial strain", *Japanese Journal of Applied Physics,* vol. 58, No. 3. (2019) DOI: https://doi.org/10.7567/1347-4065/aaffaa.

- C. Gupta, S. H. Chan, **S. S. Pasayat**, S. Keller and U. K. Mishra, "Reverse breakdown studies of GaN MOSCAPs and their implications in vertical GaN power devices", *Journal of Applied Physics,* vol. 125, No. 12 (2019). DOI: https://doi.org/10.1063/1.5082652.

CONFERENCE PRESENTATIONS

- **S. S. Pasayat**, N. Hatui, W. Li, C. Gupta, S. P. DenBaars, S. Nakamura, S. Keller and U. K. Mishra, "Growth of high quality crack-free partially relaxed thick $Al_{0.24}Ga_{0.76}N$ on porous GaN based GaN pseudo-substrates", *Electronic Material Conference,* Jun. 2020, Virtual Conference.

- **S. S. Pasayat**, C. Gupta, M. S. Wong, Y. Wang, S. Nakamura, S. P. DenBaars, S. Keller and U. K. Mishra, "Compliant GaN pseudo-substrates for the growth of relaxed InGaN base layers demonstrated through long wavelength (>540nm) micro-LEDs (< 10µm)", accepted for oral presentation at *8th International Symposium on Growth of III-Nitrides,* May 2020, San Diego, CA, USA.

- **S. S. Pasayat**, C. Gupta, D. A. James, D. Cohen, S. Nakamura, S. DenBaars, S. Keller and U. K. Mishra, "InGaN Relaxation via Porous GaN Enabling Longer Wavelength InGaN Luminescence", *13th International Conference on Nitride Semiconductors*, Jul. 2019, Bellevue, WA, USA (late news).

- **S. S. Pasayat**, C. Lund, Y. Tsukada, M. Catalano, M. J. Kim, S. Nakamura, S. Keller and U. K. Mishra, “Digital Growth of Smooth, High Quality Thick (200nm) N-Polar InGaN Films by MOCVD”, *61st Electronic Materials Conference*, Jun. 2019, Ann Arbor, MI, USA.

- **S. S. Pasayat,** A. Agarwal, C. Wurm, A. Krishna, X. Zheng, B. Romanczyk, C. Gupta, M. Guidry, S. Keller, and U. K. Mishra, “Impact of regrowth (on wet etched and dry etched interface) on the breakdown performance of N-polar GaN MIS-HEMTs”, *International Workshop on Nitride Semiconductors,* Nov. 2018, Kanazawa, Japan.

- **S. S. Pasayat**, E. Ahmadi, B. Romanczyk, O. Koksaldi, A. Agarwal, M. Guidry, C. Gupta, C. Wurm, S. Keller, U. K Mishra, “N-polar GaN HEMTs Grown on Bulk GaN Using PAMBE for Highly Efficient Mm-Wave Power Amplifiers”, *Compound Semiconductor Week,* May-Jun. 2018, Cambridge, MA , USA.

- P. Shrestha, M. Guidry, B. Romanczyk, R. R. Karnaty, N. Hatui, C. Wurm, A. Krishna, **S. S. Pasayat**, S. Keller, J. F. Buckwalter and U. K. Mishra, “ A novel concept using derivative superposition at the device-level to reduce sensitivity to bias in N-polar GaN MISHEMT”, *Device Research Conference,* Jun. 2020, Virtual Conference. DOI : https://doi.org/10.1109/DRC50226.2020.9135169

- W. Li, M. Guidry, **S. S. Pasayat**, B. Romanczyk, X. Zheng, C. Gupta, N. Hatui, S. Keller, and U. K. Mishra, “First Experimental Demonstration and Analysis of Electrical Transport Characteristics in GaN HEMT with a Relaxed InGaN Channel”, accepted for oral presentation at *GOMACTech-20 Conference,* Mar. 2020, San Diego, CA, USA.

- N. Hatui, **S. S. Pasayat**, A. Krishna, S. Nakamura, S. Keller and U. K. Mishra, “MOCVD process optimization for thick, semi-insulating N-polar InGaN layers”, *13th International Conference on Nitride Semiconductors*, Jul. 2019, Bellevue, WA, USA (late news).

- C. Gupta, Y. Tsukada, **S. S. Pasayat**, W. Liu, S. Keller and U. K. Mishra, “Strain-relaxation studies of thick (>100nm) and wide (>500nm) InGaN stripe arrays”, *13th International Conference on Nitride Semiconductors*, Jul. 2019, Bellevue, WA, USA.

- C. Gupta, Y. Tsukada, B. Romanczyk, **S. S. Pasayat**, D. A. James, S. Keller and U. K. Mishra, “First experimental demonstration of enhancement in hole conductivity in c-plane (0001) III-Nitrides with uniaxial strain”, *International Workshop on Nitride Semiconductors,* Nov. 2018, Kanazawa, Japan.

- B. Romanczyk, H. Li, M. Guidry, E. Ahmadi, A. Agarwal, X. Zheng, **S. S. Pasayat**, S. Keller, and U. K. Mishra, “mm-Wave N-Polar GaN Deep Recess MISHEMT Delivering Over 7 W/mm and 25% Power-Added Efficiency at 94 GHz”, *Compound Semiconductor Week,* May 2017, Berlin, Germany.

ABSTRACT

Design and application of compliant III-nitride substrates using Porous GaN

by

Shubhra Shweta Pasayat

With the invention of efficient Gallium Nitride (GaN) based blue light emitting diodes (LEDs), the lighting sector has been revolutionized. The blue light is converted into white using a yellow phosphor coating. These white light sources are currently being heavily utilized in the backlight units of liquid crystal displays (LCDs) in residential and commercial settings. This white light goes through various stages such as multiple polarizers, liquid crystals, and color filters, leading to a reduced light output. Recently, organic LEDs have emerged as a premium display technology due to their self-emissive nature, leading to extremely high contrast ratio and improved overall efficiency. However, due to their organic nature they are susceptible to degradation over time and require sophisticated encapsulation due to their sensitivity to moisture and oxygen. Hence, the use of self-emissive inorganic LEDs is highly desired which will have extremely high contrast ratio and at the same time have very high lifetime, brightness, and efficiency. For the three basic colors red, green and blue, different materials are preferred. The Indium Gallium Nitride (InGaN) alloy system spans a bandgap of 0.7 – 3.4 eV covering the full visible spectrum. However, only blue and green emitting InGaN LEDs are preferred by display manufacturers, as the efficiency of InGaN LEDs emitting beyond green in the visible spectrum reduces drastically. The higher indium content necessary to emit light in the longer wavelength of emission is accompanied

by a lot of defects. As InN and GaN have a 10% lattice mismatch, the increased indium content increases the strain in the epitaxial structure causing defect formation. Hence, Aluminum Indium Gallium phosphide (AlInGaP) based red emitters are preferred as they offer very high efficiency in the red emission range.

To facilitate cost effective commercialization and provide an immersive user experience in near eye displays, the inorganic LED sizes must be scaled to dimensions < 10 µm. Due to unfavorable material properties, scaling of the phosphide based red emitters is met with a lot of challenges. Hence, InGaN based scaled red emitters are needed.

Our approach was to target the strain in the epitaxial structure by utilizing a flexible underlayer that can be visualized as a strain reducing layer. The flexible material of our choice was porous GaN, which could be obtained using a doping selective electrochemical etching process. This etching process could convert the GaN:Si films into porous GaN films. Using this flexible underlayer, elastic strain relaxation was demonstrated for InGaN films in the micrometer scale regime, leading to very high-quality epitaxial layer growth. Prior demonstrations of elastic strain relaxation were in the nanometer scale regime, posing challenges in device fabrication. With this substrate technology, the first red micro-LED sized < 10 µm was demonstrated with measurable efficiency.

Beyond InGaN, the growth of relaxed AlGaN films was also pursued. 1.3 µm thick crack-free relaxed $Al_{0.2}Ga_{0.8}N$ was grown using these substrates. With continued development large area strain relaxed AlGaN with arbitrary lattice constant can be demonstrated, that can be utilized not only for AlGaN based UV-LEDs but also for AlGaN electronics applications.

TABLE OF CONTENTS

I. Introduction

Gallium Nitride (GaN) based devices are ubiquitous serving efficient energy conversion, efficient energy utilization and high data rate applications [1-3]. Owing to their high electron mobilities, wide and direct bandgap properties, GaN along with their alloys with Aluminum and Indium, are enabling devices that have the potential to serve almost all the needs of a futuristic lifestyle. GaN based efficient lighting has revolutionized the household lighting space [4]. Beyond the conventional lighting sector, they are also making inroads into automotive lighting, LIDAR, horticulture, LiFi, displays, light therapy and sanitization applications [5-13]. The direct bandgap property and ability to achieve highly efficient devices on foreign substrates, has led to the widespread adoption of this technology.

In this dissertation, the Indium, Gallium, Aluminum Nitride or (In,Ga,Al)-N material system has been explored for long wavelength light emission (beyond green) at ultra-small device dimensions for mini-displays. Currently different display technologies dominate the consumer electronics market, but certain roadblocks have led researchers to come up with alternatives using III-nitrides [14]. In this chapter, a brief discussion of the evolution of current displays will be discussed followed by the motivation for this research work.

A. Incumbent technologies – LCDs and OLEDs compared to micro-LEDs

Light emitting diodes or LEDs sized below 100 µm are called micro-LEDs, which are going to be discussed in detail in this dissertation. Table 1.1 briefs the size dependent nomenclature for LEDs. Micro-LEDs find application in a variety of consumer electronics applications such augmented reality (AR) headsets, virtual reality (VR) headsets, televisions (TV), smartwatches, smartphones, etc. Currently, Liquid Crystal Displays (LCDs) and

Organic Light Emitting Diodes (OLEDs) are the dominant display technologies in the market. LCDs cannot emit light themselves and hence need a light source. The emitted light then passes through liquid crystals, polarizers, and color filters to develop the colored images on the front screen. These displays traditionally utilized inefficient, bulky and large area fluorescent lamps as the light source in their backlight unit (BLU), which have now been replaced by more compact and efficient white LEDs. These white LEDs are blue InGaN LEDs covered with yellow phosphors. Even with efficient backlight capability these displays suffer from low efficiency overall due to the multiple stages that the light must traverse, resulting in only 5% of the light from the BLU escaping the display [15]. Nonetheless, LEDs have allowed one of the breakthrough techniques in displays called "Local Dimming" [16]. Suppose the image in fig. 1 was displayed on the screen, and the LED BLU consisted of a few devices spread across the screen. Ideally, the bottom right part of the image must be completely dark, and the rest of the image should be bright and colorful. If all the LEDs stay lit, then the darker part of the image may appear dark grey,

Nomenclature	Dimension
LED	> 500 µm
Mini-LED	100 – 500 µm
Micro-LED	< 100 µm

Table 1.1 Nomenclature for LEDs based on size

Display technique	LCD	OLED	MicroLED
Technological type	Backlit/LED	Self emissive ☑	Self emissive ☑
Contrast ratio	5000 : 1	∞ ☑	∞ ☑
Lifetime	Medium	Medium	Long ☑
Response time	Millisecond	Microsecond	Nanosecond ☑
Operational temperature	-40 to 100 °C	-30 to 85 °C	-100 to 120 °C ☑
Cost	Low ☑	Medium	High
Power consumption	High	Medium	Low ☑

Table 1.2 Comparison between different display technologies

Figure 1.1 Butterfly Beach, Montecito CA | Image - @alexfrenchman

which is not desired. Local dimming allows for the LEDs to be dimmed in the darker part of the image resulting in an overall higher picture quality. In this regard the oldest technology is called the “direct backlit” type, wherein a few large LEDs were placed at the back of the display which were lit up or dimmed all together. This leads to dark images looking too dark and light images looking too light. These can be found in some of the lowest range LCD TVs and they do not have the capability of local dimming at all. More commonly found are the “edge-lit” kind wherein LED stripes are placed either on the top/bottom or either sides or even all the way around. The light from these stripes on the edge of the displays is directed towards the entire screen using light guiding plates and mirrors. These can enable local dimming, but since the light source is at the edge, the dimming may affect more parts of the image than it should. The state-of-the-art LCD displays have “Full array local dimming” capability, which have many smaller LEDs or mini-LEDs, facilitating various dimming zones, hence a better control over local dimming. These displays are also quite low cost and offer very high brightness of > 1000 nits (cd/m^2), due to the presence of highly efficient phosphor covered blue LEDs in the BLU. Despite these advances, these displays only allow for dimming the darker parts of the images and not complete turn-off, as enabled by self-emissive displays like OLEDs. This leads to very low contrast ratios of ~ 5000:1 (Table 1.2) in these displays leading to a low dynamic range, suppressing a lot of information in the reproduced image. Additionally, the slower response of liquid crystals to change in bias conditions leads to larger response times for these displays, which is undesirable for time-critical applications.

OLEDs have changed the display landscape and are being considered the most premium displays right now [17]. Due to their self-emissive nature, the number of components in the display reduce drastically comprising of contacts, the LEDs and encapsulation layer. Due to the absence of multiple stages of light transmission, the overall efficiency of these displays rely heavily on the efficiencies of the individual devices and the emitted color is also quite saturated or pure. These devices also have a faster response time compared to LCDs. With this technology, the darker part of the displayed images could be truly black, as the emitting device can be turned off, leading to contrast ratios of above 100000:1, resulting in a high dynamic range (HDR). Despite these attractive features, there are certain limiting features of OLED displays. As these devices are made up of organic compounds, they are quite sensitive to moisture and oxygen [15]. Hence, even with a much simpler architecture, the manufacturers require extremely high-quality encapsulation layers, to protect these devices from degradation. These devices also degrade over-time based on their drive current. The more heavily used devices degrade faster, commonly observed as “burn-in” in these displays, which means that static images displayed at high brightness on the screen, leave their imprint even after the displayed image has changed. Manufacturers have gotten around this problem by refreshing the pixels at certain intervals of time, thereby delaying the onset of this issue. The most limiting attribute of OLEDs is their total light output, which is less than 600 nits (cd/m^2), which is not suitable for high ambient light viewing applications mainly portable displays. Considering three decades of development, further improvement in brightness of these state-of-the-art displays is highly unlikely.

Micro-LED displays combine the advantages of both the above technologies, with the trade-off of technological immaturity and high cost. Instead of utilizing a phosphor converted white light in the BLU, self-emissive red, green and blue micro-LEDs combined into the size of a single pixel can provide extremely high brightness, sharpness and contrast ratios. InGaN based blue and green mini-LEDs have achieved almost 85 % and 60 % efficiencies, respectively [18-19]. Red mini-LEDs utilizing another material system called Aluminum Indium Gallium Phosphide (AlInGaP) have also demonstrated 60-70 % efficiencies [20-23]. A simplified display panel design like OLEDs, without the extreme encapsulation limitations, can help achieve displays with efficiencies quite similar to the LEDs themselves. These displays will also exhibit longer lifetimes due to their inorganic nature and better heat dissipation due to their smaller sizes [24]. Due to the smaller sizes of these devices, the capacitances exhibited by the micro-LEDs is also quite small, bringing the response times to nano-seconds range, making it quite attractive for high-speed visible light communication (VLC) applications [25]. Owing to these advantages, micro-LED display is being considered as the next in-line display technology after OLEDs. For the consumer electronics industry, investing in micro-LEDs' R&D is quite relevant for two reasons. First, for the near-eye displays, micro-LEDs sized below 10 µm, ensure an extremely sharp image and hence an immersive user experience. Secondly, for cost effective commercialization of the micro-LED technology the device sizes need to be scaled below 5 and 10 µm, for smartphones and TVs, respectively [26]. This calculation was made assuming a 6" processed wafer with 2 µm street width between the LEDs costs $ 400. The pathway to commercialization, however, is not as trivial. The efficiencies of the red, green and blue mini-LEDs mentioned above reduce upon shrinking the device sizes. Extensive research has been performed in the past decade to lower the size dependent efficiency droop utilizing various sidewall treatments. Although nitride based micro-LEDs have shown improvement in this regard, phosphide based micro-LEDs have proved quite difficult to scale [27-28]. The reasons for this will be discussed in detail in the next section. This motivated us to pursue the unconventional path of nitride based red micro-LEDs. In the next section, the basics of nitride LEDs, the effects of dimensional scaling and differences compared to phosphide LEDs are discussed.

B. Inorganic LEDs – Basic principles and the Green Gap

A simple light emitting diode (LED) epitaxial structure requires p-type and n-type doped semiconductor, connected through a thin lower bandgap undoped semiconductor called the quantum well (QW). Typically, multiple QWs (MQWs) and carefully designed barrier layers are implemented to improve the light output from a device. The MQWs are the regions where the positively charged carriers (holes) and the negatively charged carriers (electrons) recombine to emit light. For conventional (c-plane oriented) GaN LEDs, the wavelength of the emitted light depends on multiple parameters – bandgap of the QW, thickness of the QW, thickness and composition of the barrier layers, etc. The bandgap of the QW is the dominant parameter for tuning the wavelength of light emission and is generally controlled by its alloy composition. Figure 1.2 shows the bandgap versus lattice constant plot for various material systems [29]. The (In,Ga,Al)-N material system spans a range of 0.7 – 6.1 eV going from near infra-red (IR), through the visible range, and up to the far ultra-violet (UV) emission spectrum as shown in figure 1.3. GaN is doped with magnesium to achieve p-type doping and with silicon to achieve n-type doping. These doped

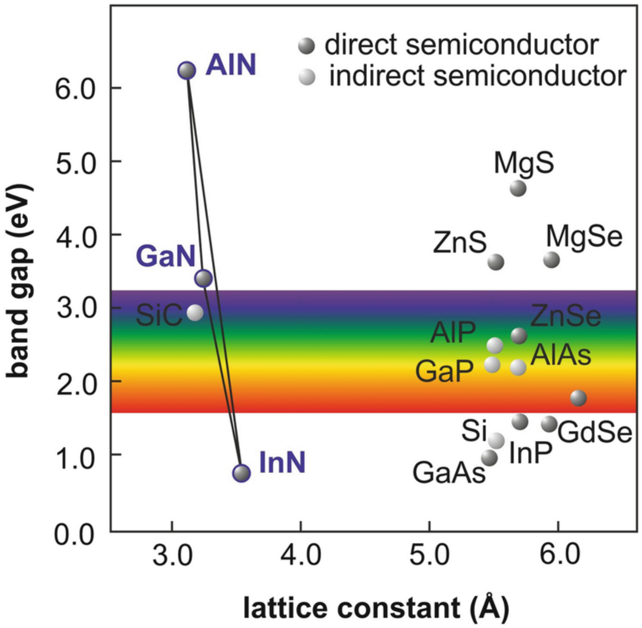

Figure 1.2 Bandgap energy versus Lattice constant for various semiconductors. Reprinted with permission from Springer [29]

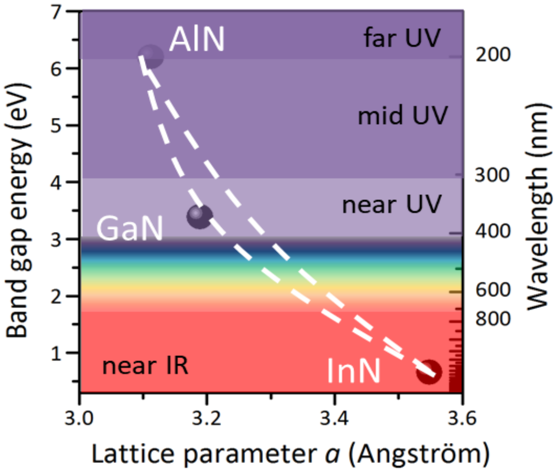

Figure 1.3 Bandgap energy and wavelength versus Lattice parameter for (In,Ga,Al)-N

layers are connected through a QW comprised of Indium Gallium Nitride or InGaN, as it offers a lower bandgap for quantum confinement of charge carriers. The higher the mole-fraction (x_{In}) of indium in the QW, the longer the wavelength of emission. For example, a higher indium content in the QW is needed for a green emission than for blue emission. Applying a suitable bias across this diode leads to light emission.

I. *Definitions of efficiency terms*

Before getting into the details of the nitride and phosphide LEDs, it is important to know the following terminologies which will be encountered throughout this text.

1. Internal quantum efficiency (IQE):

$$\eta_{\mathrm{IQE}} = \frac{\text{\#photons emitted from the active region per second}}{\text{\#electrons injected into the active region per second}} \quad 1.1$$

2. Light extraction efficiency (LEE):

$$\eta_{\mathrm{LEE}} = \frac{\text{\#photons emitted into the free space per second}}{\text{\#photons emitted from the active region per second}} \quad 1.2$$

3. Injection efficiency:

$$\eta_{\mathrm{injection}} = \frac{\text{\#electrons injected into the active region per second}}{\text{\#electrons injected into the LED per second}} \quad 1.3$$

4. External quantum efficiency (EQE):

$$\eta_{\mathrm{EQE}} = \frac{\text{\#photons emitted into the free space per second}}{\text{\#electrons injected into the LED per second}} = \eta_{\mathrm{injection}} \times \eta_{\mathrm{IQE}} \times \eta_{\mathrm{LEE}} \quad 1.4$$

EQE is typically measured for devices and IQE is determined based on an estimation of the light extraction efficiency, usually carried out using ray tracing techniques. More detailed analysis is presented in Chapter 4. In the analysis that follows either the EQE or IQE of various devices will be compared to draw conclusions.

II. *Phosphide based red emitters*

Up until late 80s, the arsenides were the primary red emitters. AlGaAs based red LEDs were utilized in automotive brake lights and traffic lights under high ambient light conditions. However, it was pointed out that these devices suffered from severe degradation due to oxidation and hydrolysis of the AlGaAs layers [30-31]. The AlInGaP material system was then developed, which is being widely used for high brightness LEDs in the red, orange, and amber emission range. For Gallium and Indium compositions of 0.5 each, InGaP can be grown lattice matched to the readily available GaAs substrates. As the atomic radii of aluminum and gallium are quite similar, $(Al_xGa_{1-x})_{0.5}In_{0.5}P$ can also be grown lattice matched to the GaAs substrate [32]. For an Aluminum composition of greater than 0.53, this semiconductor has indirect bandgap and below this composition it is a direct bandgap material. The direct-indirect bandgap crossover point lies in the emission range of 550 – 600 nm. Both the lattice mismatch and direct to indirect crossover for high aluminum content in the QWs results in a lower EQE in phosphide LEDs when moving to higher bandgap or shorter wavelength emission as can be seen in Fig. 1.4 [20].

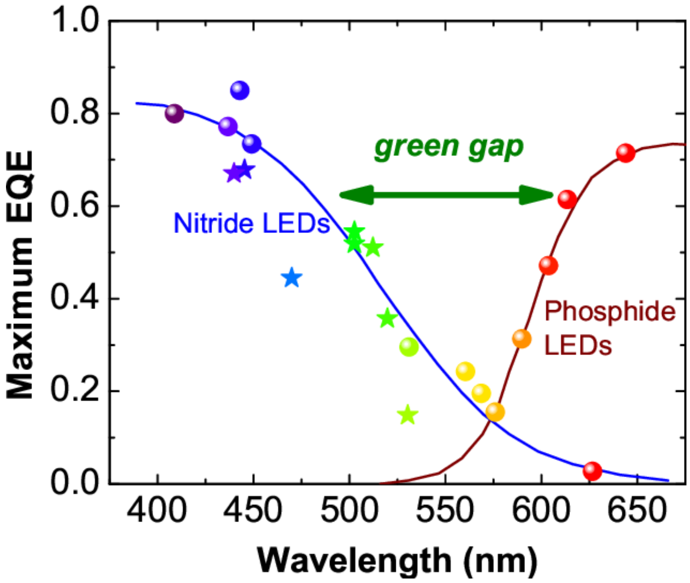

Figure 1.4 Bandgap energy and wavelength versus Lattice parameter for (In,Ga,Al)-N. Reprinted with permission from APS [20].

For red emission (~630 nm), highly efficient AlInGaP based LEDs and mini-LEDs have been demonstrated [20,23]. These devices, however, suffer from efficiency droop at high temperature of operation [33]. The low band offsets offered by the phosphide-based heterojunctions do not offer a significant barrier for charge carriers to stay confined, when high thermal energy is made available due to a raised temperature. This leads to carrier loss and hence efficiency lowering or droop. This material system also has a high surface recombination velocity of ~10^6 cm/s, which make these devices highly sensitive to plasma etch damage encountered during LED fabrication [32,34]. Additionally, as discussed before, the scaling of LEDs to micron-sized range is required for commercialization and widespread adoption [26]. When scaling down in the dimension, the surface area to volume ratio is enhanced. As the isolation of p and n-type contact layers utilizes plasma etching, an enhanced surface area to volume ratio for a material with high surface recombination velocity causes the non-radiative recombination to dominate. With a higher non-radiative recombination (surface recombination), the radiative component is reduced as the charge carriers find a shunt path to recombine. Hence, the scaling issue and temperature sensitivity of phosphide based red micro-LEDs needed an alternate material system.

In this regard, nitride-based devices were explored for red emission. The surface recombination velocity of the nitride material system is ~10^4-10^5 cm/s, which is at least an order of magnitude lower than that of the phosphides, enabling a reduced dimensional scaling related efficiency droop [34]. Additionally, the ability to form heterostructures across the (In,Ga,Al)-N system allows for higher barrier heights compared to the phosphides, resulting in a lower carrier loss at elevated temperatures of operation. Hence, temperature dependent efficiency droop is also lowered with the nitride-based devices, when the barrier heights are designed to provide a high band offset. These advantages offered by the nitride material system have motivated us to pursue InGaN micro-LEDs for red emission. However, figure 1.4 shows that the EQE of nitride-based emitters decreases with increasing wavelength of emission. In the next section, the reasons for this observation and methods to resolve these issues are discussed.

III. Nitride based long wavelength emitters

Due to the lack of cost-effective native substrates, the III-nitrides are usually grown on a foreign substrate such as sapphire, silicon carbide or silicon, leading to high defect densities in the range of 10^7 – 10^9 cm^{-2}. Surprisingly, even at such high defect densities, exceptional device level demonstrations have been obtained for blue InGaN LEDs with indium content of 0.13-0.18 in the QWs. Typically, there is a lateral fluctuation in the indium content across the wafer due the low miscibility of InN with GaN. This results in formation of localized quantum confinement states across the wafer, where radiative recombination of charge carriers takes place preferentially [35-36]. These localized radiative recombination centers shield the charge carriers from the dislocation or defect sites that cause non-radiative recombination, resulting in highly efficient devices. For green emission, the peak EQE numbers obtained so far are about 25% lower than the highest EQE numbers obtained for blue devices. The EQE for these LEDs is ~ 60% and the indium content in the QWs is typically between 0.22 – 0.26 [19]. This reduction in efficiency can be partly attributed to the ~10% lattice mismatch between InN and GaN, evident from figure 1.3. The misfit strain induced by the lattice mismatch is relaxed partly through the formation of defects for higher indium content, also reducing the radiative recombination in the QWs [37-39]. A higher strain in the structure also mitigates the indium incorporation in the films, a phenomenon called composition pulling effect [40-42]. Another issue with the growth of InGaN films is its thermal instability, wherein InN sublimes at 550°C and metal organic chemical vapor deposition (MOCVD) growth of GaN usually takes place at above 1000 °C [43]. Hence, InGaN is usually grown at a temperature of 800-900 °C, with higher indium content needing a lower growth temperature, negatively impacting the crystal quality. To resolve this issue a biaxially relaxed InGaN pseudo-substrate (PS) is extremely desired which will be discussed in the next section.

C. Relaxed InGaN Pseudo-substrates

Suppose low indium content films ($x_{In} < 0.05$) are grown strained to GaN buffer layers at a relatively high growth temperature of 900 °C, as shown in fig. 1.5 (left).

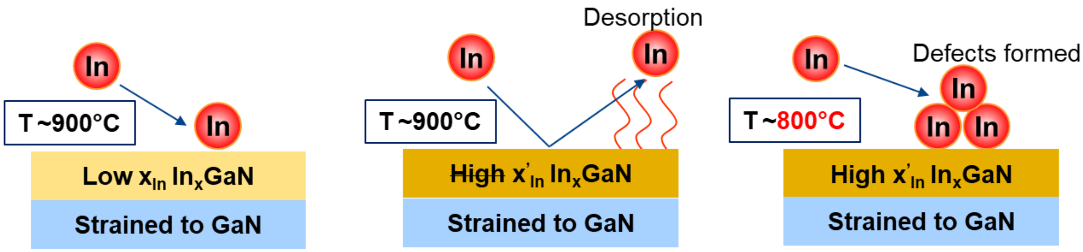

Figure 1.5 InGaN grown strained on GaN

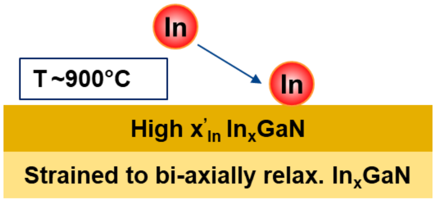

Figure 1.6 InGaN grown on a relaxed InGaN PS

As the x_{In} is low, the lattice mismatch between the $In_xGa_{1-x}N$ and GaN film is low, so the indium incorporation will be as expected. If at the same growth temperature, a higher indium content is desired and a higher indium precursor flow is supplied during the growth, the indium incorporation will not be enhanced as shown in fig 1.5 (center). The first reason for that is the lower thermal stability of higher indium content films causing desorption of indium at high growth temperatures. Secondly, if the desorption is somehow suppressed by tuning the growth rate, a higher indium content in the initial stages of the growth will mitigate any further enhancement in the indium incorporation in the subsequent layers to maintain the overall structure at a lower strain state. This phenomenon is called composition pulling effect and has been reported by several research groups at high growth temperatures, leading to a lower indium content but a higher quality film [39-42,44-46]. An enhanced indium content can be achieved by lowering the growth temperature substantially, say by 100 °C as shown in fig 1.5 (right). However, this high indium content in the films gives rise to very high misfit strain in the epitaxial structure as the lattice mismatch in comparison to GaN buffer layer increases. The misfit strain relaxes partly via defect formation, resulting in a lower film quality, which is undesirable.

Ideally a high indium content at a high growth temperature is desired. This can be achieved by growing InGaN on a bi-axially relaxed InGaN PS as shown in fig. 1.6. Due to a lower lattice mismatch between the relaxed InGaN base layer and the growing InGaN film, a high indium content can be achieved as the overall strain state of the epitaxial structure remains low.

I. Prior efforts to fabricate relaxed InGaN pseudo-substrates

The availability of strain relaxed InGaN buffer layers, with an in-plane lattice constant closer to that of the QWs is highly desirable to obtain high efficiency long wavelength (>500 nm) III-nitride optoelectronic devices. A reduced lattice mismatch between the buffer layer and the QWs not only results in a better material quality, but also in a higher Indium incorporation efficiency as discussed in the previous section. Attempts to grow relaxed InGaN buffer layers lattice matched to substrates such as ZnO and $ScAlMgO_4$ using MOCVD, have been challenging due to the very low growth temperatures required for deposition on ZnO and the high n-type conductivity of InGaN grown on $ScAlMgO_4$ substrates, respectively [47-51] Using molecular beam epitaxy (MBE) growth technique, compositionally graded relaxed InGaN layers have been demonstrated. These layers exhibited superior surface morphology, with RMS surface roughness as low as 0.75 nm for ~500 nm thick $In_{0.1}Ga_{0.9}N$ layer [52]. However, these films relax plastically thereby relieving the misfit strain in the epitaxial layers through the formation of threading dislocations, which is not ideal for device level demonstrations.

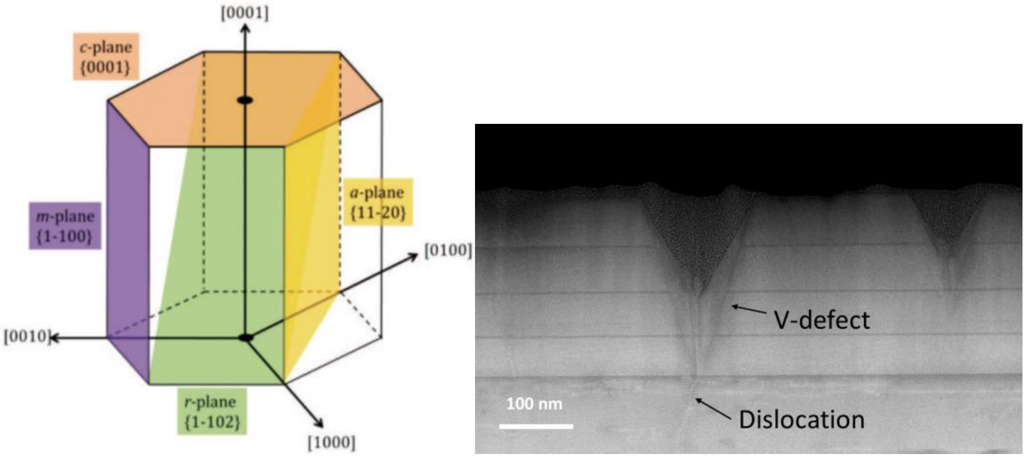

Fig. 1.7 (left) Schematic representation of various GaN planes, reprinted with permission from IOP (right) High angle annular dark field Transmission Electron Microscopy (HAADF TEM) image of a v-defect in InGaN films originating from a threading dislocation in the GaN buffer (Images acquired by Dr. Feng Wu).

Elastically relaxed InGaN films are desired to ensure strain relaxation via defect formation is eliminated. Prior efforts targeting elastic strain relaxation utilized nano-patterning of MOCVD grown strained InGaN films on GaN buffer layers. Owing to the enhanced aspect ratio of the patterns (ratio of feature height to feature dimension), elastic strain relaxation can be achieved [53]. However, during the growth of strained InGaN films using MOCVD, an inverted hexagonal shaped defect called v-defect initiates at the site of threading dislocations. These v-defects have semipolar r-plane sidewalls (Fig 1.7-left) with low growth rates; hence they are difficult to fill once formed and grow larger in size with increasing layer thickness (Fig 1.7-right). Careful placement of these defects has shown enhancement in radiative efficiency by dislocation screening and improved carrier injection in the QWs of LEDs [54]. However, their premature inception during the growth of the PS is not desirable. An improved approach of utilizing nanopatterned mask to induce selective area growth of nano-rod LEDs using MBE resulted in superior film quality and as-grown strain relaxed InGaN films [55]. Even though nano-patterning yields elastically relaxed InGaN layers the cost, reliability and complexity involved in the fabrication steps has impeded the widespread adoption of this method for the fabrication of relaxed InGaN PS.

Soitec is a renowned industry leader in substrate technology development. Their commercially available relaxed InGaN PS (InGaNOS) utilizes patterning and multiple substrate transfer of MOCVD grown strained InGaN films. The patterns in these substrates are in the range of few 100 µm allowing for reliable fabrication of mini and micro-LEDs, which is quite attractive. However, the growth of the strained InGaN films introduce v-defects, the density and size of which is directly proportional to the indium mole-fraction of the base layer. This restricts the pathway for this substrate technology towards larger indium content base layer and hence a larger in-plane lattice constant of the relaxed InGaN PSs [39,45].

Despite being noteworthy, none of the above relaxed InGaN PSs are ideal. To achieve scaled red InGaN micro-LEDs, an ideal substrate technology must exhibit elastic strain relaxation while employing a simpler fabrication process compatible with the micro-LEDs. In this regard, a novel technique to achieve micro-meter scale elastic strain relaxation was employed, which will be discussed in detail in the next section.

II. Our approach - Flexible underlayer

The elastic strain relaxation demonstrated earlier took advantage of aspect ratio by reducing the feature size to nano-meter scale. To fabricate micro-LEDs, it was important to achieve elastic strain relaxation in the micro-meter scale regime. A flexible underlayer was utilized to accommodate the misfit strain in the epitaxial structure. Although, GaN is known to be a hard material, it tends to be mechanically less stiff upon an increase in porosity, as has also been observed in silicon [56-57]. Using porous GaN underlayers with a certain porosity, elastically relaxed InGaN films could be achieved. An electrochemical etch with silicon doped GaN (GaN:Si) films connected to the metal contact acting as the anode and a platinum wire acting as cathode, when dipped in a 0.3 M oxalic acid solution at a certain bias voltage yield porous GaN films [58]. The doping of the GaN film and the applied bias play an important role in the pore size and density, respectively. To achieve porous underlayers, GaN:Si underlayers were exposed to the electrolyte by defining features using optical lithography followed by dry etch chemistry. The feature shape and size determined the symmetry and degree of relaxation of InGaN films placed above the porous layers [59]. Initial experiments involved growth of InGaN films strained to GaN, followed by porosification of the underlayers to achieve strain relaxation. These experiments will be discussed in detail in Chapter 2. The compliant property of this PS was also verified, and further optimizations were made to reduce the defect density in these InGaN PSs [60]. This approach was also not ideal as the growth of strained InGaN layer with MOCVD introduced a high density of defects in these layers during the growth. The InGaN layer was then replaced by a thin GaN layer. Upon patterning and porosification, a universal compliant GaN based substrate was achieved [61]. This substrate was utilized to demonstrate as-grown micro-meter scaled elastically strain relaxed InGaN and AlGaN films, which will be discussed in detail in Chapter 3 [61-63]. Due to the as-grown elastic relaxation, as observed in selectively grown nano-rods, superior material quality was observed. Using this substrate, an InGaN based red micro-LED sized 6 µm × 6 µm was demonstrated with measurable on-wafer EQE and an area normalized light output power nominally similar to the state-of-the-art smallest demonstrated AlInGaP based red micro-LED sized 20 µm × 20 µm [64]. These experiments and device results will be discussed in detail in Chapter 4 and 5. With continuous R&D, highly efficient porous GaN based optoelectronic devices emitting in the longer wavelength regime can be developed for the applications which cannot be served by the phosphide based long wavelength emitters.

II. InGaN relaxation using porous GaN

In chapter 1, the background of relaxed InGaN pseudo-substrates (PSs) and their need was discussed. Our approach to achieve relaxed InGaN PSs involved the use of porous GaN underlayers. In this chapter, the various experiments that were performed to study the behavior of micro-meter scale relaxed InGaN on porous GaN PSs will be discussed in detail. The epitaxial structures in this study were grown by MOCVD. The following precursors were used: triethylgallium or TEG (for the InGaN growths at lower temperature 750 – 950 °C), trimethylgallium or TMGa (for thicker GaN buffer layers grown at a higher temperature > 1150 °C), trimethylindium (TMI), ammonia, and disilane on c-plane sapphire substrates. These samples consisted of a 2 μm thick unintentionally doped (UID) GaN layer followed by 400–800 nm thick silicon doped GaN with a doping of (4–5) × 10^{18} cm^{-3}, and an 80-200 nm thick compressively strained $In_xGa_{1-x}N$ top layer. To obtain porous underlayers, a doping selective electrochemical etch step was necessary. Using patterning and dry etch steps, the electrolyte during this etch gets access to the silicon doped n+ GaN layer [59]. In the next section, the mechanism of the electrochemical etching process is briefly discussed.

A. The electrochemical etch

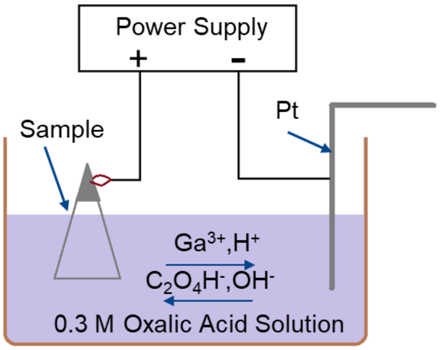

Figure 2.1 Electrochemical etch set-up

The electrochemical etch proceeds only when a conductive GaN layer is made available. The conductive layer must be n-type doped and connected to the positive source of the power supply, effectively reverse biasing the semiconductor [58]. Depending upon the applied bias, a doped GaN layer either remains unaffected, forms porous layer, or etches off completely [68]. The higher the doping the lower the voltage of porosification. Upon patterning the sample was cleaved into the size of one-eighth of a 2-inch sapphire wafer. A part of the sample was used for metal contact to connect it to the power supply through a clamp and the rest of the sample was dipped into the 0.3 M oxalic acid solution. A 10 cm long and 1 mm diameter Platinum wire was also dipped into the electrolyte serving as the cathode as shown in figure 2.1. Upon the application of bias, the etch progresses in multiple stages – inception of random etch sites on the n+ GaN layer sidewalls with hole generation, progression of the etch, removal of etch products and movement of reactants towards the etch site.

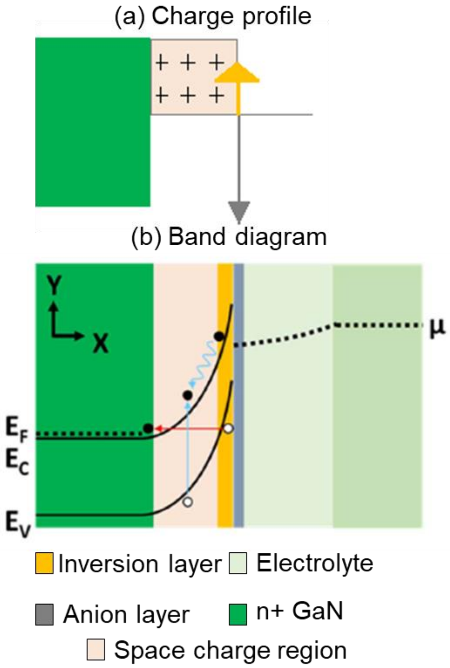

Figure 2.2 (a) Charge profile and (b) Band diagram of the n+ GaN/oxalic acid interface, reprinted with permission from ACS.

Reverse biasing the n-doped GaN layer leads to the generation of holes in the inversion layer, at the GaN/electrolyte interface. This interface behaves like a Schottky diode, the charge profile and band diagram of which are shown in figure 2.2 [65]. Under the electric field the holes end up at the surface of GaN and cause its etching due to oxidation:

$$2GaN + 6h^{+} \rightarrow 2Ga^{3+} + N_2\ (g) \qquad 2.1$$

At the site of inception of each pore, especially at the tip of the pore, the electric field reaches a local maximum leading to a larger density of holes resulting in a faster etch rate of GaN locally. This preferential etching leads to deepening of the formed pores and hence the lateral progression of the etch takes place. The gaseous byproducts escape from the pores to allow the reactants to replace them and continue the reaction, hence deeper the pores penetrate laterally through the sidewalls, the more difficult it is for the byproducts to escape. The Ga^{3+} may form insoluble or soluble products with the electrolyte, potentially altering the property of the electrolyte. The potential electrolysis of H_2O in the electrolyte, and the release of H^+ ions from oxalic acid result in the formation of H_2 gas at the cathode because of a reduction reaction. To complete the electrical circuit, the electrons released as a result of hole formation are swept from the sample towards the anode through the remaining n-doped GaN material. Typically, the samples are biased at 25-30 V for 30 minutes, followed by a solvent clean (details in the Process traveler in chapter 4). If any porous sample required a regrowth step after characterization, in addition to the above cleansing steps, the sample was dipped in concentrated HF for 4 minutes, then rinsed with de-ionized water before loading it back into the MOCVD reactor.

As the etch progresses laterally through the sidewalls, the shape of the patterns has an impact on the axial behavior of relaxation [59, 66-67]. For instance, patterning into fins yielded uniaxial relaxation while patterning into square tiles led to biaxial relaxation as discussed in detail in the next two sections.

B. Uniaxial relaxation - feature size and bias dependencies

An epitaxial structure consisting of a 2 μm thick unintentionally doped (UID) GaN layer followed by 400 nm thick Si-doped GaN with a doping of 4.5 × 10^{18} cm^{-3}, and a 200 nm thick compressively strained $In_xGa_{1-x}N$ top layer was grown using MOCVD (fig. 2.3 a).

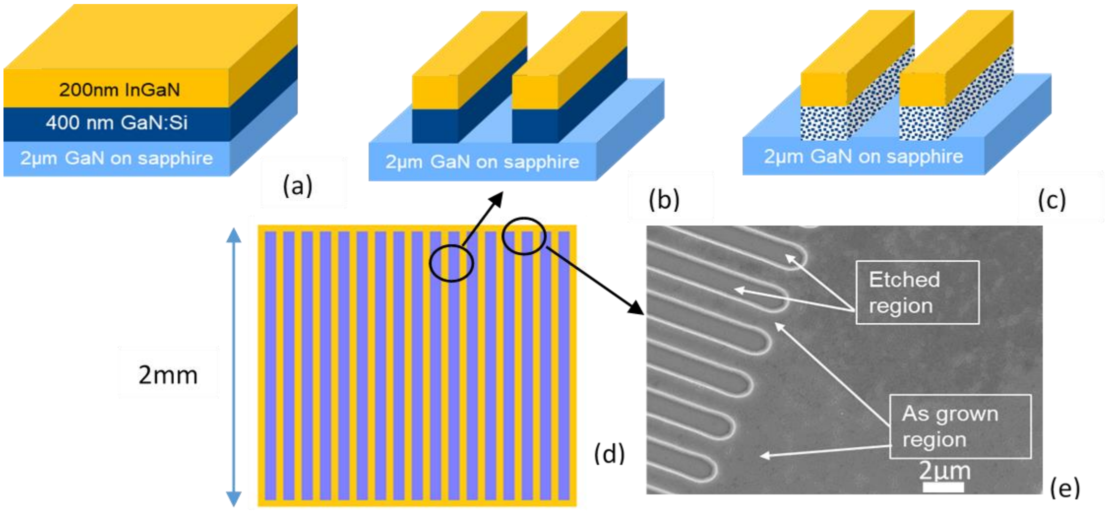

Figure 2.3 (a) Sample consisting of 200 nm $In_xGa_{1-x}N$ on top of 400 nm of GaN:Si with a doping of 4.5×10^{18} cm^{-3}, on 2 μm thick UID GaN base layers on sapphire substrate. (b) Sample structure after patterning into 2, 5, or 10 μm wide and 2 mm long fins, (c) followed by a doping selective electro-chemical etch, leading to porosification of the GaN:Si layer. (d) Top view representative schematic (not to scale) of the 2mm × 2mm die after patterning and etch, (e) SEM image of the edge of the die, reprinted with permission from IOP [59]

The 200 nm InGaN layer was composed of 37 nm of InGaN followed by 3 nm thick GaN interlayer, repeated five times. The GaN interlayers help absorb surplus indium on the surface, hence reducing the number of defects formed on the surface [69]. A nitrogen carrier gas was used during the growth of this InGaN layer. Growth conditions such as temperature and precursor flow rates were optimized to achieve thick InGaN films grown strained to GaN. The motivation behind this approach was to decouple defect assisted plastic relaxation and porous GaN assisted elastic relaxation. When the growth is not optimized, large (~ hundreds of nanometers in diameter) and dense (higher than the dislocation density of the GaN underneath) v-defects form on the surface of InGaN layers resulting in a significant amount of strain relaxation through their sidewalls. Hence, to demonstrate strain relaxation achieved entirely using porous GaN, it was important to achieve thick InGaN films grown strained to GaN.

Using optical lithography 2 μm wide and 2 mm long trenches were defined with spacings of 2, 5 and 10 μm on three different samples. Reactive ion etching (RIE) with 100 W BCl_3/Cl_2 chemistry, was used to etch these 700 nm deep trenches (fig 2.3 b,d,e). These fins were aligned to the GaN [$\mathbf{1\bar{1}}00$] plane for ease of sample alignment during lithography and during X-ray diffraction (XRD) measurements to obtain the degree of InGaN relaxation. The EC etch was performed with the sample connected to the anode for a duration of ~30 minutes (fig. 2.3 c). For each fin width, different bias voltages were applied in the range of 10 to 35 V, and the strain state of the top InGaN layer was measured using XRD, specifically (ω–2θ)–ω reciprocal space maps (RSMs) around the GaN ($\overline{11}24$) reflection to evaluate the InGaN relaxation perpendicular the fins, and around the GaN ($\bar{1}105$) reflection to evaluate the relaxation parallel to the fins. Figure 2.4 shows the degree of relaxation versus applied voltage for different fin widths in these orthogonal directions. For a certain fin width, as the bias voltage increases, the porosity (volume ratio of voids in porous GaN) increases, reducing the stiffness of the porous underlayer, thereby yielding higher degree of relaxation. At a particular bias voltage say 25 V, a narrower fin width led to a higher degree of relaxation in the direction perpendicular to the fin, because of reduced spatial restraints. As per expectation, the relaxation across the longer dimension of the fin or parallel to the fin, was lower than its orthogonal counterpart as these fins were hinged at their ends restricting the relaxation (fig 2.3 d,e). The RSM measurements in different orientation and corresponding results for a 2 μm wide fin etched at 30 V are shown in figure 2.5 (a) to (c), almost 100% relaxation across the fin was observed. The cross-sectional images were taken using FEI Helios Dualbeam Nanolab 600 Focussed Ion Beam (FIB) tool operated at 5 kV, shown in figure 2.5 (d). The porosity observed in this sample was ~ 50-60 %. These results suggest that the relaxation can be controlled by the feature size for the same applied bias and the level of porosity. Additionally, the porosity and hence the relaxation, can also be tuned with the applied bias, for the same feature size. The most unique aspect of this strain relaxation approach was that the strain was relaxed in a micro-meter scale regime. Previous efforts of strain relaxation via patterning have been typically in the nanometer scale [53,55,66]. The nature of relaxation, whether elastic or plastic, was yet to be verified.

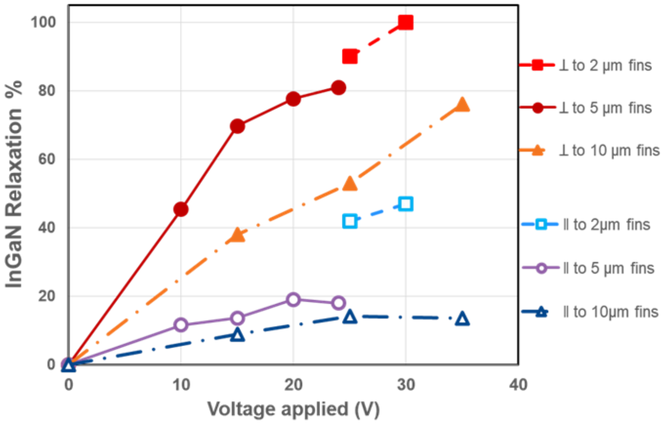

Figure 2.4 Degree of relaxation perpendicular and parallel to the fins versus applied voltage for samples with varying fin widths. Reprinted with permission from IOP [59].

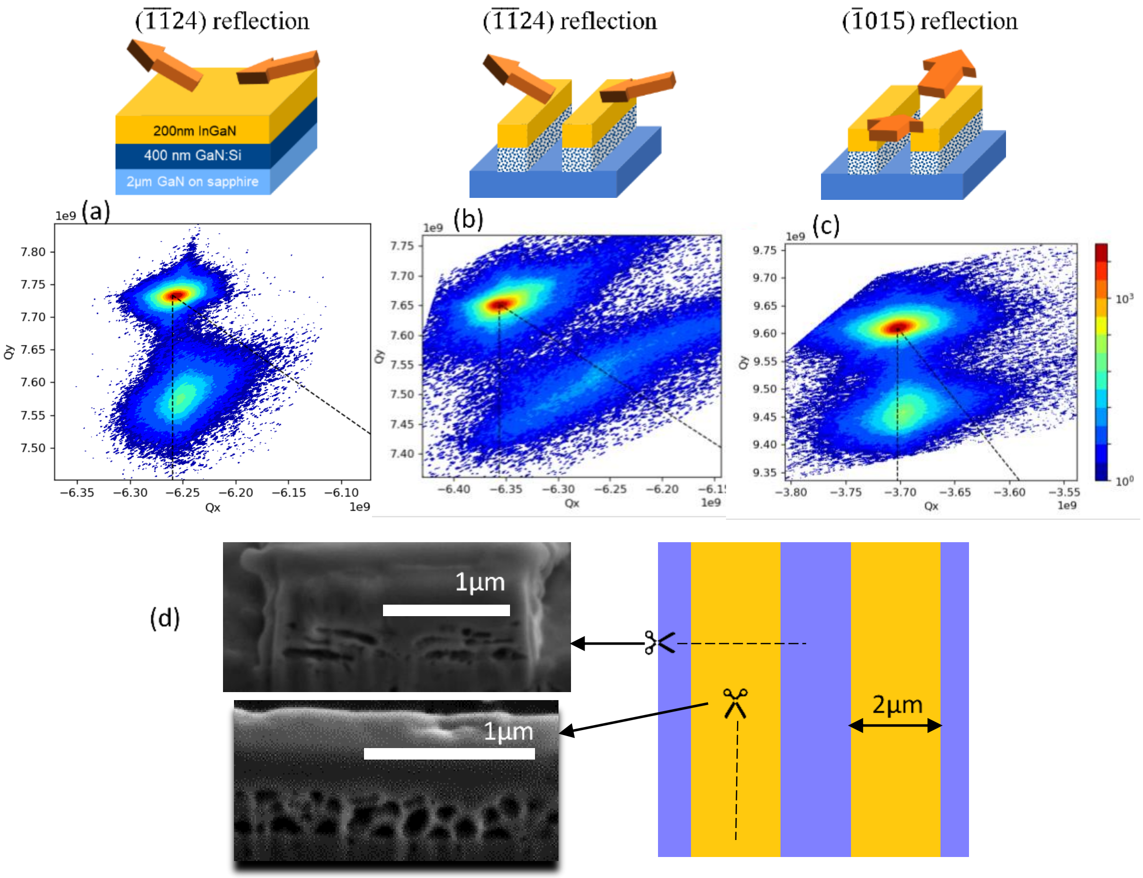

Figure 2.5 (a) RSM of as-grown sample along the GaN $(\bar{1}\bar{1}24)$ reflection. (b) RSM along the GaN $(\bar{1}\bar{1}24)$ reflection (along the arrows) after patterning 2µm wide fins and EC etch at 30V bias. (c) RSM along the GaN $(\bar{1}015)$ reflection (along the arrows) after patterning and EC etch at 30V bias. (d) Cross sectional FIB images of the fin region post porosification for the 2µm wide fins. Reprinted with permission from IOP [59].

In the next section, experiments to demonstrate bi-axial relaxation and subsequent regrowth on these InGaN PSs will be discussed.

C. Biaxial relaxation and regrowth experiments

As discussed in chapter 1, relaxed InGaN PSs are necessary to achieve efficient nitride based long wavelength emitters. One of the pre-requisites for these PSs is that the relaxation in the base layer must be bi-axial in nature, for the composition pulling effect to be in effect, resulting in higher indium incorporation in the QWs. In the previous section, it was observed that the 1D features or fins resulted in a higher degree of relaxation in the narrow dimension, compared to the wider dimension. To achieve bi-axial relaxation, square shaped features or tiles were studied. In the fin experiments, the n+ GaN:Si layer, or the current carrying layer during the EC etch, was connected in all dies along the fins and at the ends. Even though the trenches in between, were etched down to the UID GaN buffer layer, the fins being connected at the edge of the dies, ensured the current path was continuous across the wafer. For the tile geometry, a similar approach failed, as the current carrying layer was now isolated upon etching into the UID layer on the area surrounding the tiles as shown in figure 2.6 (a). As the etch depth was 700 nm, the region in between the tiles offered a higher resistance to the path of the current. The epitaxial structure was modified to have an increased n+ layer thickness of 800 nm and the etch depth during the tile fabrication process was kept at 650-700 nm. The modified epitaxial structure consisting of a 2 μm thick unintentionally doped (UID) GaN layer followed by 800 nm thick Si-doped GaN with a doping of 5×10^{18} cm^{-3}, and a 200 nm thick compressively strained $In_xGa_{1-x}N$ top layer was grown using MOCVD (fig. 2.7 a). Hence, a total etch depth of ~700 nm i.e. 200 nm of $In_{0.08}Ga_{0.92}N$ and 500 nm of GaN: Si, with 300 nm of unetched GaN:Si surrounding the tiles, ensured a continuous current flow through the entire wafer during the EC etch (fig. 2.7 b,f). The RSM of the as-grown sample and porosified sample is shown in figures 2.7 (d) and (e), where in fully strained $In_{0.08}Ga_{0.92}N$ peak vertically aligned to the GaN peak in figure 2.7 (d) can be observed to shift halfway towards 100% relaxed InGaN slanted line in figure 2.7 (e), resulting in 45-50% relaxation. RSM measurements were also performed in the orthogonal direction to confirm bi-axial relaxation. These samples were then used for regrowth experiments, discussed next.

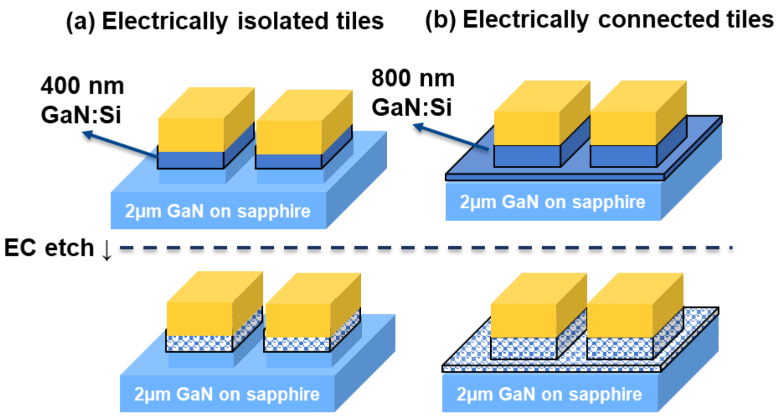

Figure 2.6 10 µm ×10 µm patterned square tiles with 200 nm $In_{0.08}Ga_{0.92}N$ top layer, and (a) 400 nm; (b) 800 nm of GaN:Si layer on 2 µm GaN buffer layers.

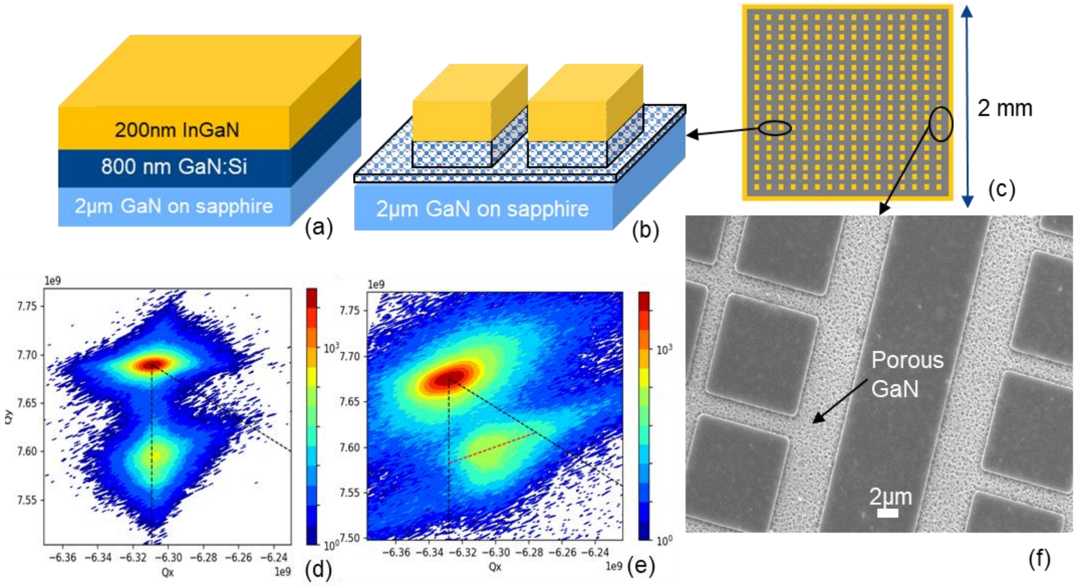

Figure 2.7 (a) Sample consisting of 200nm $In_xGa_{1-x}N$ ($x = 0.08$) on top of 800 nm of GaN:Si with a doping of 5×10^{18} cm^{-3}, on 2 µm thick UID GaN base layers on sapphire substrate. (b) Sample structure after patterning into 10 µm × 10 µm square tiles, followed by a doping selective

electrochemical etch, leading to porosification of the GaN:Si layer. (c) Top view representative schematic (not to scale) of the 2 mm × 2 mm die after patterning and dry etch, (d) RSM of the as-grown epitaxial structure shown in (a) along the GaN $(\overline{11}24)$ reflection and (e) upon patterning into 10 µm × 10 µm tiles followed by the porosification etch showing ~50% bi-axial relaxation of the InGaN top layer (f) SEM image of the edge of the die. Reprinted with permission from IOP [59].

I. MQW regrowth

The biaxially relaxed patterned InGaN PSs (sample A) discussed in the previous section, were utilized for regrowth of MQWs. For comparison, a 10 µm × 10 µm tile patterned GaN on sapphire template (sample B) and a planar GaN on sapphire template (sample C) were co-loaded with the relaxed InGaN PS sample. Four period MQWs with 2.5 nm $In_yGa_{1-y}N$/8.3 nm $In_zGa_{1-z}N$ (y >z) were grown with TMI and TEG flows of 17 and 6.5 µmol/min at 835 °C for the wells and 3.7 and 6.5 µmol/min at 869 °C for the barriers, respectively. Room-temperature photoluminescence (PL) was measured on these samples after the growth using the 325 nm line of a He–Cd laser with an excitation density of 220 W/cm^2.

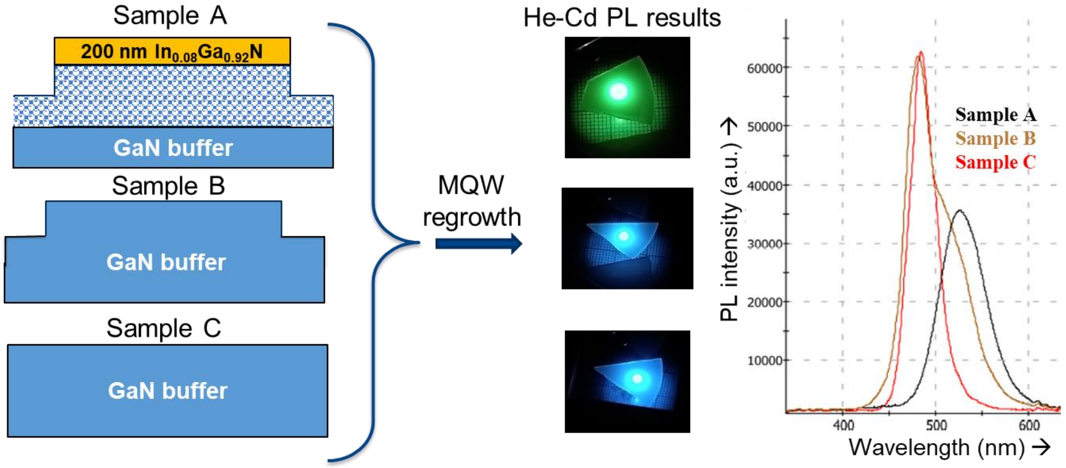

Figure 2.8 Epitaxial structures for samples A, B and C before MQW regrowth, PL snapshots and PL intensity versus wavelength plot after the MQW regrowth

Figure 2.8 shows the PL results for all the three samples. Sample B and C both demonstrated luminescence at ~480 nm, compared to sample A which luminesced at 527 nm, resulting in a redshift of ~47 nm. The red shift in the emission wavelength observed for the MQW deposited on sample A (relaxed InGaN PS sample) was caused by an enhanced indium uptake owing to the reduced lattice mismatch to the partially relaxed InGaN base layers. The PL result from sample B, suggests that the tile geometry in sample A, did not cause the precursor transport modification changing the QW thickness leading to longer wavelength of emission. The longer wavelength shoulder observed in the PL of sample B is not well understood, and maybe resulting from parasitic reflections from the sidewalls of the tiles. The lower intensity of PL from sample A can most likely be attribute to the unoptimized growth conditions at the higher indium compositions. The observation of enhanced indium uptake in QWs grown on relaxed InGaN base layers is similar to prior results obtained when growing QWs on relaxed InGaN base layers [39,45-46]. The reduced misfit strain in the epitaxial structure led to a reduction in the compositional pulling effect, resulting in an enhanced indium uptake. Beyond luminescence, XRD measurements needed to be performed to confirm the effect of composition pulling effect on these set of samples. In the next section this experiment is discussed in detail.

II. Bulk InGaN regrowth

PL results are often viewed with skepticism, as a longer emission wavelength may result from other factors such as QW thickness variation, etc. Hence, the epitaxial structure of the regrown layers was modified from MQW to bulk InGaN growth to verify the strain state of the regrown InGaN using RSM measurements. The intensity of a peak in the RSM is directly proportional to the film thickness, hence thicker films (~100 nm) were preferred over the MQW (few nms).

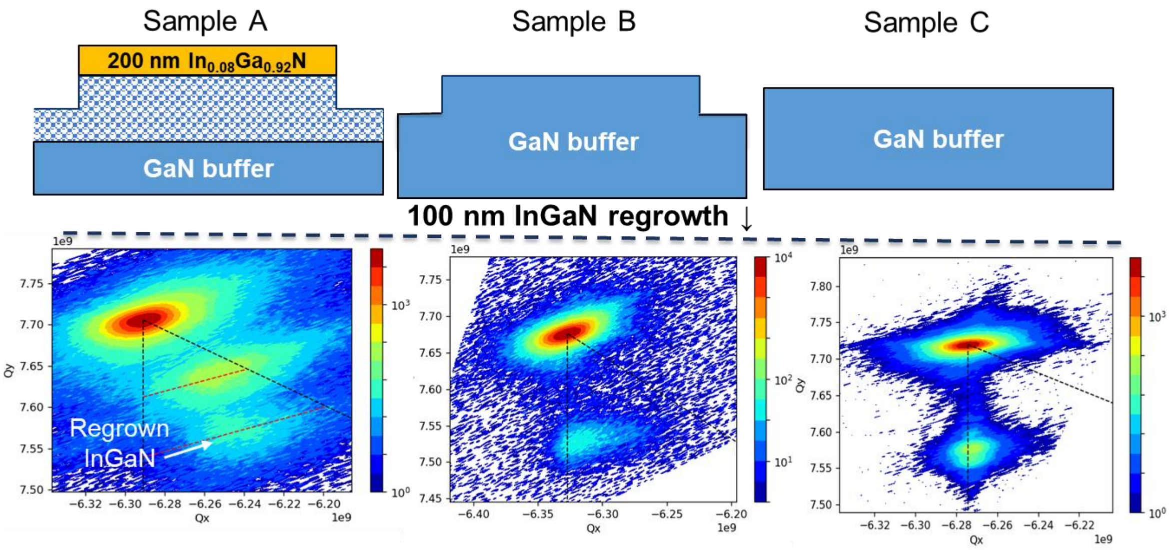

Figure 2.9 Epitaxial structures for samples A, B and C before bulk InGaN regrowth and corresponding RSMs of these samples after the 100 nm InGaN regrowth.

Figure 2.9 shows the epitaxial structure for samples A, B and C (similar to the MQW regrowth experiment) before the regrowth of the 100 nm InGaN film with the corresponding RSM measured after the regrowth. For samples B and C, the regrown InGaN layer grew almost completely strained to the GaN peak and was estimated to have an indium content of 0.12. In sample A, the regrown InGaN was as-grown 50% relaxed with an indium content of 0.145. This enhancement in indium content from 0.12 to 0.145 could be attributed to reduced composition pulling effect due to reduced lattice mismatch in the tiled porous sample. Due to the presence of bi-axially relaxed $In_{0.08}Ga_{0.92}N$ base layers in sample A, to be referred to as Layer 1 (figure 2.10), an enhanced indium incorporation was observed in the regrown InGaN layer, to be referred to as Layer 2.

Beyond the experimental verification of composition pulling effect lowering induced enhanced indium content using XRD measurements, evidence of elastic strain relaxation was also obtained. The lattice constants of the InGaN layers, were determined using the X-pert Epitaxy software using ‘a’ lattice constant of 3.1893 Å and 3.538 Å for GaN and InN, respectively. The lattice constant ‘a_{new}’ of an $In_yGa_{1-y}N$ layer, which was relaxed, R%, can be calculated following Vegard’s law:

$$a_{new} = 3.1893 \times \{1 - (y \times R/100)\} + 3.538 \times y \times R/100 \qquad 2.2$$

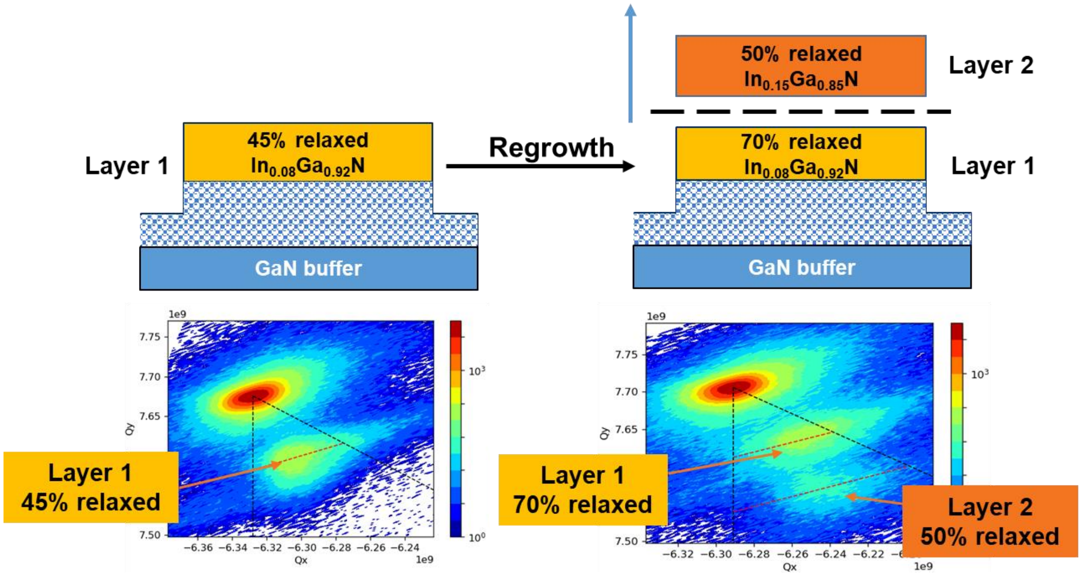

Figure 2.10 Epitaxial structure and corresponding RSM of the relaxed InGaN PS before (left) and after (right) the 100 nm InGaN regrowth.

With regrowth of Layer 2, the relaxation of Layer 1 changed from 45% to 70%. For Layer 1, using equation 2.2, the ‘a’ lattice constant changed from 3.202 to 3.209 Å. This result indicates that the use of porous GaN as a mechanically flexible layer allows the Layer 1 on the top to change its lattice constant, a known property of compliant layers. Upon closer inspection of the RSM in figure 2.10 (right), the InGaN peaks corresponding to Layer 2 is offset slightly in the ‘Qx’ direction. The lattice constant of Layer 2 was 3.214 Å as opposed to 3.209 Å for Layer 1. This could be attributed to the formation of additional v-defects, as their density increased from 4.1×10^8 cm^{-2} to 4.8×10^8 cm^{-2} after the regrowth of Layer 2, resulting in a larger lattice constant compared to Layer 1. The density of these v-defects was determined by counting them over a specific area from multiple atomic force microscopy (AFM) scans and averaging over them to obtain the nominal v-defect density for the film.

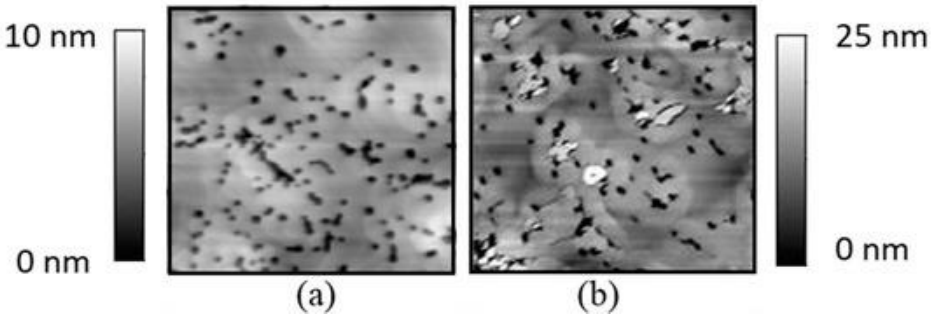

Figure 2.11 5 µm × 5 µm AFM image of sample (a) with 200 nm $In_{0.08}Ga_{0.92}N$ Layer 1 before the regrowth and (b) after the regrowth of 100 nm InGaN Layer 2. Reprinted under MDPI open access and information policy [60].

From the above result, it is evident that growing thick InGaN strained to GaN results in the formation of dense and large sized v-defects [70-71]. Even though the Layer 2 was as-grown 50 % relaxed above the base Layer 1, the poor morphology of the final epitaxial structure makes this PS unsuitable for device fabrication. Hence, an attempt was made to improve the surface morphology by growing a thinner Layer 1 and varying the indium content in this layer to study it's effect on the morphology and v-defect density, as described in detail in the next section.

D. Relaxed InGaN pseudo-substrate optimization

In the previous section, it was observed that a 200 nm thick strained $In_{0.08}Ga_{0.92}N$ as Layer 1 was not ideal in terms of the morphology and further regrowth lead to formation of 3D defects and larger v-defects on the surface as seen in figure 2.11 (b). In this section, our attempts to optimize the relaxed InGaN PS will be discussed. The first step was to reduce the thickness of Layer 1 from 200 nm to 80 nm. The reason a thinner Layer 1 was preferred, was to minimize the thickness of InGaN grown strained to GaN thereby reducing the size and density of v-defects appearing on the surface. Additionally, the mole-fraction of the thinner Layer 1 InGaN was also varied as 0.05 (sample A), 0.09 (sample B) and 0.12 (sample C), to determine the most optimal pathway to achieve a device quality relaxed InGaN PS [60].

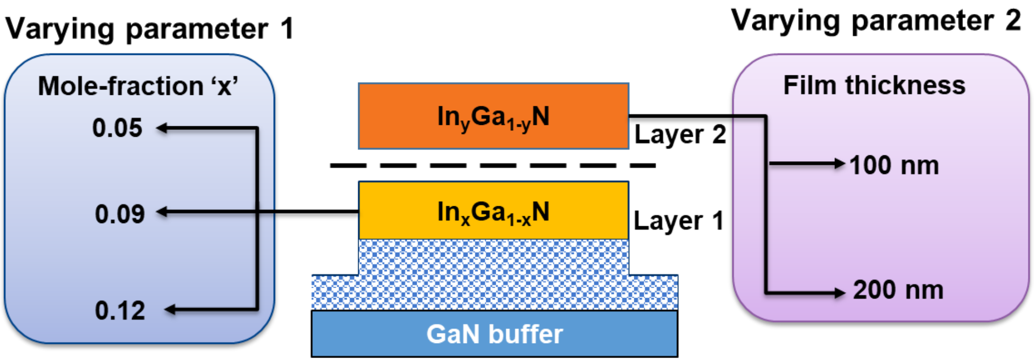

Figure 2.12 Sketch of the experiments performed to optimize the relaxed InGaN pseudo-substrate

Upon tile patterning and porosification, two sets of samples A0, B0 and C0, were used to perform regrowths of 100 and 200 nm thick Layer 2, respectively as shown in figure 2.12. All the samples with different mole-fractions (A0, B0 and C0) were co-loaded in the reactor to ensure the same growth conditions for each set during the two different regrowth experiments. The samples with 100 nm thick Layer 2 will be referred to as samples A1, B1 and C1, and those with 200 nm thick Layer 2, as samples A2, B2, and C2. The morphology, strain state and v-defects were studied for all the 6 samples before and after the regrowth. The lattice constants obtained from the XRD measurements of the two sets of samples A0, B0, and C0 are displayed in Figure 2.13. The extracted lattice constants were 3.193 Å, 3.194 Å, and 3.194 Å for the samples A0, B0 and C0, respectively. This lattice constant corresponded to a fully relaxed InGaN layer with mole-fraction 0.01–0.02. For reference the lattice constant of GaN is 3.1893 Å. The small differences between the lattice constants of the Layer 1 InGaN and GaN reflected limited relaxation of the Layer 1 for the three samples due to the low thickness of 80 nm compared to 200 nm for Layer 1 in the previous experiment, resulting in a lower driving force for the relaxation to occur.

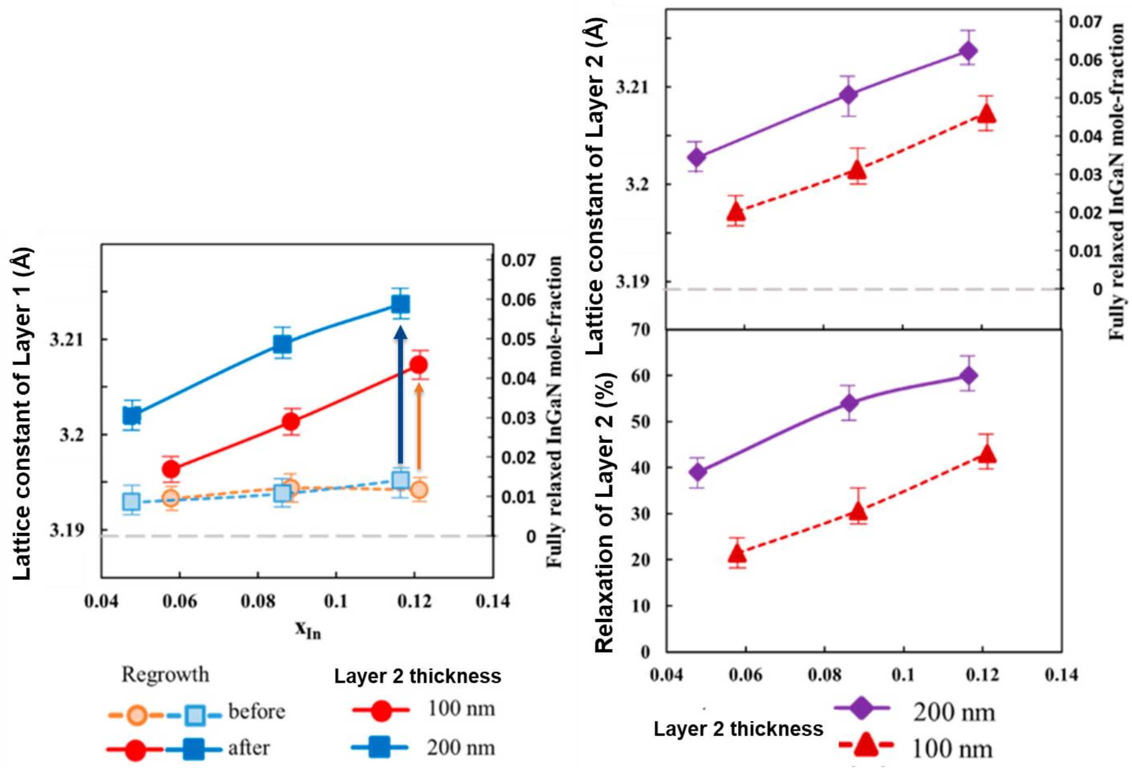

Figure 2.13 (Left) Lattice constant ‘a’ in angstrom of Layer 1 before and after regrowth of Layer 2 and respective mole fractions of a fully relaxed InGaN layer versus mole-fraction ‘x’ of Layer 1. Square markers refer to the samples with 200 nm regrowth (light blue squares depict samples before the regrowth and dark blue squares depict samples after the regrowth of 200 nm Layer 2) and the circular markers refer to the samples with 100 nm regrowth (orange circles depict samples before the regrowth and red circles depict samples after the regrowth of 100 nm Layer 2). (Right) (top plot) Lattice constant ‘a’ in angstrom of Layer 2 and corresponding mole fraction of a fully relaxed InGaN layer versus mole-fraction ‘x’ of Layer 1, after regrowth of 100 (triangles) or 200 nm Layer 2 InGaN (rhombi). (bottom plot) Degree of relaxation of Layer 2 InGaN, versus mole-fraction of Layer 1, after regrowth of 100 (triangles) or 200 nm Layer 2 (rhombi). Grey dashed line corresponds to the ‘a’ lattice constant of GaN. Reprinted under MDPI open access and information policy [60].

After regrowth of the 100-nm-thick Layer 2 InGaN, the lattice constants of the Layer 1 increased from an average of 3.193 to 3.197 Å for samples A0/A1 (x = 0.05), from 3.194 to 3.201 Å for samples B0/B1 (x = 0.09), and 3.194 to 3.207 Å for samples C0/C1 (x = 0.12), as illustrated in Figure 2.13 (left). Similarly, upon regrowth of 200 nm thick Layer 2, the lattice constants of the Layer 1 InGaN increased further from 3.193 to 3.203 Å for samples A0/A2 (x = 0.05), from 3.194 to 3.209 Å for samples B0/B2 (x = 0.09), and 3.195 to 3.214 Å for samples C0/C2 (x = 0.12) (Figure 2.13 - left). The increase in Layer 2 thickness resulted in additional stretching of Layer 1, which behaved as compliant layer due to presence of the flexible porous GaN layer underneath it. These experiments were aimed to check the effect of mole-fraction of Layer 1 and thickness of Layer 2, on the strain state of both Layers 1 and 2 and morphology of the final epitaxial structure. It was observed that the larger the indium content of Layer 1, the higher indium incorporation in Layer 2. The indium compositions measured for the 100 nm thick regrown InGaN Layer 2 were approximately 0.105, 0.11, and 0.12 for samples A1, B1, and C1, respectively, with all the samples co-loaded in the reactor to ensure the same growth conditions. For this 100 nm thick Layer 2, the extracted ‘a’ lattice constants were 3.197 Å, 3.201 Å, and 3.207 Å, respectively (Figure 2.13 - right, top), corresponding to a degree of relaxation of 21%, 31% and 43%, respectively (Figure 2.13 - right, bottom). After the regrowth of 200 nm thick Layer 2, the extracted ‘a’ lattice constants were 3.203 Å, 3.209 Å, and 3.214 Å, respectively (Figure 2.13 - right, top), and an increased degree of relaxation was observed for this layer from 21% to 39% (samples A1/A2), 31% to 54%, (samples B1/B2), and 43% to 60% (samples C1/C2) with higher thickness of the regrown Layer 2 (Figure 2.13 - right, bottom). With increasing Layer 2 thickness, there was a rise in the nominal strain in the layer resulting in a stronger driving force towards strain relaxation. In elastic continuum theory, the strain energy per unit area, E_h, for a pseudo-morphic epilayer of thickness 'h' on a (0001) substrate, with misfit strain 'ϵ', shear modulus 'G' and poisson's ratio 'υ' is given by [72]:

$$E_h = \{2G \times (1 + \upsilon)\, \epsilon^2 h\} \div (1 - \upsilon) \qquad 2.3$$

Considering Layer 2 as the epilayer and Layer 1 underneath as the substrate, the strain energy per unit area is directly proportional to the thickness of Layer 2 and square of the misfit strain between the two layers. When both layers are positioned above the porous GaN layer, the in-plane lattice constant of Layer 1 can change, resulting in a lower strain energy. For a higher indium content in Layer 2 compared to Layer 1, the in-plane lattice constant of Layer 1 increased leading to a reduced lattice mismatch between Layer 2 and Layer 1 and a decrease of the misfit strain in Equation (2). With a thicker Layer 2, this effect was more pronounced as the strain energy increased with thickness (h) of the epilayer. To compensate for this strain energy increase, the degree of relaxation of Layer 2 increased (Figure 2.13 – right, bottom). Hence, with an increase in the indium content of Layer 1, an enhanced indium content was observed in Layer 2 from 0.105 to 0.12 due to the composition pulling effect.

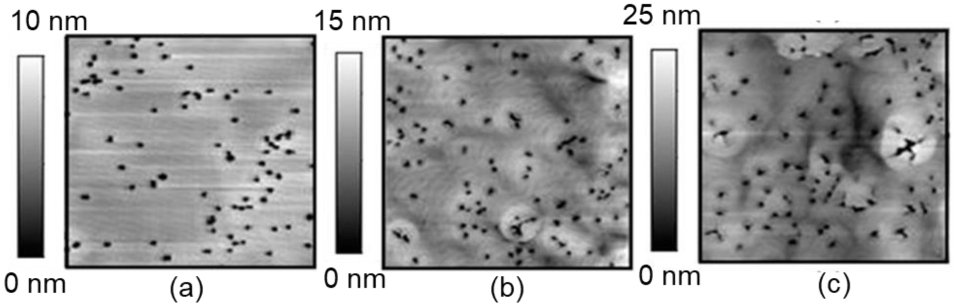

Figure 2.14 The 5 µm × 5 µm AFM image of sample (a) B0 with 80 nm thick $In_{0.09}Ga_{0.91}N$ Layer 1 before regrowth, (b) B1 upon regrowth of 100 nm Layer 2 on Layer 1, (e) B2 upon regrowth of 200 nm Layer 2 on Layer 1. Reprinted under MDPI open access and information policy [60].

The fabrication of relaxed InGaN PSs from strained InGaN films using MOCVD has long been challenging due to the formation of defects called v-defects as discussed before. Typically, these v-defects form to release strain energy, and their density and size increases as the indium composition and film thickness increases as mentioned before and observed by multiple research groups [70-71,73]. Comparing sample B1(lattice constant 3.201 Å) in figure 2.14 (b) with almost 100 nm each of Layer 1 and Layer 2, with the sample in the previous section with 200 nm thick $In_{0.08}Ga_{.92}N$ Layer 1 in figure 2.11 (a) (lattice constant 3.202 Å), with similar mole-fraction and total InGaN layer thickness, it was observed that sample B1 has nominally the same lattice constant but without the penalty of degraded morphology as can be observed from their AFM scans. For sample B1, the Layer 1 (80 nm) was grown strained to GaN while the Layer 2 (100 nm) was as-grown relaxed, while for the sample in the previous section, 200 nm thick InGaN was grown strained to GaN, resulting in 25 % higher v-defect density (4.1×10^{8} cm^{-2} compared to 3.3×10^{8} cm^{-2}) and much larger defect size. Further regrowth on this sample led to formation of 3D defects (as has also been observed by other research groups, for instance in reference [74]), which is undesirable. To avoid this morphology degradation when starting with a 200 nm thick as-grown strained InGaN, an alternate approach to achieve thicker InGaN layers was to divide the InGaN base layer growth into two components. Starting out with a thinner InGaN film (Layer 1) grown strained to GaN, with small-sized defects and low v-defect density. Then partially relaxing Layer 1 using the porosification process and following it up with the regrowth of as-grown elastically relaxed Layer 2 InGaN led to less dense and smaller v-defects. Upon increasing the thickness of Layer 2, the v-defect density and size increased but was still lower than that of the sample with 200 nm thick strained InGaN layer 1. Figure 2.15 shows the trends of v-defect density for all the samples across different Layer 1 mole-fractions and Layer 2 thicknesses, although the differences in v-defect densities may not seem drastic, it provides an overall guidance towards the trends to be observed.

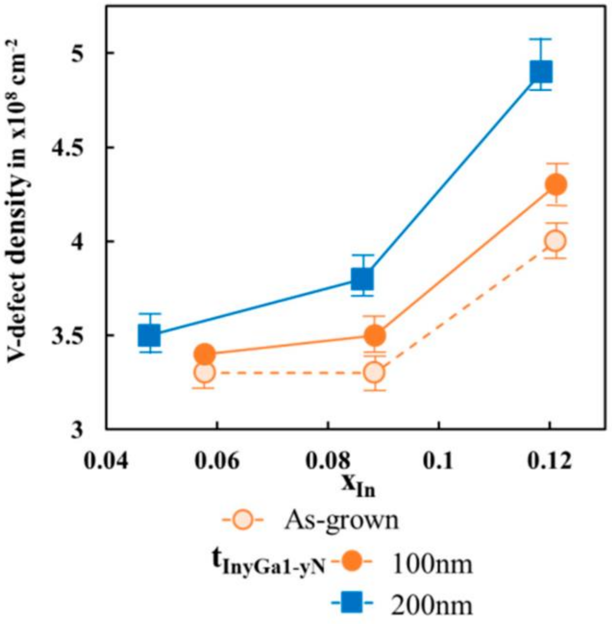

Figure 2.15 The average V-defect density on the Layer 2 surface vs. mole-fraction of Layer 1, for as-grown samples (open circles), after regrowth of 100 nm Layer 2 (filled circles) or 200 nm of Layer 2 (filled squares). Reprinted under MDPI open access and information policy [60].

Once a v-defect has formed, it typically does not coalesce or fill under the typical growth conditions required for InGaN deposition such as, low temperatures, and the use of nitrogen as carrier gas to obtain sufficient indium incorporation in the MOCVD process. From the above results, it was inferred that the presence of dense v-defects in the base layers is unavoidable if strained InGaN base layers are used. From figure 2.15, it can be observed that the density of the v-defects in Layer 2 increased with increasing indium content of Layer 1, as the average composition of the combined Layers 1 and 2 stack increased. A larger increment in v-defect density was observed for a thicker Layer 2, which can be attributed to the higher strain energy in the thicker layers. Hence, a low strain energy in the initially coherently strained Layer 1 aided in achieving compliant partially relaxed composite InGaN layer stack (combined Layer 1 and 2) with low v-defect density. Sample B1 with indium content of 0.08-0.09 was determined to be the most optimized relaxed InGaN PS in terms of the morphology (figure 2.14 (b)) including the v-defect density (figure 2.15) and in terms of lattice constant to facilitate composition pulling effect. Unlike the large v-defects formed in sample C1 and the lower lattice constant offered by sample A1, sample B1 offered a better solution for film growth with indium content of 0.1-0.12 with an optimal v-defect density appearing on its surface. Of course, these results are highly dependent on the growth conditions of Layer 2 and indium content difference between Layer 1 and Layer 2, however, these results serve as a reference and can be extrapolated to different ranges of indium content and film thicknesses. The degree of relaxation and the lattice constant of the composite InGaN layer stack obtained here can be further increased through continued growth condition and process optimizations.

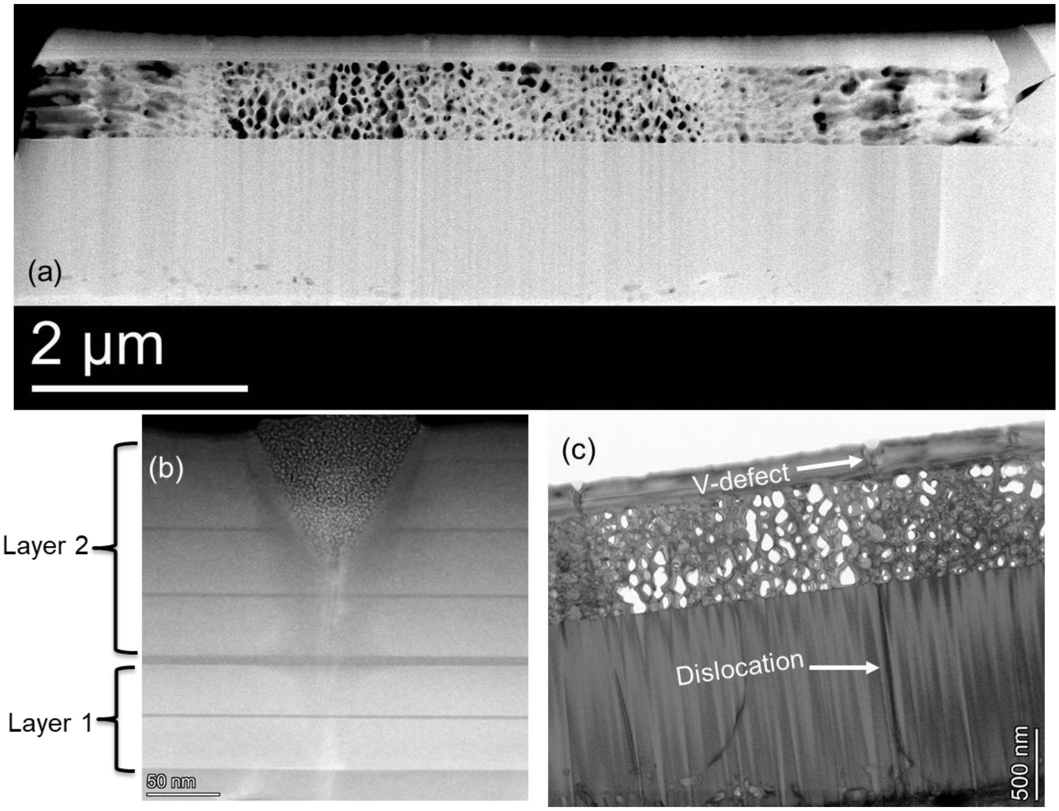

Figure 2.16 (a) HAADF TEM image of the cross-section of one of the tiles from sample B2 (Layer 1: 80 nm thick $In_{0.08}Ga_{0.92}N$ and Layer 2: 200 nm thick $In_{0.12}Ga_{0.88}N$), (b) High resolution image of a v-defect appearing on the surface originating from the Layer 1 and increasing in size with Layer 2 thickness, (c) Electron scattering contrast image of the cross-section showing the dislocation propagating through the porous layer and terminating in the v-defect at the surface. Images acquired by Dr. Feng Wu.

Figure 2.16 depicts the cross-sectional TEM images of one of the tiles from sample B1 with 80 nm thick $In_{0.08}Ga_{0.92}N$ as Layer 1 and 100 nm thick $In_{0.12}Ga_{0.88}N$ as Layer 2. The thin darker layers in figure 2.16 (b) correspond to the GaN interlayers. As observed in prior studies, the dislocations terminated on the surface as v-defects [71,73-74]. The porosification seemed to have no effect on the direction or orientation of the dislocations. The size of the v-defects grew larger in size as the layer was grown thicker, as expected and discussed before. Owing to the porosification mechanism proceeding through the sidewalls, there was a variation in the porosity of the porous layer as can be seen from Figure 2.16 (a) above. The effect of this non-uniformity on local variation of film relaxation is yet to be determined.

Additionally, the degree of relaxation of these layers was found to be highly dependent on the lateral dimension of the etched features on the sample (tiles). Our previous study on fin patterns showed that when the fin width was reduced from 10 µm to 2 µm, the relaxation perpendicular to the fins drastically increased from about 60% to almost 100%, respectively [59]. The 10 µm × 10 µm tiles in this study were chosen for their compatibility with the ultra-small micro-LED device technology. As the lateral dimension of micro-LEDs are reduced for applications in AR/VRs, smartwatches, mini-displays and in bio-photonics applications, the pattern size for the InGaN PS fabrication process may be reduced as well.

With smaller patterns, larger lattice constants can be obtained resulting in highly efficient long-wavelength micro-LEDs.

Even with thinner strained layers, the v-defects appeared on the surface, hence an alternate approach was desirable. Before depositing the epitaxial layers for device demonstration, it was important to start with a substrate with as high quality as possibly achievable. In the next chapter, a compliant universal PS will be discussed to solve this bottleneck.

III. Universal pseudo-substrate development

In the previous chapter, relaxed InGaN on porous GaN pseudo-substrates (PSs) were discussed. A part or the entire InGaN layer was grown strained to GaN initially and relaxed upon patterning and porosification of the n-type doped underlayer. This approach had the drawback that the surface of the PS would always comprise of a lot of v-defects, which were unavoidable as these defects resulted from the InGaN growth conditions and these could also relieve a part of the strain in the epitaxial structure resulting from the growth of strained InGaN layer on GaN. This strained InGaN layer was denoted as Layer 1 and upon porosification of the underlayer, this Layer 1 served as a partially relaxed InGaN base-layer and together with the porous layer underneath presented itself as a compliant PS for growth of as-grown relaxed InGaN layers (Layer 2) above them. Once the v-defects have formed in the InGaN base layers, it is difficult to planarize with subsequent growth of InGaN as the growth conditions (reduced growth temperature and N_2 carrier gas) do not aide the filling of these defects. It was also discussed in the last chapter how the size and density of these defects increases with film thickness and indium composition. Recent developments suggest that when the inception and density of v-defects is carefully engineered, it can help improve the performance of a device by enhancing the hole-injection [54,75-77]. However, these v-defects need to be nucleated in the device epitaxial structure and not at the substrate, and hence engineering the formation of these defects requires substantial research efforts. When nucleated at the substrate level, as is the case with InGaN on porous GaN PSs, subsequent growth of the LED epitaxial structure will lead to much larger v-defects and hence reducing the planar light emitting region of the LED significantly. This will also lead to an enhanced non-radiative recombination on the v-defect sidewalls, resulting in higher leakage currents [78]. Hence, the ability to grow device epitaxial structures on a smooth surface allows for a larger epitaxial structure design window. In this chapter, an improved approach towards PS fabrication will be discussed.

A. InGaN relaxation

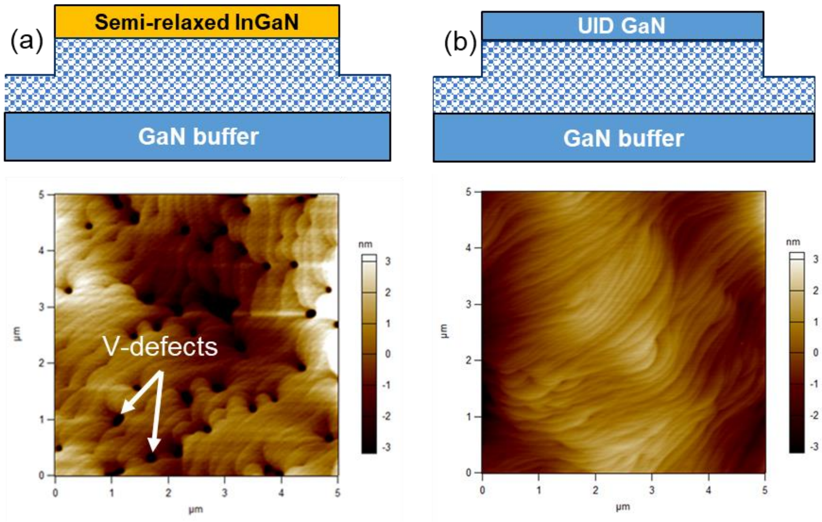

Figure 3.1 (Top) Epitaxial structure of porous GaN based PSs (bottom) with corresponding representative AFM scans to demonstrate the difference in surface morphology of (a) InGaN on porous GaN and (b) GaN on porous GaN PSs

From our initial experiments, it was learnt that the compliant property of porous GaN based PSs was provided by both the porous GaN underlayer as well as the layer positioned above it. It was also learnt that a thinner InGaN base layer (Layer 1) improved the morphology of the base layer, resulting in smaller and less dense v-defects. With this information, the InGaN base layer was replaced with a GaN layer (to be referred to as the GaN cap layer). In addition to maintaining the compliant property, the GaN capped PSs would also be nominally strain-free and could be grown at a much higher temperature without requiring N_2 ambient conditions resulting in extremely smooth surface as shown in Figure 3.1.

I. *GaN cap thickness series*

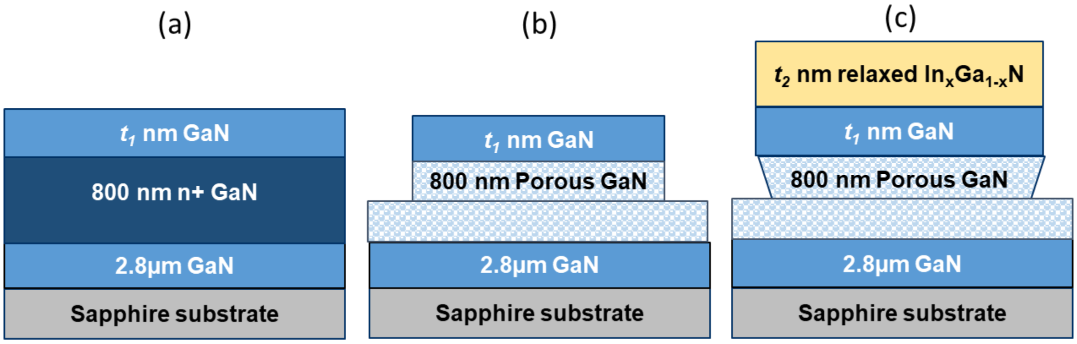

Figure 3.2 Epitaxial structure of (a) MOCVD grown sample with varying GaN cap thickness of t_1 = 30, 60, 100, and 140 nm, (b) post porosification, and (c) upon regrowth of $In_xGa_{1-x}N$ with varying thickness of t_2 = 100 and 200 nm.

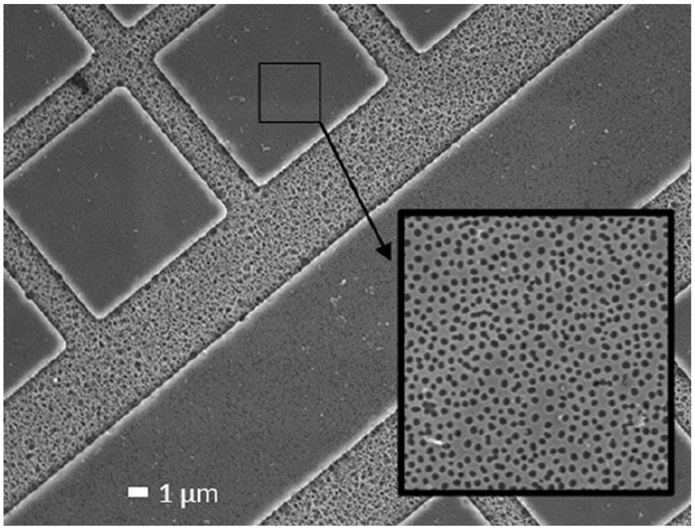

Figure 3.3 Plan view SEM image of the sample with GaN cap thickness of 30 nm, after the EC etch step. Reprinted with permission from AIP [61].

Four samples with epitaxial structures shown in Figure 3.2 (a) were grown with GaN cap thicknesses – 30, 60, 100 and 140 nm. Upon patterning into 10 µm × 10 µm sized features using optical lithography, etching half-way through the n-doped GaN layer using dry etch chemistry (figure 3.2 (b)) and subjecting the sample through the EC etch, the samples were observed with SEM. Unfortunately, for the sample with GaN cap thickness of

30 nm the pores pierced through the GaN cap layer as shown in figure 3.3, hence this sample was dropped from the study that followed, while providing us with the information about the lower limit of GaN cap thickness. The rest of the samples denoted as A0, B0 and C0 (corresponding to GaN cap thickness of 60, 100 and 140 nm, respectively) were used as PSs to grow 100 and 200 nm thick $In_xGa_{1-x}N$ layers, which were then characterized using AFM and XRD measurements to obtain information about the morphology, strain state and indium composition of the grown layers. A planar GaN on sapphire template (sample D0) was also co-loaded into the MOCVD reactor during these growths to observe the advantage offered by the presence of the porous underlayers in the GaN-on-porous GaN PSs. The nomenclature of the samples is detailed in Table 3.1 below. The GaN-on-porous GaN samples were denoted as A1, B1 and C1 after 100 nm of $In_xGa_{1-x}N$ regrowth and A2, B2 and C2 after 200 nm of $In_xGa_{1-x}N$ regrowth. Corresponding co-loaded GaN on sapphire template were denoted as D1 and D2. The InGaN regrowths were performed at 869°C with TMI and TEG flows of 11.3 and 6.5 μmol/min, with intermittent insertion of GaN interlayers as described in chapter 2. The lattice constants of the InGaN films were extracted using equation 2.2 in chapter 2, wherein the indium content and degree of relaxation were obtained from the Epitaxy software, which was used to analyze the RSM measurements performed using the XRD tool. The RSMs were performed along the GaN $(\overline{11}24)$ reflection.

Sample description	After EC etch/Before regrowth	After 100 nm $In_xGa_{1-x}N$ regrowth	After 200 nm $In_xGa_{1-x}N$ regrowth
60 nm GaN capped PS	A0	A1	A2
100 nm GaN capped PS	B0	B1	B2
140 nm GaN capped PS	C0	C1	C2
Planar GaN-on sapphire template	D0	D1	D2

Table 3.1 Nomenclature of all the samples in the GaN-on-porous GaN PS

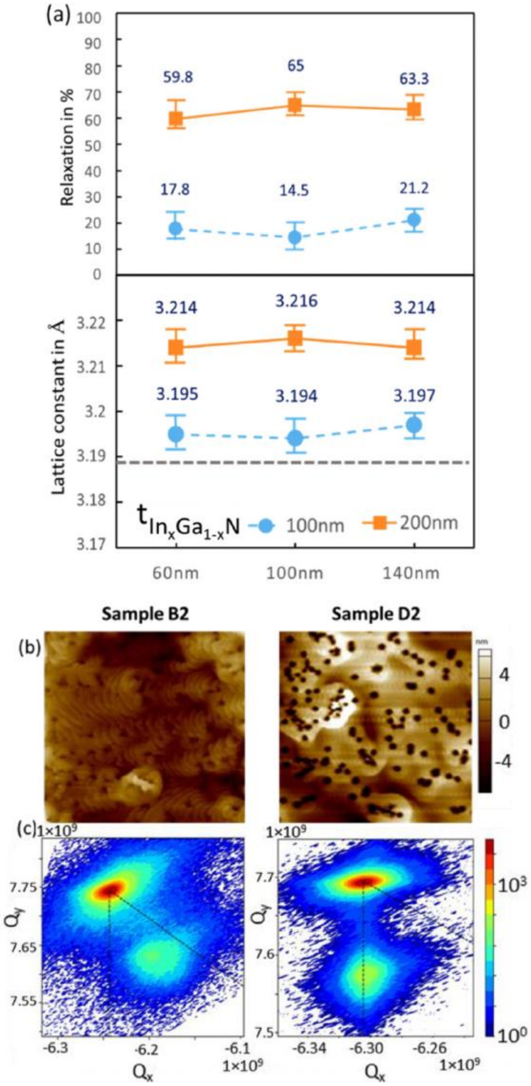

Figure 3.4 (a) The degree of relaxation and a-lattice constant of 100 nm (circle) and 200 nm (squares) thick $In_xGa_{1-x}N$ layers grown on GaN-on-porous-GaN pseudo-substrates with different thicknesses of the GaN cap layer. The dotted gray straight line in the bottom figure corresponded to the lattice constant of the coherently strained $In_xGa_{1-x}N$ layer grown on the co-loaded GaN-on sapphire reference sample. (b) AFM images across 5 μm × 5 μm scan areas of sample B2 (GaN cap thickness: 100 nm, $In_xGa_{1-x}N$ thickness: 200 nm) on the left and sample D2 ($In_xGa_{1-x}N$ thickness : 200 nm grown strained on a co-loaded GaN-on-sapphire wafer) on the right. (c) Reciprocal space maps of samples B2 (left) and D2 (right) around the GaN $(\overline{11}24)$ reflection. Reprinted with

permission from AIP [61].

Sample id	GaN cap thickness (nm)	$In_xGa_{1-x}N$ thickness (nm)	x_{In}	Relaxation of $In_xGa_{1-x}N$ (%)	‘a’ (Å)	Corresponding fully relaxed $In_yGa_{1-y}N$ y_{In}
A1	60	100	0.102	17.8	3.195	0.018
B1	100	100	0.101	14.5	3.194	0.015
C1	140	100	0.1035	21.2	3.197	0.022
D1	-	100	0.099	0	3.189	0
A2	60	200	0.1174	59.8	3.214	0.07
B2	100	200	0.1176	65	3.216	0.076
C2	140	200	0.1110	63.3	3.214	0.07
D2	-	200	0.1	0	3.189	0

Table 3.2 Summary of the GaN cap layer thickness, indium mole fraction, relaxation, and lattice constant for various samples

A summary of indium content and strain state for all the samples is detailed in Table 3.2. Upon the regrowth of 100 nm thick $In_xGa_{1-x}N$, with x within 0.1-0.12, the degree of relaxation measured was ~ 20% on average with the a-lattice constant corresponding to 3.195 Å, without any noticeable trend across the GaN cap thickness for samples A1, B1 and C1. Slightly higher indium incorporation was obtained for these samples compared to sample D1. For the samples with 200 nm thick $In_xGa_{1-x}N$ regrowth, with similar growth conditions, much higher degree of relaxation was observed ~60-65%, with the a-lattice constant corresponding to ~ 3.214 Å, as shown in figure 3.4 (a). With a thicker regrown InGaN layer, the driving force towards relaxation rises, hence the degree of relaxation and thus the a-lattice constant both increased with the thicker InGaN layer. Interestingly, there was no trend across the different GaN cap thicknesses even with a thicker InGaN regrowth, the reason for which is currently not well understood and needs further investigation. A higher indium incorporation was obtained for these samples compared to sample D2, due to a lower strain in the overall structure enhancing the indium incorporation due to a reduced composition pulling effect. For both the coloaded reference samples D1 and D2, the regrown

100 nm and 200 nm In$_x$Ga$_{1-x}$N layers were completely strained to the GaN layers underneath corresponding to a lattice constant of 3.1893 Å and degree of relaxation of 0%. Comparing samples B2 and D2, with nominally similar InGaN layer thickness, the v-defect size and density are much larger for sample D2 (figure 3.4 (b)), which can be attributed to the higher strain in the epitaxial structure. The regrown InGaN layer in this sample was completely strained to the GaN layer underneath as shown in Figure 3.4 (c). On the other hand, due to the presence of the flexible porous GaN layer and thin GaN cap layer, together forming a compliant base layer, as-grown 65% relaxed InGaN layer was achieved (sample B2), with a-lattice constant of 3.216 Å, corresponding to a fully relaxed InGaN with a mole-fraction of 0.076. Hence, compliant GaN on porous GaN PSs was demonstrated, which were attractive not only for relaxed InGaN but also to achieve relaxed AlGaN, discussed later in the chapter.

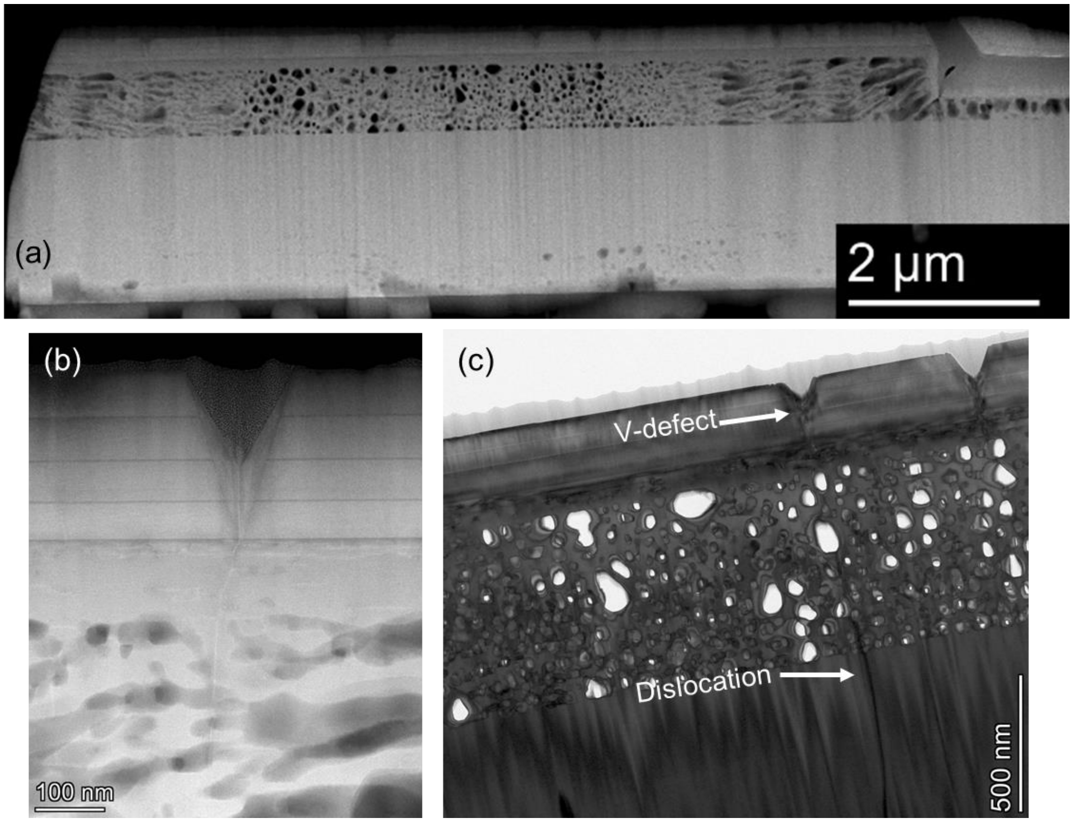

Figure 3.5 (a) HAADF TEM cross-section of one of the tiles from sample B2 (GaN cap thickness: 100 nm, regrown InGaN layer thickness: 200 nm, (b) High resolution image of a v-defect appearing on the surface originating at the InGaN regrowth interface above a threading dislocation, (c) Electron scattering contrast image of the cross-section showing the dislocation propagating through the porous layer and terminating in the v-defect at the surface. Images acquired by Dr. Feng Wu.

Figure 3.5(a) depicts the cross-sectional TEM images of one of the tiles from sample B2 with 100 nm thick GaN cap layer thickness and 200 nm thick $In_xGa_{1-x}N$ regrown above it. Like figure 2.16, the GaN interlayers could be observed distinctly as thin darker horizontal lines. From the zoomed in image of the v-defect in figure 3.5 (b), the dislocation could be observed which seemed to propagate through the porous layers as observed in the InGaN-on-porous GaN samples as well. The only difference from the prior demonstration on InGaN-on-porous GaN samples, was the position of inception of the v-defects. In the prior demonstration, the v-defect nucleated before the regrowth, from the InGaN base layer and in the current case, since the samples are GaN capped and have no strained InGaN as base layers, the v-defect nucleated at the interface of the GaN cap and the regrown InGaN layer. A similar variation in porosity of the porous GaN layer across the dimension of the tile was observed as the same lateral porosification technique was employed in these samples as well.

II. Micro-LED demonstration

To establish the potential of this substrate technology, it was important to demonstrate electroluminescence from devices fabricated above these GaN-on-porous GaN PSs. Sample B0, with 100 nm thick GaN cap layer and 10 µm × 10 µm sized tiles was chosen to deposit the LED epitaxial structure. A GaN-on-sapphire wafer was co-loaded during the growth, as a reference sample. Bottom-up the regrown LED structure consisted of 180 nm thick $In_{0.04}Ga_{0.96}N$: Si layer, 30 nm GaN:Si, 10 nm of UID GaN layer, three iterations of 3 nm / 2nm/ 10 nm $In_{0.24}Ga_{0.76}N/Al_{0.3}Ga_{0.7}N/GaN$ serving as the active region (details in ref. 79), 120 nm thick $In_{0.04}Ga_{0.96}N$:Mg as the p layer and 16 nm of $In_{0.04}Ga_{0.96}N$:Mg p+ contact layer. The compositions and thicknesses were verified using separate calibration runs. Upon thermal activation, the samples were isolated using a BCl_3/Cl_2 based low power reactive ion etch (RIE) [80] to form 5 µm × 5 µm sized devices ensuring minimal plasma etch damage. This was followed by the deposition of 200 nm thick layer of SiO_2 dielectric sidewall passivation using plasma enhanced chemical vapor deposition (PECVD) to reduce surface recombination of charge carriers. The p and n-contact regions were opened up with a wet etch utilizing buffered HF. Using electron beam deposition, p-contacts consisting of 2 nm/5 nm Ni/Au and combined n-contact/probe pad stack of 30 nm/500 nm Ti/Au was evaporated onto the sample, concluding the device fabrication flow (device cross-section in figure 3.6). This fabrication process was yet to be optimized and was used as a fast feedback technique to check whether the devices fabricated on these pseudo-substrates were capable of electroluminescence.

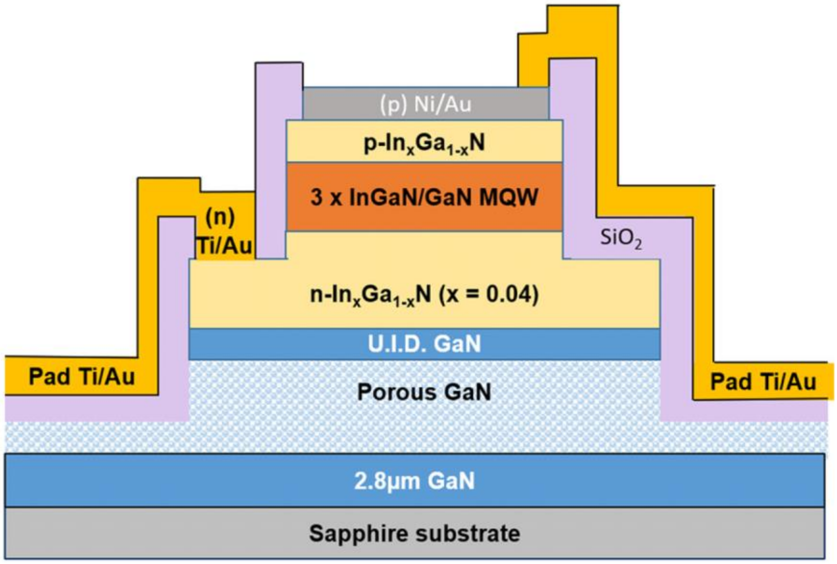

Figure 3.6 Cross-sectional schematic of the micro-LED structure. Reprinted with permission from AIP [61].

The 5 µm × 5 µm micro-LED fabricated on the 100 nm GaN capped PS, had a turn-on voltage of 3.5 V (figure 3.7 (a)) and room temperature peak wavelength of electroluminescence at 547 nm under 50 A/cm^2 direct current. A large area 300 µm × 300 µm sized LED was tested on the co-loaded reference GaN-on-sapphire wafer, and that device luminesced at 506 nm at the same current density (figure 3.7 (b)). Using the 100 nm GaN capped compliant PS, the 180 nm n-InGaN layer was ~ 60% relaxed and incorporated a higher amount of indium, leading to an enhanced indium content in the QWs, in comparison with the GaN on sapphire reference sample, resulting in the ~40 nm redshift in the electroluminescence. The n-type doped InGaN layer in the LED structure not only served as the n-layer, but also as the relaxed InGaN base layer, to help incorporate a higher indium content in the quantum wells.

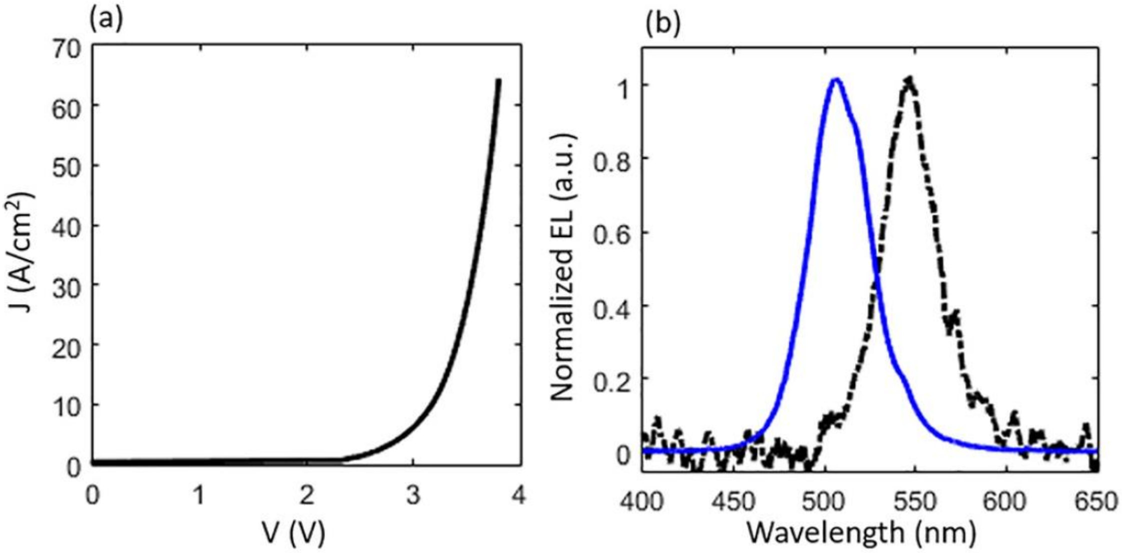

Figure 3.7 (a) I–V characteristics of the 5 µm × 5 µm micro-LED on the compliant GaN-on-porous-GaN pseudo-substrate. (b) Normalized electroluminescence of the 5 µm × 5 µm micro-LED (blue, solid) and a 300 µm × 300 µm LED (black, dashed) fabricated on the co-loaded GaN-on-

sapphire reference wafer measured at room temperature at a current density of 50 A/cm^2. Reprinted with permission from AIP [61].

These complaint GaN capped PSs, enabled the regrowth of (In,Ga)N layers with significantly improved surface morphology compared to those grown on InGaN-on-porous-GaN in the previous study, allowing the demonstration of a 5 µm × 5 µm sized green micro-LED. Like the prior observations for relaxed InGaN on porous-GaN PSs, an enhanced indium uptake and a redshift in the luminescence compared to growth on standard GaN-on-sapphire reference samples were observed. Both the results could be attributed to the relaxation of the strain in the (In,Ga)N layers, enabled by the presence of the porous GaN underlayers with reduced mechanical stiffness.

III. Color-tunable micro-LEDs

It is a well-established fact that it is difficult to achieve highly efficient micro-LEDs when the dimensions are reduced below 50 µm [27, 81, 82]. The reason behind this observation lies in the micro-LED fabrication steps and specifically the p and n contact isolation etch. The device mesas are fabricated using a plasma dry etch, which may result in the formation of various defects on the sidewalls, dangling bonds, etc. resulting in the formation of surface states within the bandgap of the material resulting eventually in non-radiative recombination [32,34]. As the size of the device shrinks, the surface area to volume ratio increases, hence the etch damage becomes a dominant reason for non-radiative recombination in these devices. At the time of pursuing this research, only one report was published on the EQE of blue and green micro-LEDs sized below 5 µm [83], and no reports existed on electroluminescence from micro-LEDs of similar dimensions emitting beyond 540 nm. Additionally, the EQE of nitride based light emitters emitting beyond 540 nm have shown a drastic reduction mainly due to the large lattice mismatch between InN and GaN

[22,84-86]. As discussed before, the misfit strain emerging from this lattice mismatch induced formation of defects in the active region, lowering the efficiency of the light emitter. Using the porous GaN underlayer based substrate technology, this lattice mismatch issue could be addressed. In the previous section, a device demonstration on the GaN on porous GaN PSs was discussed and the red-shift in the peak electroluminescence wavelength was observed in this device with reference to the LED on the co-loaded GaN on sapphire wafer. This was attributed to the compliant property of the porous GaN underlayer and the GaN cap layer positioned above it, which led to the relaxation of the n-InGaN layer deposited above it. The relaxation of this n-InGaN layer led to enhanced indium incorporation into the QWs grown subsequently. In chapter 2, the dependence of feature size on the degree of relaxation was discussed. In this section, methods to tune the peak electroluminescence on the same wafer or on a different wafer with nominally similar growth conditions are discussed. This can help display manufacturers reduce dependence on multiple material systems and rely on a single MOCVD reactor, eventually driving down the cost of this technology, which is one of the biggest roadblocks for commercialization.

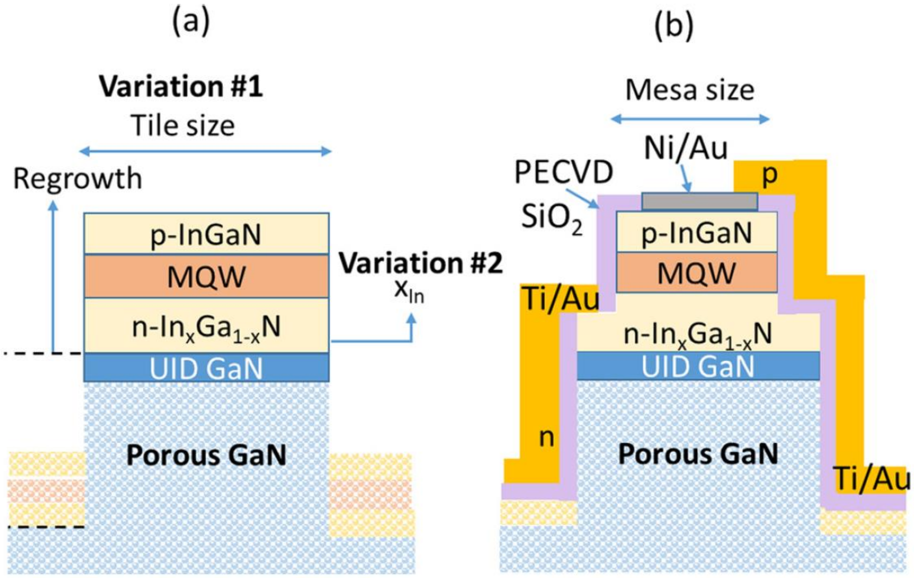

Figure 3.8 Cross sectional schematic of the LED structure (a) after regrowth with the two variations serving as tunability parameters – tile size and mole-fraction of the n-InGaN layer, (b) After fabrication of the micro-LED. Reprinted with permission from AIP [62].

GaN on porous GaN PSs were fabricated by patterning and porosification of samples, as shown in figure 3.2 (a) and (b). A portion of the wafer was left unpatterned, protecting its n type doped GaN underlayer from the EC etching step. The devices fabricated on this region of the wafer served as on-wafer non-porous reference devices for comparison with the porous devices. Figure 3.8 (a) shows the cross-section of the square tile after the regrowth of the micro-LED structure and the two variations performed on these samples. The deposited LED epitaxial structure was nominally similar to the previous experiment except for the active region compositions, with the QW composed of $In_{0.2}Ga_{0.8}N$ and the barrier composed of 2 nm $Al_{0.1}Ga_{0.9}N$ and 10 nm of UID GaN, calibrated on planar GaN on sapphire samples. The fabrication process flow was the same as in the previous experiment, and the cross-section of the fabricated device is shown in figure 3.8 (b). Upon fabrication, these devices were characterized on-wafer for a faster feedback loop and relative comparison among devices, compared to the traditionally used method of characterizing micro-LEDs in an integrating sphere. For measurement in an integrating sphere, the devices need to be diced out of the wafer and then wire bonded onto reflective headers, followed by encapsulation with a resin, before characterization. The integrating sphere also has a limit on the light sensitivity, hence the relatively low light output of these long wavelength micro-LEDs compared to blue or green micro-LEDs and small size of < 20 µm, posed difficulties for reliable measurement in the integrating sphere. An on-wafer measurement set-up was created, allowing sample observation, and probing from the top of the wafer and light extraction from the backside of the sapphire substrate within approximately a 60° half-angle cone normal to the substrate. A more detailed difference in terms of light extraction and external quantum efficiency (EQE) figures between the two measurement set-ups will be discussed in the next chapter. The wafer was placed on a stage housing an optical diffuser coupled to a fiber optic cable, whose output was collimated into a monochromator using thermoelectrically cooled Synapse CCD detector for recording the electroluminescence spectra. For each device, the spectra were measured at room temperature at various current densities and integrated over all relevant wavelengths to estimate the light output power, P_{OUT}. The EQE was then extracted as follows:

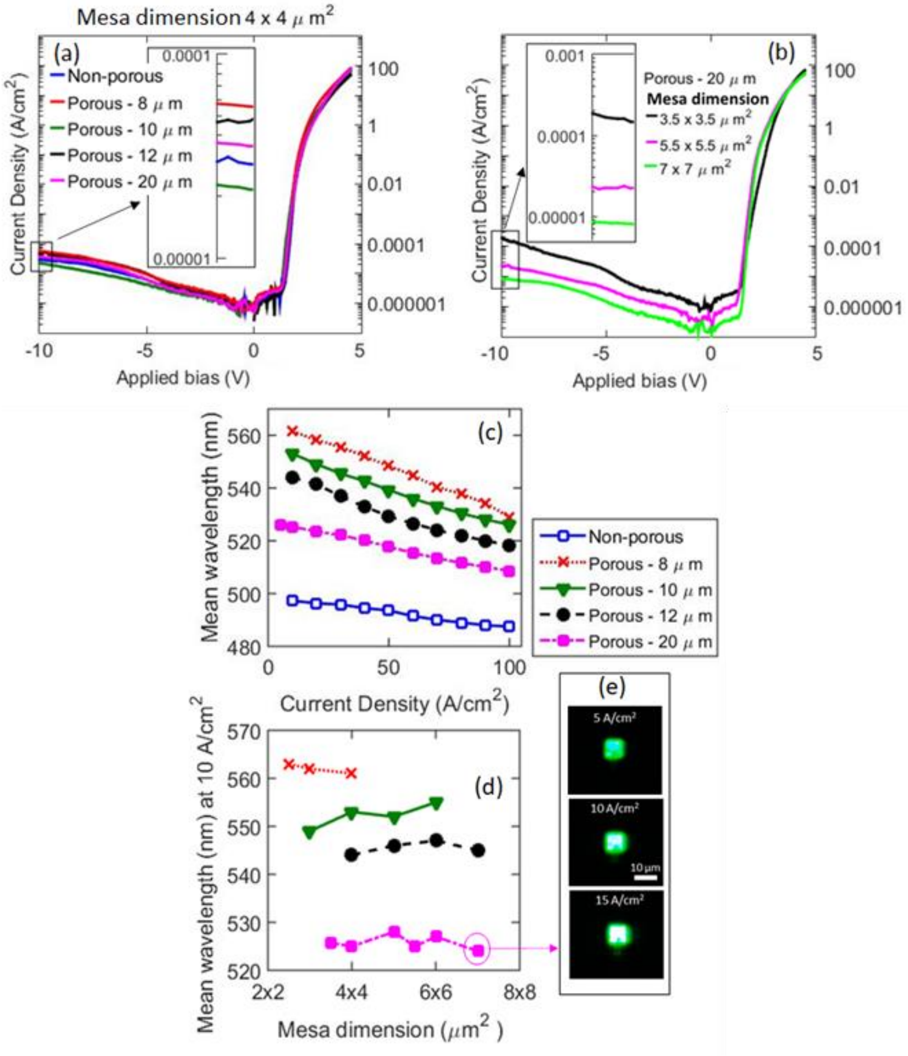

Figure 3.9 I–V characteristics of (a) 4 µm × 4 µm sized micro-LEDs fabricated on tiles with varying sizes of - 8 µm (red, cross), 10 µm (green, downturned triangle), 12 µm (black, filled circle), and 20 µm (magenta, filled square) and on the unpatterned non-porous region (blue, open square), (b) and for 3.5 µm × 3.5 µm (black), 5.5 µm × 5.5 µm (magenta), and 7 µm × 7 µm (lime green) sized micro-LEDs fabricated on 20 µm wide tiles, (c) Mean EL wavelength dependent on current density, for 4 µm × 4 µm sized micro-LEDs fabricated on tiles with varying sizes of : 8 µm (red, cross), 10 µm (green, downturned triangle), 12 µm (black, filled circle), and 20 µm (magenta, filled square) and on the unpatterned non-porous region (blue, open square). (d) Mean EL wavelength dependent on device dimensions fabricated on tiles with varying sizes of 8 µm (red, cross), 10 µm (green, downturned triangle), 12 µm (black, filled circle), and 20 µm (magenta, filled square) at 10 A/cm2. (e) EL images of a 7 µm × 7 µm sized micro-LED on a 20 µm wide tile at 5, 10, and 15 A/cm^2. Reprinted with permission from AIP [62].

$$EQE = (q \times P_{OUT} \times \lambda) \div (J \times A \times h \times c) \qquad 3.1$$

where, q is the charge of an electron, λ is the mean wavelength of the electroluminescence spectrum, J is the current density, A is the area of the light emitting region of the device, h is the Planck’s constant and c is the speed of light.

There are two dimensions that must be noted – the tile size and the mesa size. The tile size is the dimension of the pattern defined before the porosification process and the mesa size is the dimension of the light emitting region or the active region of the device (figure 3.8). For tuning the emission wavelength, the first variation was to vary the tile size, which required careful design of the mask plate used during optical lithography to define the patterns prior to porosification. In this mask plate several tile sizes were included for devices with the same mesa/device active region size. The results for devices with lateral dimension or mesa size of 4 µm, fabricated on square tiles with lateral dimension or tile size of - 8, 10, 12 and 20 µm, will be discussed. Figure 3.9 (a) shows the IV characteristics of these devices, showing similar turn-on voltage of ~3-3.5V, without any clear trend in the series resistance or the reverse leakage current. Since, these devices had a similar epitaxial structure, doping and active region dimensions, nominally the same series resistance and reverse leakage currents were anticipated, with few minor differences attributed to process variations. When comparing micro-LEDs on the same tile size of 20 µm but with different mesa sizes of: 3.5, 5.5 and 7 µm as shown in figure 3.9 (b), a clear trend of decrease in reverse leakage current with increasing device size was observed as has been observed in prior studies as well [81,87-89]. With a smaller device size, the surface area to volume ratio is enhanced, resulting in a more pronounced effect of the mesa sidewall etch damage and hence, a higher surface leakage. At high current densities in the forward bias conditions, the series resistance and high injection effects dominate leading to similar IV behavior across all these devices, indicating comparable carrier transport in them.

Figure 3.9 (c) compares the mean/peak wavelength of emission from the 4 µm × 4 µm device fabricated on different tile sizes as well as on the non-porous region of the wafer. Comparing the peak wavelength of electroluminescence at 10 A/cm^2 current density for all these devices, the micro-LEDs fabricated on 8, 10, 12, and 20 µm wide tiles emitted at 561, 553, 544, and 525 nm (with estimated indium contents of 0.245, 0.24, 0.23, and 0.22), respectively. Owing to the varying degree of strain relaxation on these differently sized square tiles, i.e., smaller features demonstrating a higher degree of relaxation, as observed for fins in ref. 59. varying extents of composition pulling effect or indium incorporation in the subsequently grown MQWs was observed evident from the redshifted peak electroluminescence wavelength from smaller features. Under the same measurement condition, the device fabricated on the non-porous region of the die emitted at 497 nm (with an estimated MQW indium content of 0.2), which was a significantly lower wavelength of emission compared to all the devices fabricated on the porous tiles. Hence, using the same growth conditions, different emission wavelengths could be obtained by varying the size of the features.

Each of these micro-LEDs also showed a blueshift in their peak electroluminescence wavelength with an increase in the current density, with a higher blueshift observed for devices fabricated on smaller tiles as shown in figure 3.9 (c). Due to the composition pulling effect, as the indium incorporation increased for smaller tiles, with the barriers being composed of AlGaN and GaN, a higher piezo-electric field existed in these devices, resulting in a higher quantum confined Stark effect (QCSE). By utilizing InGaN barrier layers, this large difference in QCSE and hence the blueshift with higher current densities, can be reduced.

For each tile dimension, the micro-LED mesa size was also varied, and the mean wavelength of emission at 10 A/cm^2 was plotted as shown in figure 3.9 (d). The peak emission wavelengths seemed independent of the mesa sizes suggesting a uniform indium incorporation across the entire tile, resulting in uniform emission across the tiles. The electroluminescence snapshots of a 7 µm × 7 µm device fabricated on 20 µm × 20 µm tile at different current densities is shown in figure 3.9 (e), wherein uniformity of emission can be observed. For the 8 µm × 8 µm wide tiles, devices with lateral dimensions 2.5, 3 and 4 µm, emitted nominally at the same wavelength of 562 nm ± 4 nm at 10 A/cm^2, with a peak on-wafer EQE in the range of 0.12 – 0.2 % at 100 A/cm^2. For the 10 µm × 10 µm wide tiles, devices with lateral dimensions 3, 4, 5 and 6 µm, emitted nominally at the same wavelength of 552 nm ± 3 nm at 10 A/cm^2, with a peak on-wafer EQE in the range of 0.2 – 0.4 % at 100

A/cm^2. For the 12 µm × 12 µm wide tiles, devices with lateral dimensions 4, 5, 6 and 7 µm, emitted nominally at the same wavelength of 545 nm ± 2 nm at 10 A/cm^2, with a peak on-wafer EQE in the range of 0.25 – 0.43 % at 100 A/cm^2. For the 20 µm × 20 µm wide tiles, devices with lateral dimensions 3.5, 4, 5, 5.5, 6 and 7 µm, emitted nominally at the same wavelength of 526 nm ± 2 nm at 10 A/cm^2, with a peak on-wafer EQE in the range of 0.25 – 0.44 % at 100 A/cm^2. These devices demonstrated an increase in the EQE with increasing current density without saturation till 100 A/cm^2. An increase in EQE for devices with a larger dimension was observed, as seen in prior studies as well [34, 81-82]. As discussed before, this trend can be attributed to the increased surface-area to volume ratio for a smaller device size, resulting in enhanced non-radiative Shockley Read Hall recombination at the edge of the device mesa. This decline in EQE of micro-LEDs with decreasing size, can be suppressed through the optimization of the fabrication process.

In the second experiment, the growth temperature of the n-InGaN was lowered, resulting in an increase in the nominal indium content of this layer from 0.04 (in the first experiment) to 0.09, keeping the growth conditions of all the other layers of the epitaxial structure the same. Two micro-LEDs sized 4 µm × 4 µm fabricated on tile 10 µm × 10 µm with x_{In} of 0.04 and 0.09 in the n-doped layer, were compared. For the device with n-$In_{0.04}Ga_{0.96}N$ (discussed in the first experiment), the turn-on voltage was ~ 3 V and the peak wavelength of emission at 10 A/cm^2 current density was 553 nm, with an on-wafer EQE of 0.4 % at 100 A/cm^2 and nominal MQW x_{In} = 0.24. On the other hand, for the device with n-$In_{0..09}Ga_{0.91}N$, the turn-on voltage was ~2 V and the peak wavelength of emission was 616 nm at 60 A/cm^2 with an on-wafer EQE of 0.001 % at 100 A/cm^2 and nominal MQW x_{In} = 0.3 as shown in figure 3.10 (a) and (b). The electroluminescence spectra for this device could not be resolved using the on-wafer EQE set-up for current densities below 60 A/cm^2, as the device

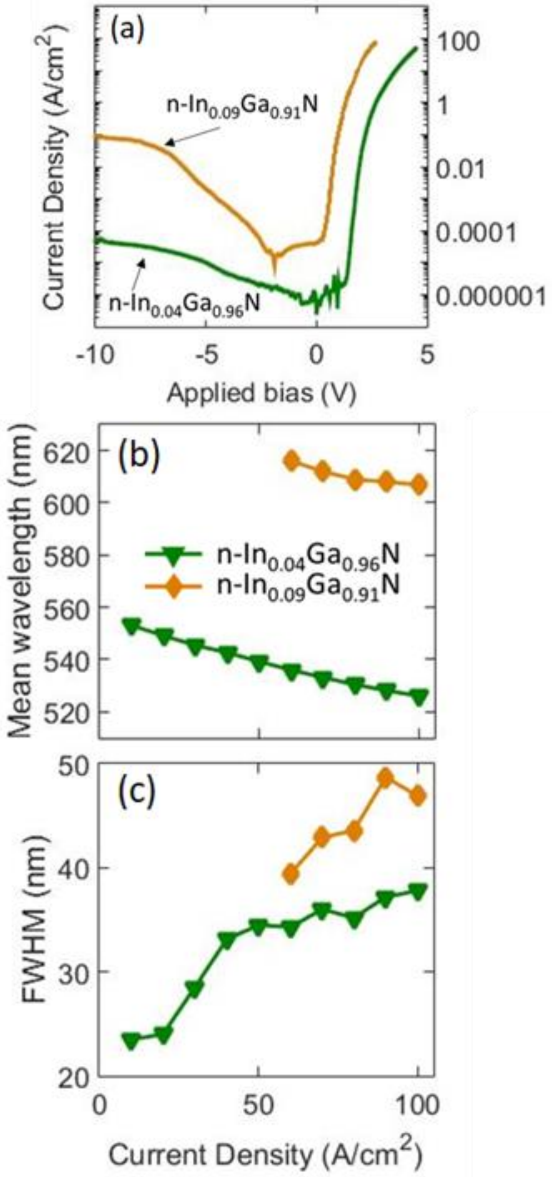

Figure 3.10 (a) I–V characteristics, (b) mean EL wavelength, and (c) FWHM of the electroluminescence peak dependent on current density for 4 µm × 4 µm sized micro-LEDs fabricated on 10 µm wide tiles with different mole fractions of the n-InGaN region of the LED structure: x_{In} = 0.04 (green, downturned triangle) and x_{In} = 0.09 (orange, diamond). Reprinted with permission from AIP [62].

was too dim. Due to the higher indium content in the n-InGaN base layer, with the same degree of relaxation of the base layers (as seen in chapter 2), the lattice constant offered by the n-$In_{0.09}Ga_{0.91}N$ was larger compared to that offered by the n-$In_{0.04}Ga_{0.96}N$ base layer to the subsequently grown MQWs. Hence a much higher indium content was achieved leading to a significant redshift in emission. At 60 A/cm^2, the corresponding wavelength of emission from the low indium content base layer device was 536 nm compared to 616 nm from high indium content base layer device, hence a remarkable 80 nm redshift was observed with a change in the base layer composition even though the growth conditions for the MQWs were the same for both the samples. The full width at half maximum of the electroluminescence spectra for both these devices increased with higher current densities as shown in figure 3.10 (c) and can be attributed to band-filling effects [85,90]. Despite the low EQE (and yield) in the high indium content base layer, this result demonstrates the potential of this technology for the fabrication of color-tunable micro-LEDs. Substantial optimization efforts in the device fabrication steps as well as the epitaxial structure design were required at this stage of development.

In conclusion, two methods to tune the emission wavelength of the InGaN based micro-LEDs from green to orange emission were discussed. Both the methods were based on the extent of composition pulling effect. While the first method required different pattern sizes on the same wafer, for the feature sizes explored it led to emission wavelength tuning from 497 nm for a non-porous device to 561 nm for a porous device on an 8 µm × 8 µm sized tile at 10 A/cm^2. The second method required different growth condition of the base n-InGaN layer and led to wavelength tuning from 536 nm to 616 nm at 60 A/cm^2 on a 10 µm × 10 µm sized tile. Using either or combination of both these techniques, completely nitride-based displays can be developed in the future. In the next chapter, efforts to optimize the fabrication process and the micro-LED epitaxial structure will be discussed. The process traveler for the above micro-LEDs was as follows:

1. Solvent clean with ultrasonication of the unporosified GaN on GaN:Si template in acetone, isopropanol followed by rinse using de-ionized water for 3, 2 and 1 minute each.

2. Pattern definition on the samples using maskplate CGLED, layer MESA using GCA Autostep

3. Etch the GaN cap and halfway through the GaN:Si layer using a 100 W BCl_3/Cl_2 RIE etch chemistry

4. EC etch in 0.3 M Oxalic acid for 30 minutes using indium contact pressed onto scratched surface to make contact with the buried GaN:Si layer.

5. Solvent clean as described in step 1, but with low ultrasonication intensity, followed by 4 minutes dip in concentrated HF, and rinse in de-ionized water.

6. MOCVD regrowth of the LED epitaxial structure

7. Pattern definition on the samples using maskplate CGLED, layer ISO using GCA Autostep

8. Etch into the InGaN:Si layer using a 15 W BCl_3/Cl_2 RIE etch chemistry

9. PECVD deposition of 200 nm thick SiO_2 at 250 °C

10. Pattern definition on the samples using maskplate CGLED, layer PCONT using GCA Autostep

11. Wet etch of 200 nm SiO_2 from the p-contact region using diluted buffered HF, followed by 1 minutes of rinse in de-ionized water

12. Dip in concentrated HCl for 1 minutes, followed by 30 seconds rinse in de-ionized water, before loading into electron beam deposition chamber for deposition of 2 nm Nickel and 5 nm of Gold

13. Pattern definition on the samples using maskplate CGLED, layer PADO using GCA Autostep

14. Wet etch of 200 nm SiO_2 from the n-contact region using diluted buffered HF, followed by 1 minutes of rinse in de-ionized water

15. Pattern definition on the samples using maskplate CGLED, layer NCONT using GCA Autostep

16. Electron beam deposition of 30 nm of Titanium and 250 nm of Gold

In this chapter so far, the applicability of the GaN on porous GaN PSs to obtain micro-meter scale patterned elastically relaxed InGaN layers and associated primary device level demonstrations were discussed. As mentioned before, these PSs, were attractive not only for relaxed InGaN demonstration, but also for relaxed AlGaN, which will be discussed next.

B. AlGaN relaxation

The (Al,Ga)N material system spans the bandgap of 3.4 eV to 6.1 eV making it attractive for LEDs emitting in the ultra-violet (UV) wavelength range of 210 to 341 nm, generally used in sensing, water purification, sterilization, medical diagnostics, UV curing, lithography, security systems, and horticultural lighting [91]. Owing to their wide-bandgap, AlGaN alloys also find applications in electronic devices specifically high power, high frequency and power switching devices [92], for which large-area AlGaN substrates are highly desirable. Often, high dislocation density films are obtained when grown on readily available substrates like silicon or sapphire [93-94]. Point defects and threading dislocations are the main reasons behind non-radiative recombination in UV LEDs, lowering the internal and external quantum efficiencies [91,93]. Due to the lattice mismatch of 2.5% between AlN and GaN, tensile strain is induced in AlGaN films grown on GaN, which results in cracking of these films [95]. Using lateral overgrowth over buried cracks, plastically relaxed $Al_{0.2}Ga_{0.8}N$ layers have been demonstrated on GaN [96]. Air-bridged lateral growth of AlGaN on porous GaN or AlN base layers has also been demonstrated either to reduce the dislocation density in the films or as a sacrificial layer for flip-chip UV LEDs [97-99]. Low dislocation density bulk AlN substrates can be considered but they are quite expensive and are available in small dimensions only [100]. In this section, growth of elastically relaxed crack-free AlGaN grown on patterned GaN on porous GaN PS is discussed, with a pathway toward a low dislocation density large area cost-effective AlGaN PS for electronic and optoelectronic device applications.

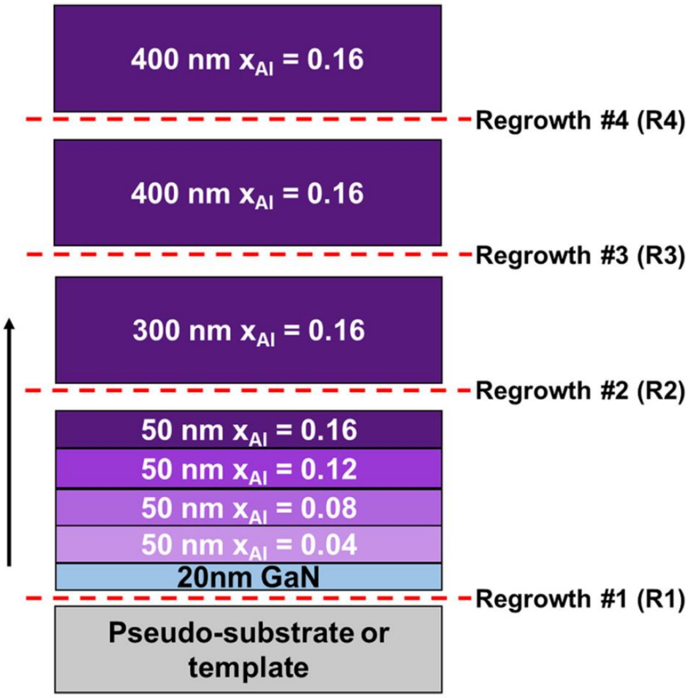

Figure 3.11 Cross-sectional schematic of the GaN on porous GaN PS and co-loaded GaN on sapphire template upon a series of regrowth of AlGaN layers labeled with the regrowth interfaces. After regrowth #1 (R1), cracks were observed on the surface of the GaN on sapphire template. Reprinted with permission from AIP [63].

The fabrication of the 10 µm × 10 µm tile patterned 100 nm thick GaN cap on porous GaN PS, has been discussed earlier in this chapter. Following this fabrication process, the PS was loaded into the MOCVD reactor to perform a series of AlGaN regrowth. The AlGaN layers were grown by MOCVD using Tri-methyl Gallium (TMG), Tri-methyl Aluminum (TMA) and ammonia at a temperature of 1080 °C and a pressure of 100 torr. A GaN on sapphire template was co-loaded with the GaN on porous GaN PS, to serve as a reference sample.

Figure 3.11 shows the compositions of the AlGaN layer that was intended for the growths. For the intended or nominal compositions, the AlGaN growth conditions were calibrated using separate runs on GaN on sapphire templates. The actual compositions on the GaN on porous GaN sample was obtained using XRD measurements after subsequent runs and the morphology was studied using optical microscopes and AFM scans. The first regrowth denoted as R1, was performed both on the GaN on porous GaN PS and the GaN on sapphire template. R1 consisted of an initial 20 nm of UID GaN, serving as a transition layer before the introduction of misfit strain in the structure, followed by 50 nm each of $Al_{0.04}Ga_{0.96}N$, $Al_{0.08}Ga_{0.92}N$, $Al_{0.12}Ga_{0.88}N$, and $Al_{0.16}Ga_{0.84}N$. The precursor flows for the different compositions were 0.98, 1.43, 2.24, and 2.69 µmol/min for TMA and 14.6, 10.2, 10.2, and 8.8 µmol/min for TMG, with a constant ammonia flow of 178 mmol/min. The gas phase molar fraction of aluminum is generally higher than those incorporated in the solid phase when AlGaN is grown strained to GaN due to the pre-reactions between TMA and ammonia [101-103]. The first 20 nm of GaN in R1, along with the 100 nm thick GaN cap layer and the porous layer underneath served as the compliant part of the PS, to relieve the misfit strain between the mismatched layers grown above them and the GaN buffer layer below, as discussed earlier in the chapter. The second regrowth denoted as R2, consisted of 300 nm AlGaN layer with a nominal composition of 0.16. The third and fourth regrowth denoted as R3 and R4 consisted of 400 nm each of AlGaN with same nominal composition of 0.16 as R2. After each regrowth, the sample was characterized with XRD and AFM, hence it was cleaned thoroughly before introducing it back into the MOCVD reactor for the next regrowth. The cleaning steps consisted of a solvent clean first including ultrasonication in acetone followed by in isopropanol, and then a de-ionized water rinse. The sample was then dipped in buffered HF followed by a de-ionized water rinse to get rid of any unintentional oxide layer formation on the surface. The XRD measurements, in this case the reciprocal space maps or RSMs were recorded around the GaN $(\overline{11}24)$ reflection to evaluate the composition and strain state of AlGaN across the tiles.

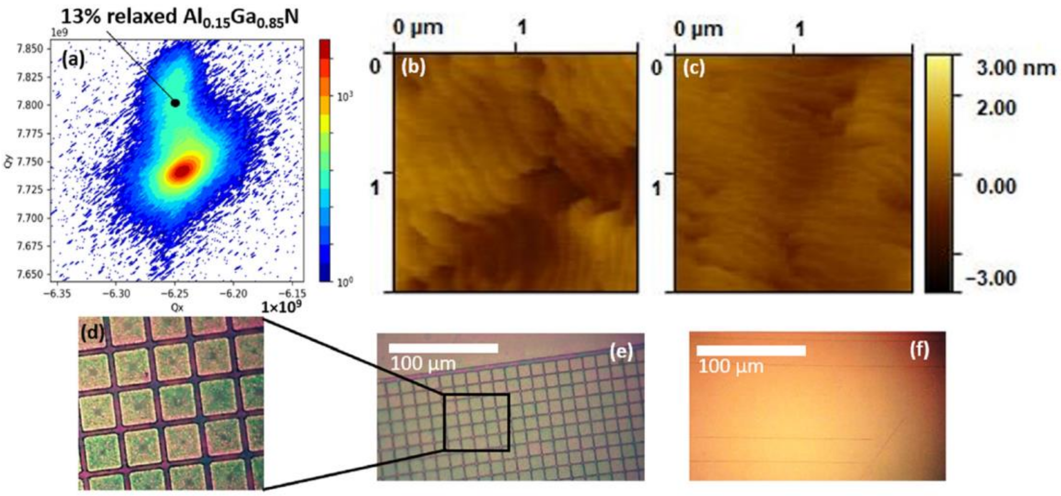

Figure 3.12 (a) RSM of the GaN on porous GaN PS after R1 around the GaN $(\overline{11}24)$ reflection. 2 µm × 2 µm sized AFM scans of the (b) GaN on porous GaN PS on one of the 10 µm × 10 µm sized tiles and (c) crack free region of the GaN on sapphire coloaded wafer after R1, with corresponding microscopy images (e) and (f), zoomed version of (e) is shown in (d). Reprinted with permission from AIP [63].

After the first regrowth step, R1, involving growth of 20 nm UID GaN followed by 50 nm each of $Al_xGa_{1-x}N$ with nominal x_{Al} = 0.04, 0.08, 0.12 and 0.16, cracks appeared on the surface of the co-loaded GaN on sapphire reference sample due to plastic relaxation as shown in figure 3.12 (f), hence this sample was excluded from the next set of regrowths. In contrast, the GaN on porous GaN PS did not exhibit any cracks as shown in figure 3.12 (d) and (e). The AFM images taken on one of the tiles of the GaN on porous GaN PS and on the crack-free region of the GaN on sapphire template, show extremely smooth surface and a root mean square (RMS) surface roughness of below 0.5 nm for both the scans shown in figure 3.12 (b) and (c). Due to the step-graded composition of the epitaxial stack in R1, a diffused set of peaks was observed in the RSM of the GaN on porous GaN PS sample as shown in figure 3.12 (a). A local maximum peak corresponding to 13% relaxed $Al_{0.15}Ga_{0.85}N$ was identified from the RSM. After the second regrowth, R2, involving regrowth of 300 nm of $Al_xGa_{1-x}N$ with a nominal composition of x_{Al} = 0.16, lateral growth at the edge of the square tiles could be observed from optical microscope images as shown in figure 3.13 (c). Comparing this image with the microscopy image of the tiles after R1 in figure 3.12 (d), the gaps between the tiles were reduced after R2. The gaps between the tiles were characterized by the dark vertical and horizontal lines in figure 3.13 (c). The AFM scans acquired from the top of one of the tiles again showed smooth surface morphology, as shown in figure 3.13 (b), with RMS surface roughness below 0.5 nm. The RSM of this sample, showed the emergence of an additional peak corresponding to 63 % relaxed $Al_{0.24}Ga_{0.76}N$ as shown in figure 3.13 (a). A lower composition $Al_{0.09}Ga_{0.91}N$ peak also appeared as a local maximum, which may have been caused by the overlap of various AlGaN peaks from R1 and R2.

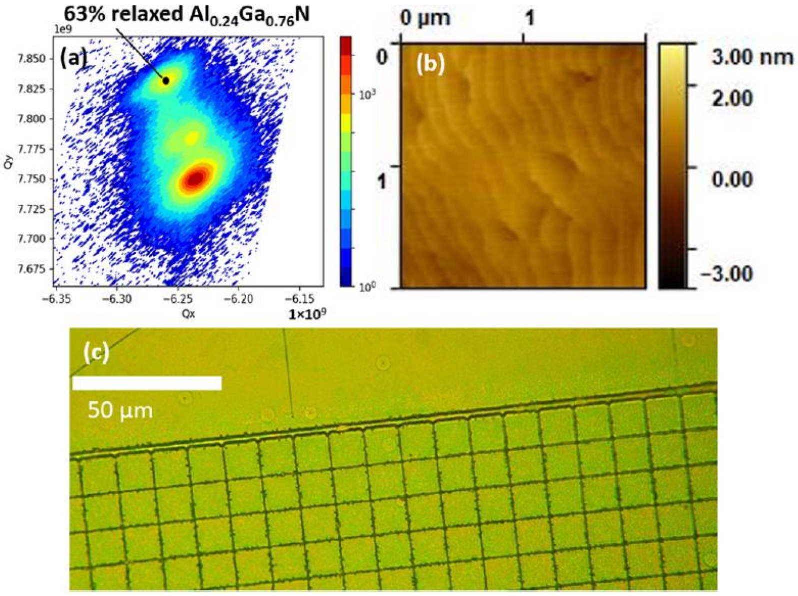

Figure 3.13 RSM of the GaN on porous GaN PS after R2 around the GaN $(\overline{112}4)$ reflection. (b) 2 µm × 2 µm sized AFM scans of the GaN on porous GaN PS on one of the 10 µm × 10 µm sized tiles and (c) corresponding microscopy image, no cracks were observed in the patterned region. Reprinted with permission from AIP [63].

After the third regrowth, R3, involving 400 nm of $Al_xGa_{1-x}N$ regrowth with a nominal composition of 0.16, the gaps between the square tiles were difficult to observe from optical microscopy images as shown in figure 3.14 (c). Hence, AFM scans of larger size of 20 µm × 20 µm were acquired as shown in figure 3.14 (d) to study the area between the tiles. These images confirmed the preferential growth on the top and bottom sidewalls of the tiles, which corresponded to the $(11\bar{2}0)$ AlGaN a-plane, when compared with the orthogonal $(1\bar{1}00)$

AlGaN m-plane sidewalls. This indicated a low lateral growth rate on the m-plane sidewalls compared to the a-plane sidewall as observed in epitaxial lateral growth studies as well [104-105].

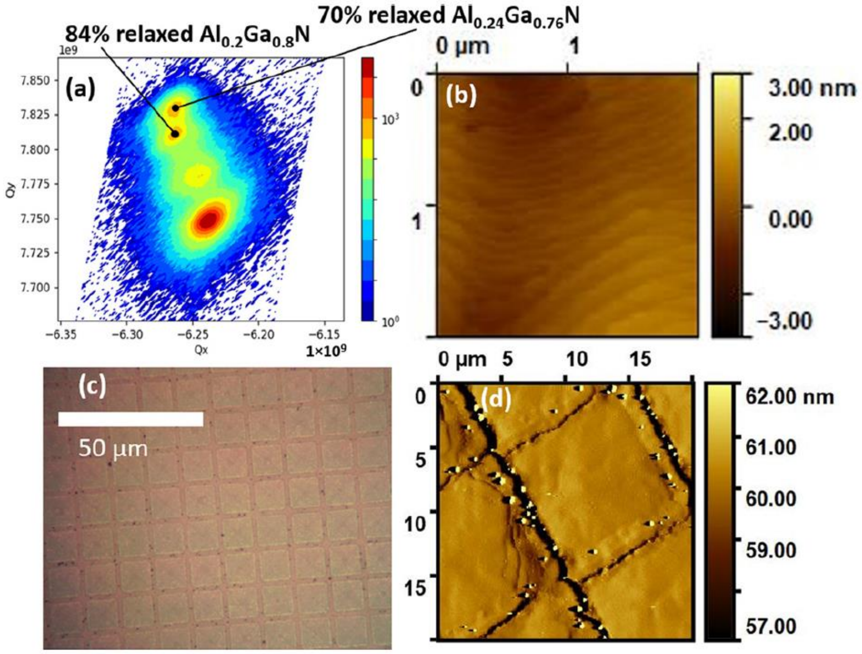

Figure 3.14 RSM of the GaN on porous GaN PS after R3 around the GaN $(\bar{1}\bar{1}24)$ reflection. (b) 2 µm × 2 µm sized AFM scans of the GaN on porous GaN PS on one of the 10 µm × 10 µm sized tiles and (c) corresponding microscopy image, (d) a 20 µm × 20 µm AFM scan confirming the preferential growth on the AlGaN a-plane sidewalls compared to the AlGaN m-plane sidewalls of the tiles. Reprinted with permission from AIP [63].

The RSM of this sample displayed a newly emerged peak corresponding to 84 % relaxed $Al_{0.2}Ga_{0.8}N$ as shown in figure 3.14 (a). The $Al_{0.24}Ga_{0.76}N$ peak was now vertically aligned to the above peak indicating the same lattice constant and this layer was approximately 70 % relaxed. Additionally, from the microscopy images in 3.14 (c), the tiles appeared lighter in color compared to the rest of sample, even though the tiles have almost coalesced with each other, due to a thickness of the underlying porous layers. No cracks could be located from the microscopy images on this sample. After the fourth regrowth, R4, involving 400 nm of $Al_xGa_{1-x}N$ with a nominal aluminum composition of 0.16, very similar observations were made compared to that after R3. No cracks could be observed on the sample surface as shown in figure 3.15 (c), and the 2 µm × 2 µm AFM scan on one of the tiles demonstrated extremely smooth surface with RMS roughness below 0.3 nm as shown in figure 3.15 (b). The larger 20 µm × 20 µm AFM scan showed almost complete coalescence across the AlGaN a-plane sidewall as shown in figure 3.15 (d). In the RSM shown in figure 3.15 (a), a higher intensity peak corresponding to almost 85 % relaxed $Al_{0.18}Ga_{0.82}N$ was observed, which was slightly broadened in shape. The $Al_{0.24}Ga_{0.76}N$ peak also appeared in the RSM, however with a reduced degree of relaxation from ~70 % after R3 to 64 % after R4. Despite the same growth conditions being used for re-growths R2, R3 and R4, much different aluminum incorporation was observed in the sample for each regrowth.

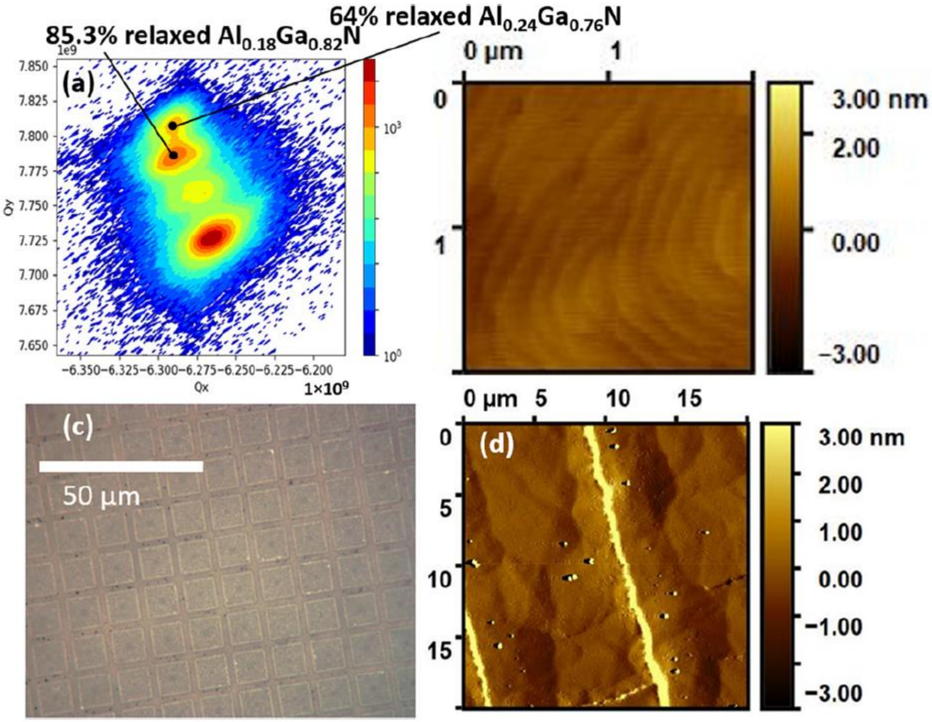

Figure 3.15 RSM of the GaN on porous GaN PS after R4 around the GaN $(\overline{11}24)$ reflection. (b) 2 µm × 2 µm sized AFM scans of the GaN on porous GaN PS on one of the 10 µm × 10 µm sized tiles and (c) corresponding microscopy image, (d) a 20 µm × 20 µm AFM scan confirming complete coalescence across the AlGaN a-plane sidewalls. Reprinted with permission from AIP [63].

After R1, involving a growth of a total of 200 nm thick AlGaN with nominal composition of 0.04, 0.08, 0.12 and 0.16 for 50 nm thickness of each layer, an average aluminum content of 0.1 was observed with a 13% relaxed $Al_{0.15}Ga_{0.85}N$ peak appearing as the local maximum. A subsequent regrowth R2 of 300 nm thick AlGaN with nominal composition of 0.16, resulted in a 63 % relaxed $Al_{0.24}Ga_{0.76}N$ layer. There was a significant enhancement in the actual aluminum incorporation of 0.24 in these films compared to the intended or nominal composition of 0.16, when grown strained to GaN-on-sapphire templates during growth condition calibration runs. There was also an enhancement in the degree of relaxation between regrowths R1 and R2. From equation (2.3) in chapter 2, it is known that the elastic strain energy is directly proportional to the thickness of the epilayers and the square of the misfit strain between the epilayers and the substrate. In the above experiments, as the thickness of the AlGaN layers increased, the degree of relaxation of these layers increased as well to compensate for the increased strain energy in the epitaxial structure. The enhancement in the aluminum incorporation from expected 0.16 to the measured 0.24, was attributed to the reduced lattice mismatch between the layers being deposited during R2 and the presence of partially relaxed AlGaN layers underneath, as observed in previous studies as well [40-41, 106]. The aluminum incorporation reduced from 0.24 after regrowth R2, to 0.2 after regrowth R3 and 0.18 after regrowth R4, even with the same growth conditions. This behavior could be related to the gradual coalescence of the tiles across the AlGaN a-plane sidewalls, enhancing the tensile strain in the structure, resulting in a reduced aluminum incorporation in the tiles due to composition pulling effect [40-41, 106-107]. Another reason could be the onset of the tile coalescence at the bottom portion of the epitaxial structure, where the aluminum content was lower than 0.2, as the lattice constant of the top layer of the structure is nominally the same as that set after the tile coalescence started. Hence, the much higher aluminum uptake was observed only until the tiles were spaced apart from each other. Upon the onset of visible coalescence of these tiles, after R3, the aluminum incorporation achieved was relatively lower than R2, but still higher than the intended or nominal composition obtained when the AlGaN films are grown strained on GaN on sapphire templates for calibration purposes. In some studies, performed on patterned samples, different aluminum compositions have been obtained on the sidewalls compared to the top of the features [108-109]. In this study, the primary focus was on the regions on top of the 10 µm × 10 µm wide tiles, which could be accomplished with the XRD analysis, as the fill factor in these samples was quite high (~ 70%).

The $Al_{0.2}Ga_{0.8}N$ layer grown during R3 was 84 % relaxed and was lattice matched to the 70 % relaxed $Al_{0.24}Ga_{0.76}N$ underneath, and after R4, the 85 % relaxed $Al_{0.18}Ga_{0.82}N$ was lattice matched to the 64 % relaxed $Al_{0.24}Ga_{0.76}N$ layer underneath. The lattice matching lowers the misfit strain between the multiple AlGaN layers and hence reduces the overall elastic strain energy in the epitaxial structure. The above observations suggest that the type of relaxation was elastic, with no visbile indications of crystal defect formation, similar to the observations made for relaxed InGaN layers. The aluminum content could be increased by spacing the tiles further apart, when initially patterning the sample prior to the EC etch. Additionally, if the samples were patterned in a certain shape and aligned carefully for the features to have a-plane sidewalls exclusively, then a fully coalesced large area AlGaN substrate with a desired aluminum content can be achieved. As observed in the relaxed

InGaN study in chapter 2 and earlier in this chapter, smaller feature sizes could also yield a higher degree of relaxation, and hence a higher aluminum uptake. Essentially, this substrate technology allows for lattice constant engineering of AlGaN layers in a micro-meter dimension scale.

In this study growth of 1.3 µm thick elastically strain relaxed crack-free AlGaN was demonstrated on micro-meter scale patterned GaN on porous GaN PS. The patterns coalesced beyond certain thickness of the regrown films under the low-pressure growth conditions, which led to the locking of the lattice constant of these films due to an enhanced tensile strain in the structure. The dislocation density of the deposited AlGaN films is expected to be nominally the same as that of the underlying GaN base layers, hence very low dislocation density can be achieved with the choice of a suitable substrate for the GaN on porous GaN PS. The developed relaxed AlGaN PSs are of particular interest for efficient UV optoelectronic devices and for emerging electronic devices.

IV. Micro-LED process and epitaxial structure optimization

In chapter 3, the GaN on porous GaN PS was discussed for the growth of relaxed InGaN and relaxed AlGaN films. A preliminary device level demonstration was also presented. Both the green and orange micro-LEDs demonstrated served the purpose of establishing the viability of this substrate technology for device level demonstrations. However, the fabrication process utilized for these devices was sub-optimal. The most important steps involved in the fabrication of micro-LEDs are the sidewall formation and the passivation of these sidewalls. Previously, a low damage etch was utilized, however, for the sidewall passivation PECVD dielectric was used, which was detrimental to the luminescence of the devices. Additionally, the use of thin metal p-contacts led to poor current spreading in the devices. In order to achieve the goal of demonstrating efficient red micro-LEDs, it was important to optimize the fabrication steps on relatively more efficient micro-LEDs (blue or green emitting) to ease the identification of the effects of the modified fabrication steps. Hence, in the next section the fabrication process optimization for a green micro-LED is discussed. This section will be followed by the discussion on epitaxial structure optimization to achieve red InGaN micro-LEDs while utilizing the optimized fabrication process, followed by the estimation of IQE, for these devices.

A. Green micro-LEDs

As discussed before, the sidewalls of a micro-LED are formed utilizing a plasma etch chemistry. Hence the etch damage caused is inevitable for devices fabricated with a top-down approach. However, this damage can be reduced either by modifying the etch chemistry or by employing steps to minimize the damage after the etch. In the preliminary fabrication process, a low damage causing 15 W BCl_3/Cl_2 dry etch chemistry was used. A higher RF power used during the etch leads to a higher amount of etch damage on the sidewalls of the features being defined [80]. Even with a low power etch, there is some amount of etch damage in the form of defects, impurities, dangling bonds that result in the formation of surface states positioned within the band gap of the material. These surface states trap charge carriers and act as non-radiative recombination centers. Chemical treatments may be used to reduce the etch damage on the sidewalls. Another method to reduce surface recombination is by depositing a dielectric layer on the sidewalls of the device to lower the non-radiative recombination by lowering the surface recombination. In the preliminary fabrication process as shown in figure 4.1, PECVD sidewall passivation was used. The presence of plasma in the step (c), leads to the compensation of the p-doped nitride layer near the surface, due to the introduction of shallow donor states depending upon the ion flux, mass and energy [110]. The use of thin Ni/Au metal as p-contact also led to a reduced current spreading near the edge of the p-doped layer, and due to the fragile nature of this thin metal contact the metal lift-off was difficult, resulting in low yield for this process.

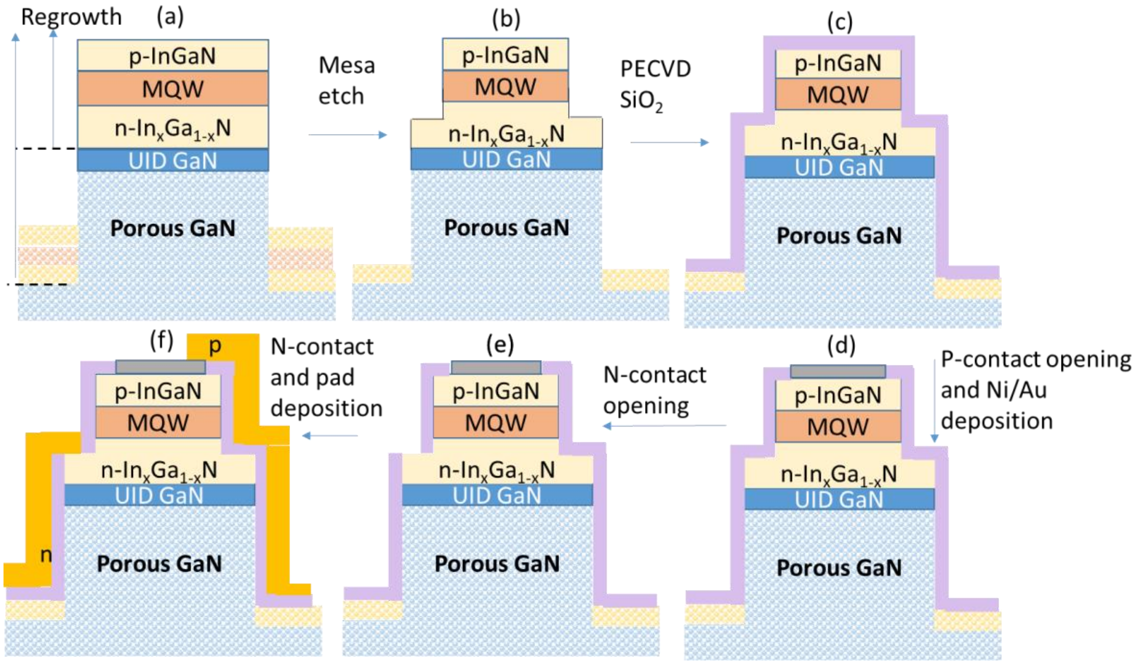

Figure 4.1 The sub-optimal preliminary micro-LED fabrication flow

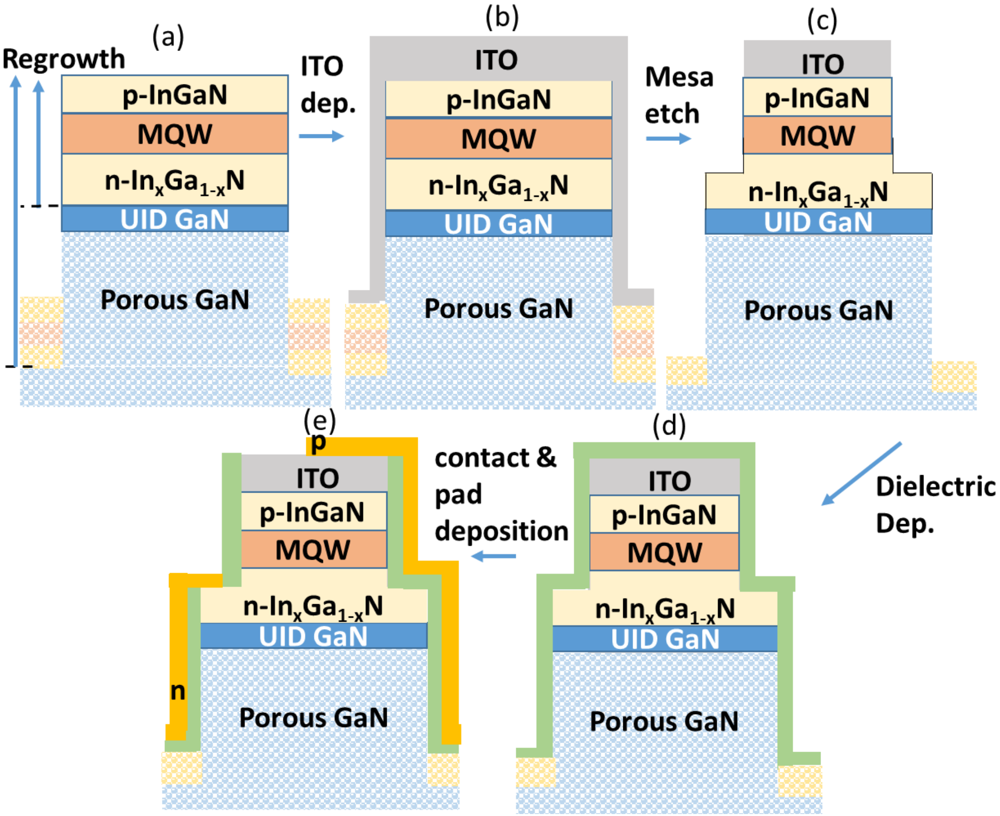

Figure 4.2 The optimized micro-LED fabrication flow

Figure 4.2 shows the optimized fabrication flow. Upon the deposition of the LED epitaxial structure in the MOCVD reactor and thermal activation of the p-doped layer, 110 nm of Indium tin oxide (ITO) was deposited on the sample. Using RIE etch, the device mesas were defined by partially etching into the n-doped InGaN layer. The ITO was etched using a Methane, Hydrogen and Argon etch chemistry, and the nitrides were etched using the low power etch described above. After this step, atomic layer deposition (ALD) was used to deposit 30 nm of Al_2O_3 followed by 200 nm of SiO_2 using sputter deposition technique. Thick dielectric deposition could be performed without exposing the sample to a source of plasma, thereby preserving the surface of the p-doped InGaN. The p and n contact regions were opened using dry etch and 100/ 50/ 100 nm of Al/Ni/Au was deposited for n-contact and probes.

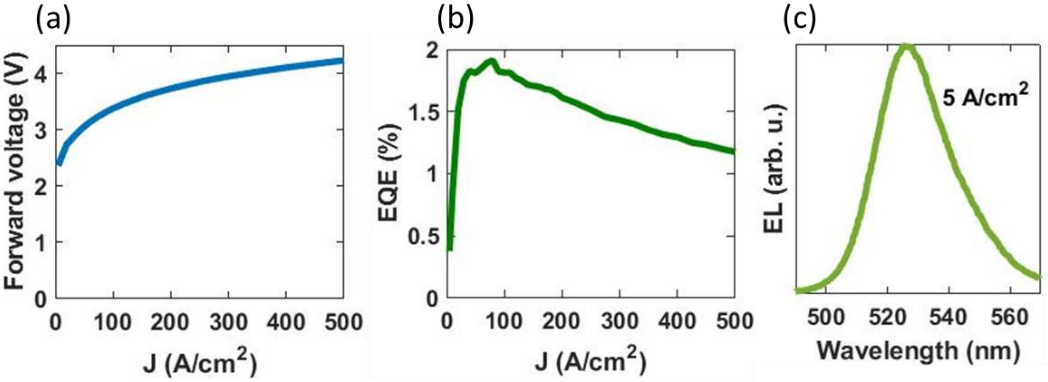

Figure 4.3 (a) IV curve of the 3 µm × 3 µm sized micro-LED with a turn on voltage of ~2.8 V, (b) A peak on-wafer EQE value of 1.91% was achieved at 80 A/cm^2. (c) Electroluminescence spectrum at at 5 A/cm^2 emitting at 528nm.

The sample was characterized with the on-wafer set-up described in chapter 3, with a limited amount of light being collected at the back-side of the wafer. A much more robust device was obtained which could be characterized at very high current densities of 500 A/cm^2, whereas the devices fabricated with the prior fabrication could not be operated beyond 150-200 A/cm^2. A 3 µm × 3 µm sized device was fabricated above a 10 µm × 10 µm wide GaN on porous GaN tile. A turn on voltage of 2.8 V was observed with a peak on-wafer EQE value of 1.91 % at 80 A/cm^2 as shown in figure 4.3 (a) and (b). Emission spectrum could be resolved for current densities as low as 1 A/cm^2. A noise-free spectrum at 5 A/cm^2 is shown in figure 4.3 (c), with a peak emission wavelength of 528 nm. A co-loaded GaN-on-sapphire template on which the same LED structure was deposited, luminesced at only 478nm for 300 µm × 300 µm large area LED. This LED had a substantially less contribution of sidewall damage owing to its large size. A 50 nm redshift was observed between the micro-LED on GaN on porous GaN PS and the reference large LED, which can be attributed to strain relaxation induced enhanced indium incorporation in the MQWs for the former. For a device fabricated using the previous process flow, with same device and tile size and electroluminescence wavelength nominally in the same range, a peak on-wafer

EQE of 0.4 % was obtained at 100 A/cm^2, compared to a peak on-wafer EQE of ~ 2 % at 80 A/cm^2 with the use of the modified process flow. Hence an estimated increase in EQE by 4-5 times was observed by employing these optimized fabrication steps. The use of ITO as the p-contact also made the devices more reliable and improved the yield of the process significantly. The process traveler for the above micro-LEDs was as follows:

1. Solvent clean with ultrasonication of the unporosified GaN on GaN:Si template in acetone, isopropanol followed by rinse using de-ionized water for 3, 2 and 1 minute each.

2. Pattern definition on the samples using maskplate CGLED, layer MESA using GCA Autostep

3. Etch the GaN cap and halfway through the GaN:Si layer using a 100 W BCl_3/Cl_2 RIE etch chemistry

4. EC etch in 0.3 M Oxalic acid for 30 minutes using indium contact pressed onto scratched surface to make contact with the buried GaN:Si layer.

5. Solvent clean as described in step 1, but with low ultrasonication intensity, followed by 4 minutes dip in concentrated HF, and rinse in de-ionized water.

6. MOCVD regrowth of the LED epitaxial structure

7. Dip in a 1:1 mixture of HCl and de-ionized water for 1 minutes, followed by 30 seconds rinse in de-ionized water, before loading into electron beam deposition chamber for deposition of 110 nm of ITO with a heated stage

8. Pattern definition on the samples using maskplate CGLED, layer ISO using GCA Autostep
9. Etch the ITO using Methane, Argon and Hydrogen RIE etch chemistry
10. Etch into the InGaN:Si layer using a 15 W BCl_3/Cl_2 RIE etch chemistry
11. ALD deposition of 30 nm thick Al_2O_3 at 300 °C, followed by deposition of 200 nm thick SiO_2 by sputtering
12. Pattern definition on the samples using maskplate CGLED, layers PCONT and PADO, using GCA Autostep
13. Dry etch of the dielectrics using ICP from the p and n-contact region
14. Pattern definition on the samples using maskplate CGLED, layer NCONT using GCA Autostep
15. Electron beam deposition of 100 nm of Aluminum, 50 nm of Nickel, and 100 nm of Gold

B. Red micro-LEDs

One of the main motivations behind developing this substrate technology was the ability to achieve efficient red micro-LEDs using the (In,Ga,Al)- nitride material system. The incumbent AlInGaP based red emitters have unfavorable material conditions for device scaling, that make the development of efficient nitride based ultra-small red micro-LEDs highly desirable. A detailed discussion on this was included in chapter 1. With the fabrication process fairly optimized, the epitaxial structure needed further optimization. In the next subsection the epitaxial structure optimization will be discussed in detail, followed by a discussion on the device results and finally its light extraction efficiency.

I. Epitaxial structure optimization

In the LED epitaxial structure there are broadly three parts – n-doped layer, active region, p-doped layer. For the composition pulling effect to take effect, it was essential to have the average composition and lattice constant of the regrown stack closer to that of the active region. Hence the n and the p doped layers were chosen to be composed of InGaN rather than the traditionally employed GaN layers. The growth conditions employed for the growth of InGaN:Si do not allow for a pristine morphology, resulting in v-defects. Hence, a modified version of semi-bulk InGaN growth approach was used to achieve high quality thick InGaN film growth [111]. The thick InGaN layers were grown with GaN interlayers as described in chapter 2. For each 37 nm of InGaN, 3 nm of GaN interlayers helped in reducing the size and density of the v-defects.

Sample id	NH_3 flow	H_2 flow during GaN interlayer in N_2/H_2	Observations
1	3 slm	No	Reference
2	1.5 slm	No	V-defect density↓
3	1.5 slm	0.3 slm	V-defect density and size↓
4	3 slm	0.3 slm	Better than 1, worse than 3
5	1.5 slm	1 slm	Best morphology

Table 4.1 Growth condition optimization steps and observations for the InGaN:Si layers

To improve the morphology further the first step was to reduce the InGaN thickness per iteration or increase the insertion frequency of the GaN interlayer. Hence, 26 nm of InGaN followed by 3.5 nm of GaN was used with the same carrier gas of N_2 throughout and 3 slm of NH_3 to be denoted as reference in Table 4.1. These experiments were performed on GaN on sapphire templates.

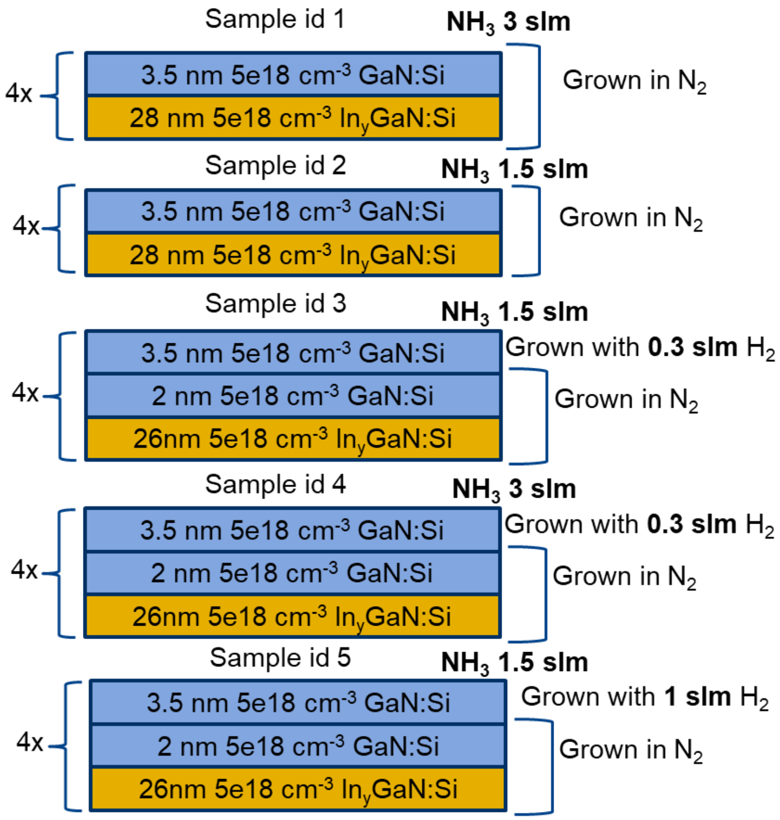

Figure 4.4 Epitaxial structure of the InGaN/GaN modified semi-bulk layers with details of the growth conditions. All layers were grown at 910 °C.

All growths were performed at 910 °C with a TMI flow of 13 µmol/min and TEG flow of 5 µmol/min, with a nominal indium composition 0.04-0.05, and a total InGaN thickness of ~ 126 nm inclusive of the GaN interlayers. Figure 4.4 shows the cross-sectional epitaxial structure and the various parameters that were varied during the growth. Table 4.1 lists the observations for each of these samples. When reducing the NH_3 flow by 50 %, the v-defect density reduced by about 20%, from 3.58×10^8 cm^{-2} in sample 1 to 2.89×10^8 cm^{-2} in sample 2. A similar observation was made when the NH_3 flow was reduced in the InGaN layers grown on InGaNOS substrates [112].

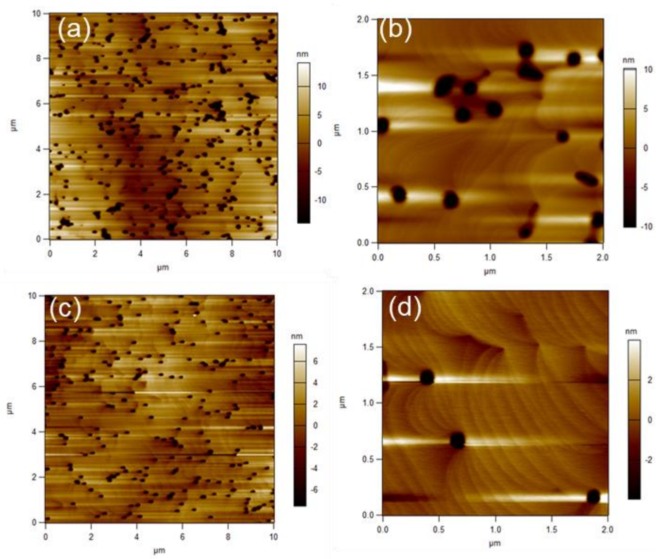

Figure 4.5 10 μm × 10 μm (a),(c) and 2 μm × 2 μm (b),(d) AFM scans of samples 1 and 5 as described in Table 4.1. RMS roughness for (b) was ~ 5 nm and for (d) was ~ 2 nm

The authors attributed this result to the enhanced lateral mobility of Gallium and Indium species due to a low V/III ratio because of the reduced NH_3 flow. This led to an enhanced lateral growth on the sidewalls of the v-defects, hence slowing down the nucleation of new v-defects. In sample 3, 0.3 slm out of the total 5.5 slm N_2 carrier gas was replaced with H_2, during the growth of the GaN interlayer. The presence of hydrogen in the ambient enhances the surface mobility of the reactants through diffusion and also reduces impurities by etching them off the surface [112]. However, it is common knowledge that the presence of hydrogen, reduces the indium incorporation in InGaN layer [113], hence a 2 nm thick GaN layer grown only in the presence of N_2 carrier gas, was used to terminate the 26 nm thick InGaN layer growth. Contrary to expectations, only a minor decrease in v-defect densities and size was observed in sample 3 compared to sample 2. When increasing the H_2 flow to 1 slm, a 40 % reduction in the v-defect density from 3.58×10^8 cm^{-2} in sample 1 to 2.17×10^8 cm^{-2} in sample 5, was observed. For the same set of samples the average v-defect size also reduced from 85 nm to 50 nm. The RMS surface roughness extracted from the 2 μm × 2 μm

AFM scans of samples 1 and 5, were 5 nm and 2 nm, respectively. Hence, it was concluded that the H_2 flow was not enough during the growth of sample 3, to produce the drastic improvement in the v-defect density as observed in sample 5. In sample 4, the low H_2 carrier gas flow of 0.3 slm during the GaN interlayer growth and high NH_3 flow of 3 slm, produced the expected result of minimal improvement in morphology over the reference sample 1. Hence, the high H_2 carrier gas flow of 1 slm, and a low NH_3 flow rate of 1.5 slm, in the presence of 4.5 slm of N_2 carrier gas was found to be the most optimized growth condition for 126 nm thick InGaN growth. An elevated growth temperature (+ 50 °C) of the 3.5 nm GaN interlayer did not lead to further improvement in the surface morphology, contrary to the observations made in [112], which may be attributed to the reactor condition fluctuations during these growths and need to be studied more extensively.

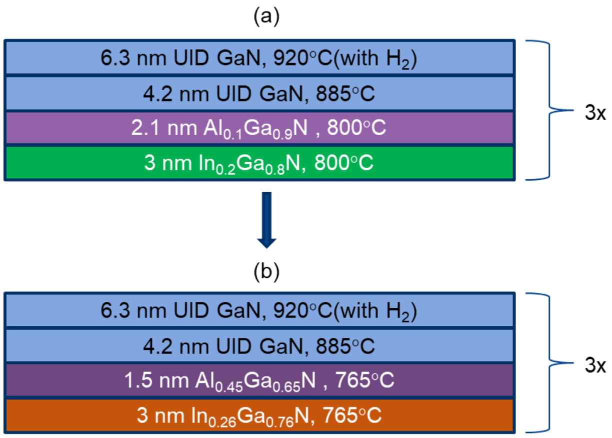

Figure 4.6 The growth temperature, nominal composition, and thickness of the quantum well and barrier layers for the (a) green micro-LEDs (b) red micro-LED

Using the above optimized growth conditions, even thicker layers were grown during the LED epitaxial structure growth on the GaN on porous GaN PS, which will be discussed in in the next section. Similar growth technique was utilized for the Mg doped p-type InGaN layers above the active region. The active region growth conditions and composition used for the green/orange micro-LED on the GaN on porous GaN PS, discussed in the previous chapter is shown in figure 4.6 (a). On planar GaN on sapphire templates these layers luminesced in the cyan range. Hence, to optimize the active region for red micro-LEDs on the GaN on porous GaN PSs, the active region was optimized for efficient yellow emission on the GaN on sapphire templates.

GaN on sapphire templates were solvent cleaned and used to regrow LED structures. Upon thermal activation, indium dot p-contact and soldered indium on a scratched region of the wafer were used as n-contact, to measure on-wafer EQE serving as a quick feedback for the grown samples. The light was captured from the backside of the wafer using a silicon photodetector and the electroluminescence wavelength was captured using a fiber optic detector. Using a power supply on a probe station, a series of samples grown with different growth conditions could be quickly tested to verify the relative trends, without following the fabrication process. To incorporate higher indium content in the quantum well, reduction of the growth temperature for both the well and the AlGaN barrier layer, while keeping the AlGaN layer composition the same, led to very low intensity of emission from the GaN on sapphire templates. Multiple growth conditions were tested, and it was found that a thinner AlGaN cap layer with a higher aluminum composition led to a relatively efficient amber emission from the GaN on sapphire templates, specifically increasing the x_{Al} from 0.1 to 0.45, while keeping the growth temperature the same as the quantum well growth temperature of 765 °C. Similar trends were observed in prior reports on longer wavelength LEDs on conventional c-plane substrates [114-115]. These epitaxial structure optimizations were used together with the developed fabrication process to achieve efficient red emission on GaN on porous GaN PSs, discussed next.

II. Device results and discussion

In chapter 1 the motivation behind the goal of achieving red InGaN micro-LEDs was discussed. The AlInGaP material system suffers from low barrier height induced high temperature carrier loss and is difficult to scale for cost effective commercialization, as discussed in detail in chapter 1. The GaN on porous GaN substrate technology was developed, micro-LEDs were demonstrated on these substrates, the fabrication process was optimized and lastly the active region and semi-bulk InGaN growth conditions were optimized. Before discussing the results, it is important to quantify the desirable metrics for a red micro-LED that would attract attention of industry and get this technology considered for commercialization. The first metric was the external quantum efficiency or EQE of the device which must be above 5% to be attractive for industry. This number was obtained from our industry partners and translates to about 1% for on-wafer EQE measurement. A lower EQE figure obtained when measuring on-wafer is due to the lower amount of light captured by the detector compared to the conventional method of reporting EQE in an integrating sphere. A complete analysis of the light extraction of the on-wafer set-up is discussed with the device results, later in the chapter. Secondly, when the brightness of an LED in a display needs to be enhanced, usually the current density of the device is increased. This increase in the current density also leads to a blueshift in the emission wavelength for conventional c-plane LEDs, as was observed for the green and orange emitting micro-LEDs in figures 3.9 (c) and 3.10 (b) in the previous chapter. An ideal red LED must have blueshift below 20 nm to maintain the color fidelity of the display. Next, the device must emit beyond the pure red wavelength of 630 nm at its peak efficiency, to ensure accurate image reproduction in the displays (as per the Rec. 2020 display standard). And finally, the fullwidth at half maximum value of the electroluminescence must be below 40 nm for a saturated color emission. With these metrics as reference, the fabricated device was characterized and benchmarked.

A GaN on porous GaN PS with 11 µm × 11 µm wide tiles was fabricated using patterning with a dry etch chemistry and EC induced porosification as discussed in detail in chapter 2 and 3. As discussed before, separate calibrations were performed on GaN on sapphire templates followed by characterization using XRD, to obtain the nominal composition and thickness of each layer. The LED epitaxial structure was composed of 440 nm of $In_{0.04}Ga_{0.96}N$:Si as the n-contact layer, using the modified semi-bulk InGaN growth technique as discussed in the previous section. After the n-doped layer. The active region was deposited which consisted of 3 nm of $In_{0.26}Ga_{0.76}N$, 1.5 nm of $Al_{0.45}Ga_{0.55}N$, and 11 nm of UID GaN barrier layer. When grown on GaN on porous GaN PS, a higher indium content was expected in the quantum wells, due to strain relaxation in the thick n-$In_{0.04}Ga_{0.96}N$ layer, enabling enhanced indium incorporation due to a reduced composition pulling effect. The InGaN quantum well and the AlGaN cap layer were both grown at 765 °C, with N_2 as the sole carrier gas. The GaN barrier layer was grown in two steps. The first 4 nm was grown at 885 °C with N_2 carrier gas, and the rest was grown at 920 °C in a mixture of H_2 and N_2 carrier gases, with gas phase ratio of 1:10, respectively. 120 nm of $In_{0.02}Ga_{0.98}N$:Mg was grown above the active region, utilizing the modified semi-bulk InGaN growth technique, followed by a 16 nm thick p+ doped $In_{0.02}Ga_{0.98}N$: Mg contact layer.

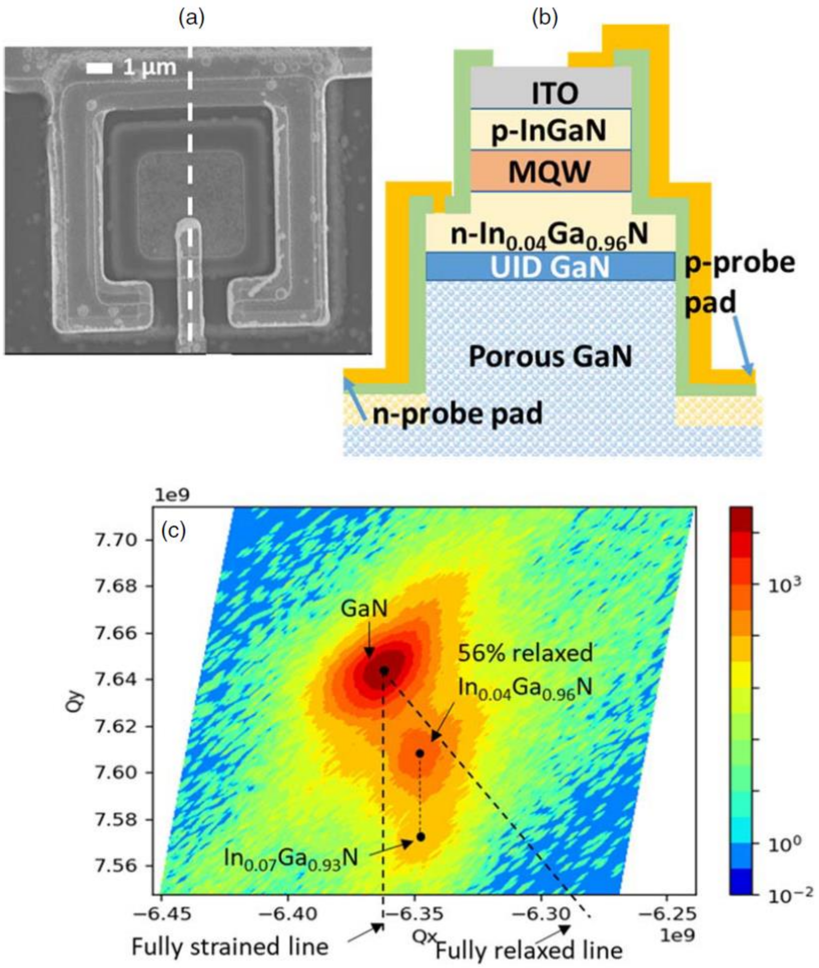

Figure 4.7 (a) The top-view SEM image of the red µLED with porous underlayers and the cross-sectional schematic across the dotted white line is shown in figure (b). (c) High-resolution X-ray diffraction (ω–2θ)–ω reciprocal space maps (RSMs) were recorded around the GaN ($\overline{112}4$) reflection. Reprinted with permission from JSAP [64].

Following the growth of the LED structure, the optimized fabrication process (as shown in figure 4.2) was used to obtain the red micro-LEDs on the 11 µm × 11 µm, and orange/yellow emitting micro-LEDs on the non-porous region of the sample. 110 nm of ITO was deposited by electron beam deposition, and low power etch was utilized to etch the sidewalls to obtain the 6 µm × 6 µm sized active regions. ALD and Sputter deposited dielectric layers were utilized which were dry etched to deposit the 100 nm Al/ 50 nm Ni and 100 nm Au metal stack for n-contact and probes using electron beam deposition. The top view SEM image of the fabricated device is shown in figure 4.7 (a), with the cross-sectional view across the white dotted line shown in figure 4.7 (b).

To investigate the strain state and composition of the $In_{0.04}Ga_{0.96}N$: Si layer on the porous tiles, a GaN on porous GaN sample comprised entirely of 11 µm × 11 µm patterns with a high fill factor of ~ 70 % was fabricated, followed by the deposition of only the 440 nm thick $In_{0.04}Ga_{0.96}N$: Si layer. The high fill factor aided the reliable acquisition of the composition and strain state from the RSMs acquired using XRD. Figure 4.7 (c) shows the RSM of this layer, wherein a 56 % relaxed $In_{0.04}Ga_{0.96}N$ layer was observed with a high intensity accompanied by a low intensity peak of $In_{0.07}Ga_{0.93}N$ strained to the previous layer. Deposition of a thick low composition InGaN layer, led to the increase of indium content from 0.04 to 0.07, which resulted in superior surface morphology and device results, compared to our prior approach of thinner, higher composition n-$In_{0.09}Ga_{0.91}N$ layers resulting in inefficient orange micro-LEDs (chapter 3).

On-wafer measurements were conducted with light being collected from the back-side of the substrate (set-up description in chapter 3). These devices were not covered with a mirror to enhance the light extraction from the backside. Additionally, the limited collection angle of 60 % and lack of other light extraction enhancements such as use of silicone encapsulation on a reflective base, lead to a lower on-wafer EQE value compared to the conventional method of reporting EQE. Typically, the device under test is diced, wire bonded onto a reflective header, and encapsulated with a silicone resin with a refractive index high enough to extract the maximum possible amount of light. This assembly is then placed in an integrating sphere where approximately 60-70% of the total light emitted from the device active region is captured. To find the downscaling factor from the encapsulated device measured in an integrating sphere to the bare device measurement on-wafer, an ultra-efficient blue micro-LED sized 20 µm × 20 µm was first characterized using the on-wafer EQE set-up followed by encapsulation and measurement in the integrating sphere. A downscaling factor in the range of 3-5 was observed, which implies that an on-wafer measured EQE of 1 % could be estimated to have an absolute EQE of 3-5% when encapsulated and measured in an integrating sphere, with the exact EQE value depending upon the topology of the device and the sensitivity of the integrating sphere. As mentioned before, the on-wafer measurement set-up served as a quick feedback for testing the devices and designing the next steps our experiments. Additionally, there were difficulties in reliably characterizing ultra-small micro-LEDs (< 20 µm laterally) with low light output power (as is the case with longer wavelength nitride micro-LEDs), in comparison to ultra-efficient and relatively larger blue and green micro-LEDs in an integrating sphere due to a higher noise floor (power) of its detector.

The electroluminescence spectra of the red micro-LED with porous underlayers, to be referred to as device ‘A’, could be resolved down to 1 A/cm^2 as shown in figure 4.8 (a). The micro-LED without the porous underlayers on the same wafer, with the same active region dimension, to be referred to as device ‘B’, was also characterized. The peak emission wavelength as a function of current density for both these devices is shown in figure 4.8 (b), along with the FWHM of the electroluminescence spectra at each current density for device ‘A’. The electroluminescence snapshots at 5 A/cm^2 for both these devices is shown in figure 4.8 (c). The emission across the red micro-LED appeared uniform, however due to the presence of vibrations during the measurement, a sharper image could not be captured.

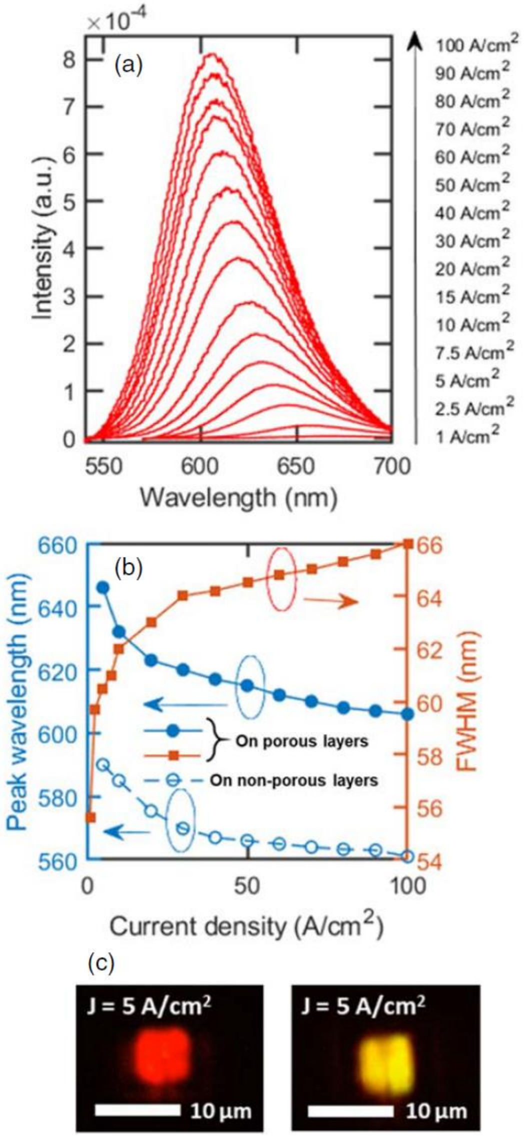

Figure 4.8 (a) Electroluminescence of the red micro-LED corresponding to different current densities as shown in the figure. (b) The peak wavelength of emission for the red micro-LED fabricated on the region of the die with porous underlayers—device “A” (solid circles) and that for the yellow micro-LED without porous underlayers—device “B” (hollow circles) with respect to the injection current density. The longer wavelength emission from device “A” in comparison to device “B” is attributed to enhanced indium incorporation efficiency due to strain relaxation. The FWHM of the red micro-LED (solid squares) as shown in (b) varied from about 56–66 nm with increasing current density. (c) Snapshot of the electroluminescence for the red micro-LED (left) and the yellow micro-LED (right) at 5 A cm^{-2}. Reprinted with permission from JSAP [64].

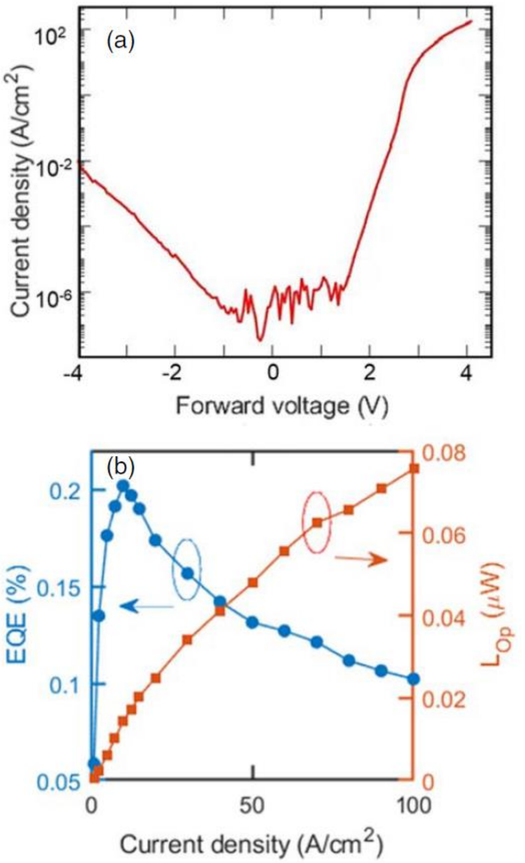

Figure 4.9 (a) J–V characteristics of the device. (b) EQE (solid circle) and L_{Op} (solid square) as a function of injection current density. Reprinted with permission from JSAP [64].

At 5 A/cm^2, device ‘A’ emitted at 646 nm compared to 590 nm for device ‘B’. The reduced lattice mismatch between the partially relaxed n-InGaN base layer and the quantum wells in device ‘A’, led to an enhanced indium incorporation resulting in the longer wavelength emission compared to device ‘B’, wherein the n-InGaN layer was grown strained to GaN. Utilizing growth conditions suitable for achieving orange to yellow emission on GaN on sapphire templates, red emission could be obtained as anticipated using the GaN on porous GaN PS. These PSs enable higher indium content incorporation at a relatively higher growth temperature, resulting in reduced defect densities and hence efficient devices. At 10 A/cm^2, device ‘A’ emitted at 632 nm and at 100 A/cm^2 the emission wavelength was 606 nm, a 26 nm blueshift. The blueshift is usually observed for c-plane LEDs due to band filling effects and piezoelectric field screening effects [116-117]. The FWHM of the electroluminescence spectra of device ‘A’ increased from 56 to 66 nm with the increase in current density from 1 to 100 A/cm^2. A similar range has been observed in prior reports on red InGaN LEDs [116-117] and has been attributed to the heat generated due to non-radiative processes in the active region [85].

A semi-log plot of the IV characteristics for device ‘A’ is shown in figure 4.9 (a). The turn on voltage for this device was ~3 V, and the peak on-wafer EQE measured for this device was ~ 0.2 % at 10 A/cm^2 current density, as shown in figure 4.9 (b), with an emission wavelength of 632 nm. Based on the downscaling comparison factor of measurement of an encapsulated device in an integrating sphere versus on-wafer EQE measurement using our set-up, an EQE of > 0.6 % can be expected from this device when measured using the former method. In the measurement range the maximum light output power (L_{Op}) measured was 75.5 nW at 100 A/cm^2, with the device demonstrating stable and repeatable light output behavior for ~1000s of continuous operation, repeated 3 – 4 times, indicating a highly robust device. The area normalized light output power for this device was 2.1 mW/mm^2 for this 6 µm × 6 µm sized InGaN red micro-LED. The smallest demonstrated state of the art (involving sidewall treatment to recover EQE drop) AlInGaP micro-LED sized 20 µm × 20 µm demonstrated an area normalized light output power of 1.75 – 2 mW/mm^2 at 100 A/cm^2 [23]. This device was also characterized on-wafer, however due to the absorbing nature of the GaAs substrate, the light was measured from the top side of the device, whereas the InGaN devices were measured from the backside of the substrate. The wavelength of emission for these two devices was also quite different at 100 A/cm^2, for the InGaN device it was 606 nm whereas for the AlInGaP device it was 632 nm. Considering these differences, it is difficult to directly compare these results, however it demonstrates the potential of InGaN red micro-LEDs, as comparable area normalized light output power was detected for a device 11 times smaller in size compared to the state-of-the-art smallest demonstrated AlInGaP red micro-LED. To the best of our knowledge, the demonstrated red InGaN micro-LED is the smallest red micro-LED in the world, with a measurable EQE figure. Compared to the state of the InGaN micro-LEDs demonstrated so far, very recently a 50 µm × 50 µm sized red micro-LED was demonstrated on partially relaxed InGaN PSs (InGaNOS) by Soitec [45]. Using on-wafer measurement set-up very similar to ours, a peak on-wafer EQE of 0.09 % was reported at a current density of 40 A/cm^2 with a peak emission wavelength of 616 nm. Our device being almost 70 times smaller in area, demonstrated more than twice the on-wafer EQE while emitting at longer emission wavelength.

Metrics	Target for commercialization	This work
On-wafer EQE	1-2%	0.2 % (previously 0.001%)
Blueshift in emission from 10 to 100 A/cm^2	20 nm	~ 25 nm
λ @ peak EQE	> 630 nm	632 nm
FWHM @ peak EQE	< 40 nm	60 nm

Table 4.2 Benchmarking results for the 6 µm × 6 µm InGaN red micro-LED on GaN on porous GaN PS

Benchmarking the device results with the metrics for commercialization as discussed earlier, the targets for blueshift in emission and the wavelength of emission at peak EQE were nominally achieved. However, the FWHM of emission at the peak EQE and the EQE figure needed significant effort for improvement. Nevertheless, compared to our previous result of orange micro-LED with an EQE 0.001 %, two order of magnitude of improvement was made. Therefore, with this technology, further epitaxial structure and fabrication process optimization can help in achieving the targets for commercialization soon.

III. Estimation of the light extraction and internal quantum efficiency

Ray tracing software was used to estimate the light extraction efficiency (LEE) of our device structure. The on-wafer EQE was then used to extract the internal quantum efficiency (IQE) of the device. To use the ray tracing method, it was important to know both the measurement set-up and the optical properties of each of the layers that the emitted light rays encounter on their path to the detector such as the substrate, UID GaN, doped GaN, porous GaN, ITO, etc. Except for the porous GaN layer, the optical properties for all the other layers were readily available in the literature. To estimate the refractive index of the porous GaN layer, available information in the literature was used and few assumptions were made, as discussed below.

The scattering factor χ, for a porous medium is defined as [68]:

$$\chi = \pi d/\lambda \tag{4.1}$$

where, d is the pore diameter, and λ is the wavelength of the emitted light. For the current study, an average value of ‘d’ to be ~ 50 nm, and λ = 630 nm was assumed. The χ for this case was ~ 0.25 for air bubbles randomly distributed in GaN. For a scattering factor of ~ 0.25, the index of refraction for porous GaN can be estimated as follows [118]:

$$\eta_{eff,porous\ GaN} = \sqrt{(1-\phi)\eta_{GaN}^2 + \phi\eta_{air}^2} \tag{4.2}$$

where, $\eta_{eff,porous\,GaN}$, $\eta_{\,GaN}$, and $\eta_{\,air}$ are the indices of refraction of porous GaN, continuous GaN, and air, and ϕ is the porosity of GaN. In this work, ϕ = 0.5, and at λ = 630 nm, $\eta_{\,GaN}$ = 2.325 [119] and $\eta_{\,air}$ = 1, hence $\eta_{eff,porous\,GaN}$ = 1.78964.

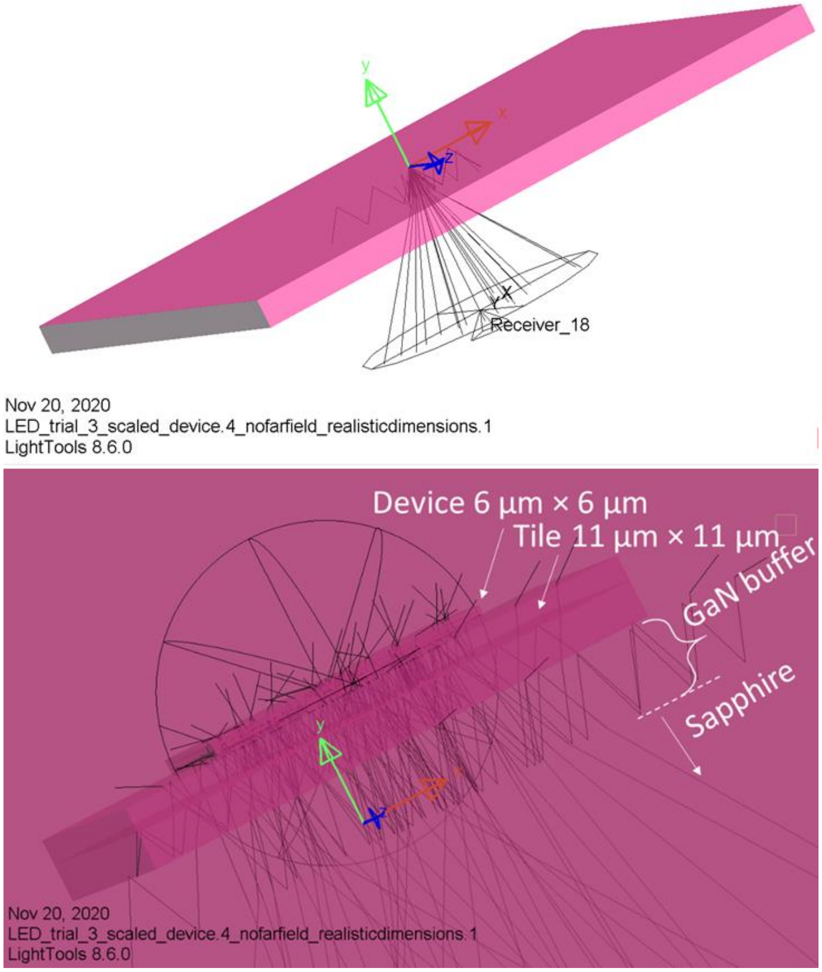

Figure 4.10 (top) Zoomed-out view of the device simulation structure with the circular receiver at the back of the substrate, (bottom) zoomed-in view of the device

Using this index of refraction for porous GaN, ray tracing simulations were performed using Synopsys LightTools software. The electroluminescence spectrum at the peak EQE was utilized as the source, and a simplified model of our device was constructed (metal contacts and dielectric layers excluded) as shown in figure 4.10. In the figure, the path of only 100 rays has been shown for ease of visualization, whereas for the actual simulation 500,000 rays were used to acquire the nominal LEE for our device. The relationship between different LED efficiencies is as follows:

$$\eta_{EQE} = \eta_{injection} \times \eta_{IQE} \times \eta_{LEE} \qquad 4.3$$

where, η_{EQE}, $\eta_{injection}$, η_{IQE}, and η_{LEE}, are the EQE, Injection efficiency, IQE and LEE, respectively. The η_{LEE} from the simulation was 7.266 % or ~ 7.3 %, hence assuming the injection efficiency was 100 %, the η_{IQE} = ~ 2.75 %. This value was low and needs further improvement.

In conclusion, measurable on-wafer EQE was demonstrated for the first time for red micro-LEDs dimensioned below 10 µm. Metrics for commercialization were identified and our device was benchmarked against them. Few metrics such as the FWHM of the electroluminescence spectra and the on-wafer EQE figure need significant effort, but this technology has the potential for commercialization based on these noteworthy demonstrations at such early stages of development, even comparable to the state-of-the-art smallest demonstrated red emitting phosphide micro-LEDs.

V. Future directions and conclusion

In the previous chapter, state-of-the-art InGaN red micro-LEDs were discussed. These devices had an on-wafer EQE of 0.2 %, with LEE of ~7.3 %, emitting at 632 nm and 10 A/cm^2 current density. These devices had a blueshift in emission of about 25 nm when the current density changed from 10 to 100 A/cm^2. Despite these record results, there are ample avenues of improvement for this device discussed in the next section. Later, a modified version of the GaN on porous GaN PS will be discussed, which was developed without the need for tile patterning, simplifying the PS fabrication process. Lastly, some attempts to understand the mechanical aspects of the GaN on porous GaN PS, will be discussed.

A. Scope for improvement of red micro-LEDs

The devices demonstrated had a large FWHM for the electroluminescence spectra. Efforts to enhance the electron and hole wavefunction overlap and reduction in phase separation by carefully controlling the growth conditions, can help reduce the FWHM obtained. Additionally, the thermal activation of the p type doped InGaN, and the doping for both the p and n-type InGaN need extensive experiments to determine their optimum conditions and levels, respectively, as a series resistance could be observed from the semi-log JV characteristics of the red micro-LED in figure 4.9 (a). To improve the internal quantum efficiency, the active region needs to be designed carefully, especially the growth rate, temperature, thicknesses, and compositions of the well, AlGaN cap and the GaN barrier layers. In terms of fabrication, chemical treatments on the micro-LED sidewall can be beneficial in reducing the size dependent EQE lowering trend [120]. In terms of the porous GaN substrate technology, from the TEM cross-section of the tiles, in figure 2.16 (a) and 3.5 (a), the non-uniformity of the porosity could be observed. Although the effect of the non-uniform porosity is yet to be determined, an effort to have uniform porosity along the lateral dimension of the substrate has been discussed in the next subsection.

B. Planar porosification and coalescence of porous GaN

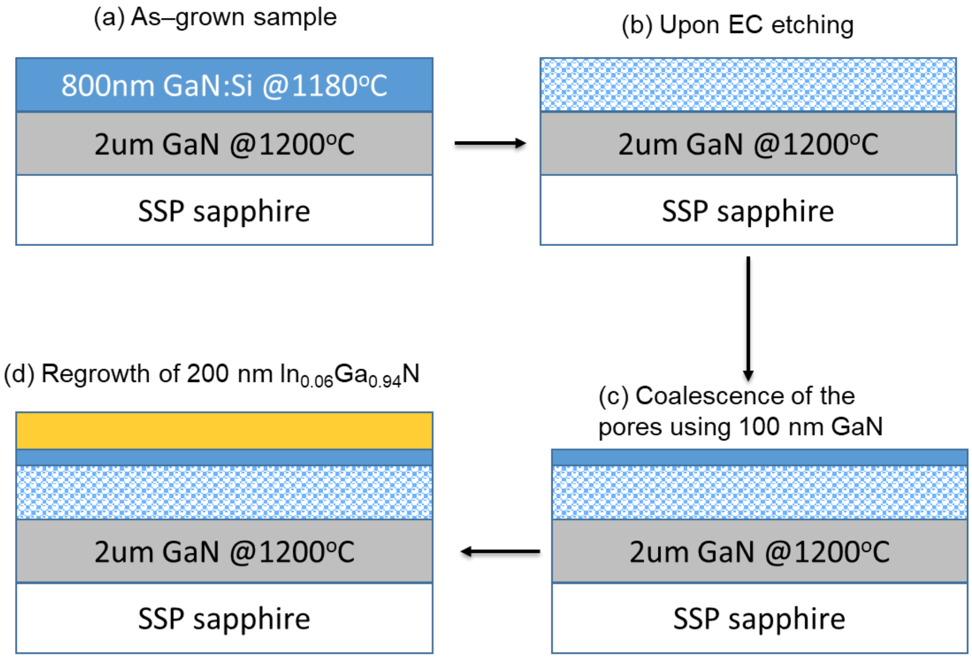

Figure 5.1 Cross-sectionals schematics of the steps involving the fabrication of (b) planar porous samples from (a) as grown nominally strain-free GaN on sapphire templates, using EC etching of the GaN:Si layer. (c) Planarization using a thin GaN cap layer, (d) followed by growth of 200 nm thick InGaN layer.

The porosification of the GaN:Si layers could be achieved either from the sidewalls or from the top surface. In the standard fabrication flow used so far, a buried GaN:Si layer, hence the sidewall porosification technique was preferred. However, terminating the base layer growth with the 800 nm thick GaN:Si layer allows for the porosification of the GaN:Si from the top surface as shown in figure 5.1 (a) and (b). The top side porosification may help reduce the non-uniformity in the pore diameter and hence the non-uniformity in the porosity across this underlayer, below a device. The top view SEM of a planar porous samples is shown in figure 5.2 (a). After subjecting the sample to a thorough solvent and acid clean, it was inserted back into the MOCVD reactor. Various growth conditions involving use of a different MO precursor (TMG and TEG), different MO precursor flow rates (for both TMG and TEG), growth temperatures (950 – 1080 °C), different NH_3 flow rates (1 – 5 slm), and varying flows of H_2 and N_2 carrier gases, were examined. Upon sample characterization, it was revealed that 100 nm of GaN grown at 1080 °C under a pressure of 760 torr, with a TEG flow of 5 µmol/min and NH_3 flow of 3 slm in the presence of 2 slm of H_2 yielded the most planar surface morphology. The schematic structure of the sample at this point in the fabrication flow is shown in figure 5.1(c) and the top view SEM image and 10 µm × 10 µm wide AFM scan of the same are shown in figure 5.2 (b) and (c), respectively. Majority of the dense pores observed on the planar porous sample in figure 5.2 (a), could be planarized using the growth conditions described above. Following characterization, the sample was again cleaned and inserted into the MOCVD reactor. 200 nm thick InGaN with a nominal composition of 0.06 was deposited at 910 °C, using the modified semi-bulk InGaN growth technique described in the previous chapter. The schematic structure of the sample at this stage is shown in figure 5.1 (d) and a 10 µm × 10 µm wide AFM scan of the same is shown in figure 5.2 (d). The RMS surface roughness of this sample was ~ 8 nm, and many v-defects could be observed as was expected for 200 nm thick $In_{0.06}Ga_{0.94}N$. A cleaned GaN on sapphire wafer was also co-loaded with this sample to examine the difference in the surface morphology between these samples. The 10 µm × 10 µm wide AFM scan of this sample is shown in figure 5.2 (e), wherein a higher density of v-defects was observed.

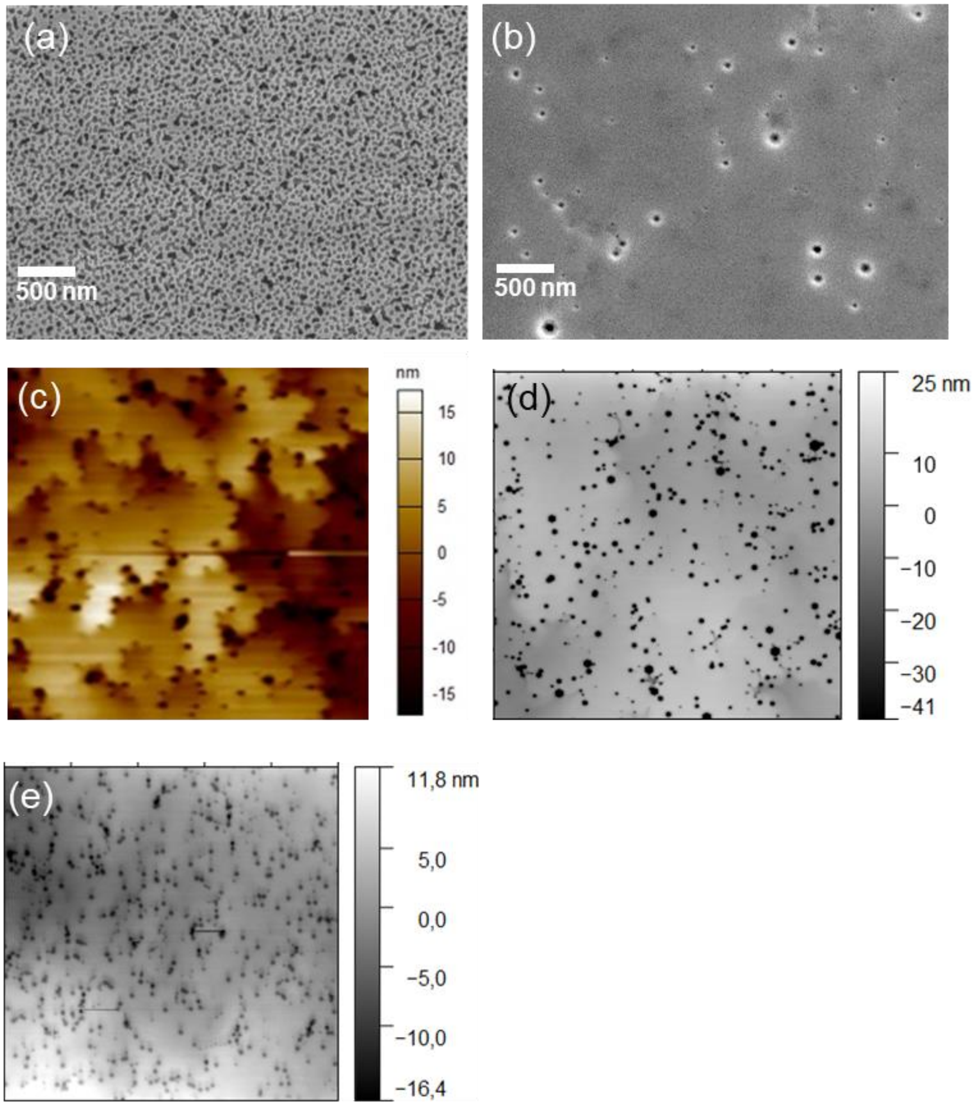

Figure 5.2 Top view SEM image of the (a) planar porous sample after the EC etch and (b) After the planarizing 100 nm GaN layer growth. 10 µm × 10 µm sized AFM scans of the sample (c) after the growth of the 100 nm GaN layer directly on the porous GaN, (d) after the regrowth of the 200 nm thick InGaN layer above the planarizing GaN layer. (e) 10 µm × 10 µm sized AFM scan of the co-loaded GaN on sapphire reference wafer after the 200 nm thick InGaN growth. AFM scans in (d) and (e) acquired by Weiyi Li.

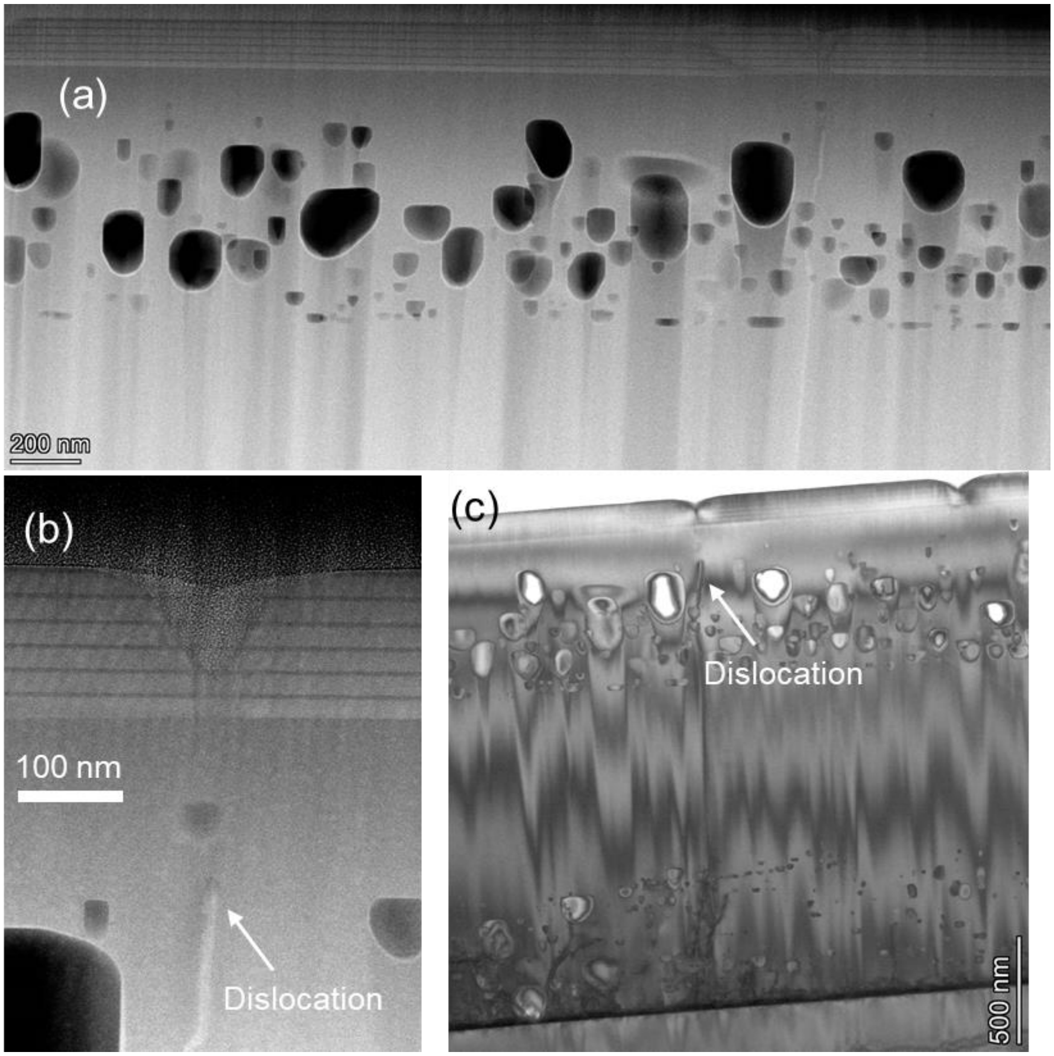

Figure 5.3 (a) HAADF TEM image of the cross-section of the sample with 2 µm thick UID GaN buffer layers, 800 nm thick-porous GaN, 100 nm thick planarizing GaN layer, 200 nm thick modified semi-bulk $In_{0.06}Ga_{0.94}N$, (b) High resolution image of a v-defect appearing on the surface originating from the buffer layer, (c) Electron scattering contrast image of the cross-section showing the dislocation propagating through the porous layer and terminating in the v-defect at the surface. Images acquired by Dr. Feng Wu.

After the InGaN regrowth, the sample with the coalesced porous underlayers was characterized using HAADF TEM. Figure 5.3 (a) shows the cross-section of the sample comprised of 2 µm thick UID GaN buffer layers, 800 nm thick, porous GaN layer porosified from the top surface, 100 nm thick planarizing GaN layer, and 200 nm thick modified semi-bulk $In_{0.06}Ga_{0.94}N$. The dislocations seemed to be unaffected by the planar porosification, which is yet to be well understood and requires more experiments. The porous layer seemed to be uniformly porous along the lateral dimension. When patterning into tiles, these substrates will have a uniform porosity under the devices. The study of relaxation of InGaN grown on these modified PS, effect of feature sizes, and device level demonstrations must be pursued on these modified GaN on porous GaN PSs.

C. Modeling the stress state across a tile

The strain state at each point across a tile could not be accessed using the available XRD tool. Considering the mechanical properties of each layer, the relaxation mechanism can be better understood. Study of strain state of patterned films on a rigid substrate can be found in literature [72]. In the current work, the substrate is non-rigid (porous GaN) and the patterned film is also composed of multiple films, hence mechanics of laminated composite plates need to be considered [121]. It was important to know the dependence of lattice constants, elastic constants, and bulk modulus on the mole-fraction of indium. A study of this dependence for the $In_xAl_{1-x}N$ alloy can be found in ref. [122]. The authors found the relationship of these parameters in close agreement with Vegard's law, which made the analysis much simpler. Hence, the using the composite laminates analysis, the elastic constants of the composite film in figure 5.4, could be calculated. To greatly simplify the analysis and demonstrate the approach, the following assumptions were made:

i) Assume the porous GaN layer is isotropic irrespective of the position of analysis

ii) Assume cubic crystal for symmetry

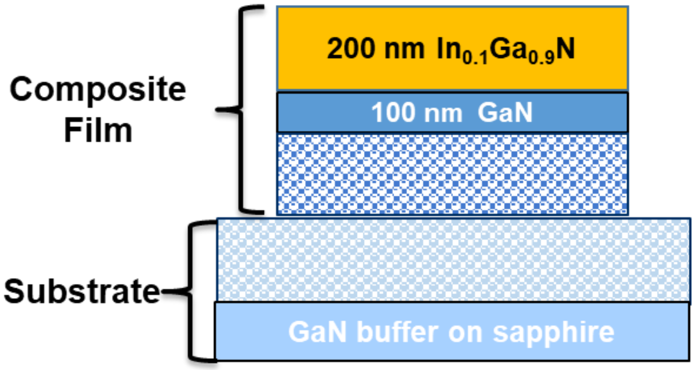

Figure 5.4 The composite film and substrate classification in the epitaxial structure of the GaN on porous GaN tile samples. The total thickness of the porous GaN layer was 800 nm, half of which was considered in the composite film.

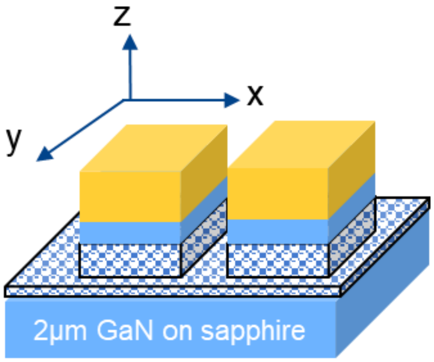

Figure 5.5 The epitaxial structure with labeled axis

The axial nomenclature is shown in figure 5.5. For an orthotropic plate, the normal strain $\mathcal{E}_x$, along the x-axis, can be expressed as:

$$\mathcal{E}_x = \sigma_x/E_x - v_{yx} * \sigma_y/E_y \qquad 5.1$$

where, σ_x and σ_y are normal stresses, E_x and E_y are elastic constants, and v_{yx} is the poisson's ratio. The shear stress τ_{xy}, can be expressed as the product of the shear strain γ_{xy} and shear modulus G_{xy}. Using the elastic constants available in the literature the Young's modulus and poisson's ratio were calculated for $In_{0.1}Ga_{0.9}N$ (using Vegard's law), GaN and porous GaN, assuming cubic symmetry, for simpler analysis [122-123]. Using the composite laminate theory, for multiple laminates with Young's modulus of Y_1, Y_2…, each with a thickness of h_1, h_2…, the resultant Young's modulus of the composite layer can be expressed as:

$$Y_{resultant} = \frac{Y_1 h_1 + Y_2 h_2 \ldots}{h_1 + h_2 \ldots} \tag{5.2}$$

Using the above relation, the Young's modulus of the composite layer and substrate were estimated.

The principal components of biaxial stress, can be expressed as $\sigma_1 = \sigma_x.f(a)$ and $\sigma_2 = \sigma_x.f(b)$, where f(a) and f(b) are the functions of stress distribution along axes a and b, and σ_x is the stress state away from the edge [72]. Using the analysis in reference [72], the formation of an edge along the 'x' axis at a distance 'a' from the edge (maximum dimension = A) between the composite film (f) and substrate (s), leads to a stress variation in film:

$$\sigma_f = \sigma_x\,(1 - e^{-\{2K(A-a)\}^\wedge\frac{1}{2}}) \tag{5.3}$$

where K is the relative rigidity and is defined as:

$$K = Y_s\,(1-v_f)/Y_f(1-v_s) \tag{5.4}$$

for cubic crystals, where, Y_s and Y_f are the young's modulus of the composite film and substrate, respectively, and v_s and v_f are the poisson's ratio of the composite film and substrate, respectively. Hence the effective stress in the film:

$$\sigma = [\tfrac{1}{2}\,\{\sigma_1^2 + \sigma_2^2 + (\sigma_1 - \sigma_2)^2\}]\ ^\wedge\tfrac{1}{2} \tag{5.5}$$

which can be extended to biaxial stress as follows:

$$\sigma = \sigma_x\,\{f^2(a) + f^2(b) - f(a).f(b)\}^\wedge\tfrac{1}{2} \tag{5.6}$$

where, $f(a) = 1 - e^{-(2Ka/\pi h)^\wedge\frac{1}{2}} - e^{-\{2K(A-a)/\pi h\}^\wedge\frac{1}{2}}$ and $f(b) = 1 - e^{-(2Kb/\pi h)^\wedge\frac{1}{2}} - e^{-\{2K(B-b)/\pi h\}^\wedge\frac{1}{2}}$.

Using the above equations, the stress ratio σ/σ_x was plotted across a 10 µm × 10 µm tile patterned composite film with and without porous underlayers, as shown in figure 5.6 (a) and (b), respectively, using MATLAB. It must be noted that this analysis holds true for cubic crystals, and for the most accurate stress state for these epitaxial structures, the relative rigidity for hexagonal lattices must be estimated. From figure 5.6, a lower relative stress can be observed for the sample with porous underlayers, as verified by XRD measurements discussed in chapter 3. For further accuracy, the effect of non-uniform porosity can also be added to this analysis. It must be noted that the relative strain state plotted in figure 5.6, were for the complete composite films and not just the $In_{0.1}Ga_{0.9}N$ layers, making it difficult to directly compare the strain relaxation obtained in this analysis with the measured XRD results.

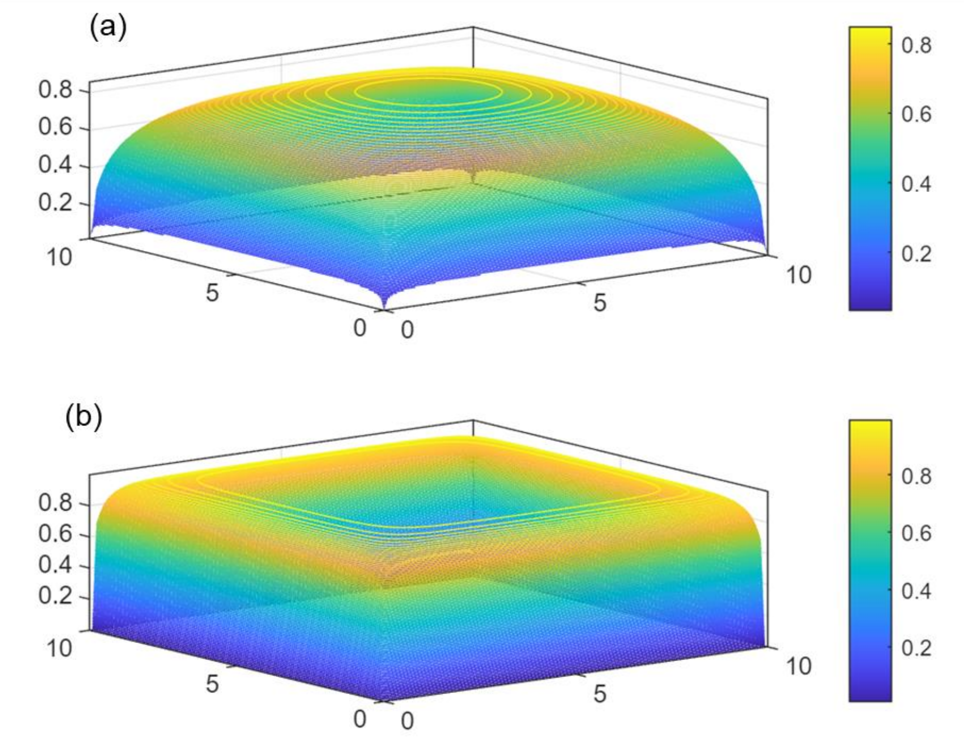

Figure 5.6 The relative stress state of tile patterns sized 10 µm × 10 µm (a) with porous underlayers, (b) without porous underlayers

D. Conclusion

To summarize, a novel porous GaN based compliant PS technology was developed. Porous GaN was utilized as a flexible underlayer, to allow the change in lattice constant of films grown above it. Using sidewall porosification of GaN:Si films, with GaN or InGaN cap layers, the PSs were fabricated following an EC etch. The patterns used to define these sidewalls, were responsible for the axial behavior (uniaxial or biaxial) of the strain relaxation and the pattern dimension determined the degree of relaxation of the films above the porous GaN layer. Hence, micro-meter scale elastic strain relaxation could be obtained. These substrates were universal in nature, allowing relaxation of InGaN and AlGaN films. Using low pressure growth conditions, methods to achieve large area relaxed AlGaN with a fixed lattice constant, was examined. Under atmospheric pressure conditions, growth optimizations were performed for InGaN layers to reduce the size and density of v-defects. Enhanced indium incorporation could be obtained when LED structures with InGaN:Si base layers were grown on these PSs compared to reference GaN on sapphire templates due to a strain relaxation induced reduced lattice mismatch between the InGaN:Si layer and the MQWs. Device demonstrations with LED epitaxial structure emitting in the green wavelength range, indicated the potential of this PS technology for longer wavelength micro-LEDs.

For the upcoming micro-LED display technology, InGaN based blue and green micro-LEDs, and AlInGaP based red micro-LEDs are being considered. To reduce the cost of these displays, aggressive scaling of these devices below 10 µm is necessary. Due to unfavorable material properties, the mature red emitting AlInGaP micro-LEDs suffer from severe EQE degradation with size reduction, hence InGaN based ultra-small micro-LEDs were studied. Using the GaN on porous GaN PS technology, the first red micro-LED sized below 10 µm was demonstrated with measurable on-wafer EQE, paving the pathway for commercialization of this technology. A few methods to improve the current device have also been suggested, which can help in pushing the light output performance of these micro-LEDs.

References

1. S. Nakamura and G. Fasol, *The Blue Laser diode: GaN based light emitters and Lasers*, Springer, (1997)

2. U. K. Mishra, P. Parikh and Yi-Feng Wu, “AlGaN/GaN HEMTs-an overview of device operation and applications,” *Proceedings of the IEEE, vol. 90,* pp. 1022-1031 (2002)

3. U. K. Mishra, L. Shen, T. E. Kazior and Y. Wu, “GaN-Based RF Power Devices and Amplifiers,” *Proceedings of the IEEE, vol. 96,* pp. 287-305 (2008)

4. S. T. Tan, X. W. Sun, H. V. Demir and S. P. DenBaars, “Advances in the LED Materials and Architectures for Energy-Saving Solid-State Lighting Toward Lighting Revolution,” *IEEE Photonics Journal, vol. 4,* pp. 613-619 (2012)

5. X. Long, J. He, J. Zhou, L. Fang, X. Zhou, F. Ren, and T. Xu, “A review on light-emitting diode based automotive headlamps,” *Renewable and Sustainable Energy Reviews, vol. 41*, pp. 29-41 (2015)

6. L. Zhao, S. Zhu, C. Wu, C. Yang, Z. Yu, H. Yang, and L. Liu, “GaN-based LEDs for light communication,” *Sci. China Phys. Mech. Astron., vol. 59,* pp. 107301 (2016)

7. H. Chun, S. Rajbhandari, G. Faulkner, D. Tsonev, E. Xie, J. James, D. McKendry, E. Gu, M. D. Dawson, D. C. O’Brien, *et al.* “LED based wavelength division multiplexed 10 Gb/s visible light communications,” *Lightwave Technol., vol. 34,* pp. 3047–3052.

8. J. J. D. McKendry, R. P. Green, A. E. Kelly, Z. Gong, B. Guilhabert, D. Massoubre, E. Gu, and M. D. Dawson, “High-speed visible light communications using individual pixels in a micro light-emitting diode array,” *IEEE Photonics Technol. Lett., vol. 22,* pp. 1346-1348 (2010)

9. S. Rajbhandari, J. J. D. McKendry, J. Herrnsdorf, H. Chun, G. Faulkner, H. Haas, I. M. Watson, D. O’Brien, and M. D. Dawson, “A review of gallium nitride LEDs for multi-gigabit-per-second visible light data communications,” *Semicon. Sci. Technol., vol. 32*, pp. 023001 (2017)

10. C. A. Mitchell, M. P. Dzakovich, C. Gomez, R. Lopez, J. F. Burr, R. Hernaández, C. Kubota, C. J. Currey, Q. Meng, E. S. Runkle, *et al.* “Light-emitting diodes in horticulture,” *Hortic. Rev., vol. 43,* pp. 1-87 (2015)

11. S. P. DenBaars, D. Feezell, K. Kelchner, S. Pimputkar, C.-C. Pan, C.-C. Yen, S. Tanaka, Y. Zhao, N. Pfaff, R. Farrell, M. Iza, S. Keller, U. K. Mishra, J. S. Speck, and S. Nakamura, "Development of gallium-nitride-based light-emitting diodes (LEDs) and laser diodes for energy-efficient lighting and displays," *Acta Materialia, vol. 61, no. 3*, pp. 945 – 951 (2013)

12. N. G. Yeh, C.-H. Wu, and T. C. Cheng, "Light-emitting diodes—Their potential in biomedical applications," *Renewable and Sustainable Energy Reviews, vol. 14, no. 8*, pp. 2161-2166 (2010)

13. J. Hadi, M. Dunowska, S. Wu, and G. Brightwell, "Control Measures for SARS-CoV-2: A Review on Light-Based Inactivation of Single-Stranded RNA Viruses," *Pathogens, vol. 9, no. 9*, pp. 737 (2020)

14. K. Ding, V. Avrutin, N. Izyumskaya, Ü. Özgür, and H. Morkoç, "Micro-LEDs, a Manufacturability Perspective," *Appl. Sci., vol. 9, no. 6*, pp. 1206 (2019)

15. M. Wong, "Development of Device Technology for Micro-Light-Emitting Diodes," *UC Santa Barbara* (2020)

16. Y. Huang, G. Tan, F. Gou, M. -C. Li, S. -L. Lee, and S. -T. Wu, "Prospects and challenges of mini-LED and micro-LED displays," *J. Soc. Inf. Display, vol. 27*, pp. 387-401 (2019)

17. H. -J Shin, K. -M. Park, S. Takasugi, S. -H. Choi, Y. -S. Jeong, H. -D. Choi, I. -J. Kim, H. -S. Kim, H. -W. Lee, and C. -H. Oh, "Advanced OLED Display Technologies for Large-Size Semi-Flexible TVs," *SID Digest, vol. 47, no. 1*, pp. 609-612 (2016)

18. C. A. Hurni, A. David, M. J. Cich, R. I. Aldaz, B. Ellis, K. Huang, A. Tyagi, R. A. DeLille, M. D. Craven, F. M. Steranka, and M. R. Krames, "Bulk GaN flip-chip violet light-emitting diodes with optimized efficiency for high-power operation," *Appl. Phys. Lett., vol. 106*, pp. 031101 (2015)

19. Q. Lv, J. Liu, C. Mo, J. Zhang, X. Wu, Q. Wu, and F. Jiang, "Realization of Highly Efficient InGaN Green LEDs with Sandwich-like Multiple Quantum Well Structure: Role of Enhanced Interwell Carrier Transport," *ACS Photonics, vol. 6, no. 1*, pp. 130-138 (2018)

20. M. A. Maur, A. Pecchia, G. Penazzi, W. Rodrigues, and A. Carlo, “Efficiency Drop in Green InGaN/GaN Light Emitting Diodes : The Role of Random Alloy Fluctuations”, *Phys. Rev. Lett., vol. 116,* pp. 027401 (2016)

21. K. A. Bulashevich, A. V. Kulik, and S. Y. Karpov, “Optimal ways of colour mixing for high-quality white-light LED sources,” *Phys. Status Solidi A, vol. 212, no. 5,* pp. 914-919 (2015)

22. T. Langer, A. Kruse, F. A. Ketzer, A. Schwiegel, L. Hoffmann, H. Jönen, H. Bremers, U. Rossow, and A. Hangleiter, “Origin of the green gap : Increasing nonradiative recombination in indium-rich GaInN/GaN quantum well structures,” *Phys. Status Solidi C, vol. 8,* pp. 2170 (2011)

23. M. S. Wong, J. A. Kearns, C. Lee, J. M. Smith, C. Lynsky, G. Lheureux, H. Choi, J. Kim, C. Kim, S. Nakamura, J. S. Speck, and S. P. DenBaars, “Improved performance of AlGaInP red micro-light emitting diodes with sidewall treatments”, *Opt. Express, vol. 28, no. 4,* pp. 5787 (2020)

24. H. X. Jiang and J. Y. Lin, “Nitride micro-LEDs and beyond – a decade progress review”, *Opt. Express, vol. 21, no. S3,* pp. A475-A484 (2013)

25. Z. Ma, H. Cao, S. Lin, X. Li, X. Xi, J. Li, and L. Zhao, “Optical and frequency degradation behavior of GaN-based micro-LEDs for visible light communication,” *Opt. Express, vol. 28, no. 9,* pp. 12795-12804 (2020)

26. Paranjpe, J. Montgomery, S. M. Lee, and C. Morath, “Micro-LED Displays: Key Manufacturing Challenges and Solutions,” *SID Symposium Digest of Technical Papers, vol. 49,* pp. 597–600 (2018)

27. D. Hwang, A. Mughal, C. D. Pynn, S. Nakamura, and S. P. DenBaars, “Sustained high external quantum efficiency in ultrasmall blue III-nitride micro-LEDs,” *Appl. Phys. Express, vol. 10,* pp. 032101 (2017)

28. P. Royo, R. P. Stanley, M. Ilegems, K. Streubel, and K. H. Gulden, “Experimental determination of the internal quantum efficiency of AlGaInP microcavity light emitting diodes,” *J. Appl. Phys., vol. 91,* pp. 2563 (2002)

29. V. Cimalla, “Label-Free Biosensors based on III-Nitride semiconductors,” *Springer series on Chemical Sensors and Biosensors (Methods and Applications), vol. 16,* Springer, Cham.(2017)

30. F. M. Steranka, D. C. DeFevre, M. D. Camras, C. -W. Tu, D. K. McElfresh, S. L. Rudaz, L. W. Cook, and W. L. Snyder, “Red AlGaAs light emitting diodes” *Hewlett-Packard Journal, vol. 39, no. 4,* p. 84 (1988)

31. J. M. Dallesasse, N. El-Zein, N. Holonyak Jr., K. C. Hsieh, R. D. Burnham, and R. D. Dupuis, “Environmental degradation of AlGaAs–GaAs quantum-well heterostructures” *J. Appl. Phys., vol. 68,* pp. 2235 (1990)

32. E. F. Schubert, “Light-Emitting Diodes,” *Cambridge University Press,* Cambridge (2006)

33. C. -H. Oh, J.-I. Shim, and D.-S. Shin, “Current and temperature dependent efficiency droops in InGaN-based blue and AlGaInP-based red light-emitting diodes,” *Jpn. J. Appl. Phys., vol. 58,* pp. SCCC08 (2019)

34. K. A. Bulashevich and S. Y. Karpov, “Impact of surface recombination on efficiency of III-nitride light emitting diodes,” *Phys. Status Solidi RRL, vol 10, no. 6,* pp. 480-484 (2016)

35. J. R. Jinscheka, R. Ernib, N. F. Gardnerc, A. Y. Kim, and C. Kisielowski, “Local indium segregation and band gap variations in high efficiency green light emitting InGaN/GaN diodes,” *Solid State Commun., vol. 137, no. 4,* pp. 230 -234 (2006)

36. S. -W. Feng, Y. -C. Cheng, Y. -Y. Chung, C. C. Yang, Y. -S. Lin, C. Hsu, K. -J. Ma, and J. -I. Chyi, “Impact of localized states on the recombination dynamics in InGaN/GaN quantum well structures,” *J. Appl. Phys., vol. 92,* pp. 4441 (2002)

37. J. W. Matthews and A. E. Blakeslee, “Defects in epitaxial multilayers: I. Misfit dislocations,” *J. Cryst. Growth, vol. 27,* pp. 118–125 (1974)

38. D. Holec, P. M. F. J. Costa, M. J. Kappers, and C. J. Humphreys, “Critical thickness calculation for InGaN/GaN,” *J. Cryst. Growth, vol. 303,* pp. 314–317 (2007)

39. A. Even, G. Laval, O. Ledoux, P. Ferret, D. Sotta, E. Guiot, F. Levy, I. C. Robin, and A. Dussaigne, “Enhanced In incorporation in full InGaN heterostructure grown on relaxed InGaN pseudo-substrate,” Appl. Phys. Lett., vol.110, pp. 262103 (2017)

40. Y. Kawaguchi, M. Shimizu, K. Hiramatsu, and N. Sawaki, “ The Composition Pulling Effect in InGaN Growth on the GaN and AlGaN Epitaxial Layers Grown by MOVPE,” *Proceedings of the MRS Symposium, vol. 449* (1996)

41. K. Hiramatsu, Y. Kawaguchi, M. Shimizu, N. Sawaki, T. Zheleva, R. F. Davis, H. Tsuda, W. Taki, N. Kuwano, and K. Oki, "The composition pulling effect in MOVPE grown InGaN on GaN and AlGaN and its TEM characterization," *MRS Internet J. Nitride Semicond. Res., vol. 2, no. 6*, pp. 11 (1997)

42. S. Pereira, M. R. Correia, E. Pereira, K. P. O'Donnel, C. Trager-Cowan, F. Sweeny, and E. Alves, "Compositional pulling effects in $In_xGa_{1-x}N$/GaN layers: A combined depth-resolved cathodoluminescence and Rutherford backscattering/channeling study," *Phys. Rev. B, vol. 64,* pp. 205311 (2001)

43. D. Queren, M. Schillgalies, A. Avramescu, G. Büderl, A. Laubsch, S. Lutgen, U. Strauß, "Quality and thermal stability of thin InGaN films," *J. Cryst. Growth, vol. 311, no. 10,* pp. 2933-2936 (2009)

44. T. Yayama, Y. Kangawa, K. Kakimoto, and A. Koukitu, "Theoretical analyses of In incorporation and compositional instability in coherently grown InGaN thin films," *Phys. Status Solidi C*, vol. 7, no. 7-8, pp. 2249-2251 (2010)

45. A. Dussaigne, F. Barbier, B. Damilano, S. Chenot, A. Grenier, A. M. Papon, B. Samuel, B. Ben Bakir, D. Vaufrey, J. C. Pillet, A. Gasse, O. Ledous, M. Rozhavskaya, and D. Sotta, " Full InGaN red light emitting diodes," *J. Appl. Phys., vol. 128, no. 13,* pp. 135704 (2020)

46. J. Däubler, T. Passow, R. Aidam, K. Köhler, L. Kirste, M. Kunzer, and J. Wagner, "Long wavelength emitting GaInN quantum wells on metamorphic GaInN buffer layers with enlarged in-plane lattice parameter," *Appl. Phys. Lett., vol. 105, no. 11,* pp. 111111 (2014)

47. A. Kobayashi, J. Ohta, and H. Fujioka, "Low temperature epitaxial growth of $In_{0.25}Ga_{0.75}N$ on lattice-matched ZnO by pulsed laser deposition," *J. Appl. Phys., vol. 99*, pp. 123513 (2006)

48. S. -J. Wang, N. Li, E. H. Park, Z. C. Feng, A. Valencia, J. Nause, M. Kane, C. Summers, I. Ferguson, "MOCVD growth of GaN-based materials on ZnO substrates," *Phys. Status Solidi C, vol. 5, no. 6,* pp. 1736–1739 (2008)

49. Y. Lei, J. Xu, K. Zhu, M. He, J. Zhou, Y. Gao, L. Zhang, and Y. Chen, "A GaN-Based LED With Perpendicular Structure Fabricated on a ZnO Substrate by MOCVD," *J. Disp. Technol., vol. 9, no. 5,* pp. 377–381 (2013)

50. T. Ozaki, Y. Takagi, J. Nishinaka, M. Funato, and Y. Kawakami, “Metalorganic vapor phase epitaxy of GaN and lattice-matched InGaN on ScAlMgO4 (0001) substrates,” *Appl. Phys. Express, vol. 7, no. 9,* pp. 091001 (2014)

51. T. Ozaki, M. Funato, and Y. Kawakami, “InGaN-based visible light emitting diodes on ScAlMgO4 (0001) substrates,” *Appl. Phys. Express, vol. 8, no. 6,* pp. 062101 (2015)

52. K. Hestroffer, F. Wu, H. Li, C. Lund, S. Keller, J. S. Speck, and U. K. Mishra, “Relaxed c-plane InGaN layers for the growth of strain-reduced InGaN quantum wells,” *Semicond. Sci. Technol., vol. 30, no. 10,* pp. 105015 (2015)

53. S. Keller, C. Schaake, N. A. Fichtenbaum, C. J. Neufeld, Y. Wu, K. McGroddy, A. David, S. P. DenBaars, C. Weisbuch, J. S. Speck, and U. K. Mishra, “Optical and structural properties of GaN nanopillar and nanostripe arrays with embedded InGaN/GaN multi-quantum wells,” *J. Appl. Phys., vol. 100, no.5,* pp. 054314 (2006)

54. Z. Quan, L. Wang, C. Zheng, J. Liu, and F. Jiang, “Roles of V-shaped pits on the improvement of quantum efficiency in InGaN/GaN multiple quantum well light-emitting diodes,” *J. Appl. Phys., vol. 116, no. 18,* pp. 183107 (2014)

55. Y. H. Ra, R. T. Rashid, X. Liu, J. Lee, and Z. Mi, “Scalable Nanowire Photonic Crystals: Molding the Light Emission of InGaN,” *Adv. Funct. Mater., vol. 27, no. 38,* pp. 1702364 (2017)

56. S. Huang, Y. Zhang, B. Leung, G. Yuan, G. Wang, H. Jiang, Y. Fan, Q. Sun, J. Wang, K. Xu, and J. Han, “Mechanical properties of nanoporous GaN and its application for separation and transfer of GaN thin films,” *ACS Appl. Mater. Interfaces, vol. 5, no. 21,* pp. 11074 (2013).

57. S. Fakiri, A. Montagne, K. Rahmoun, A. Iost, and K. Ziouche, “Mechanical properties of porous silicon and oxidized porous silicon by nanoindentation technique,” *Mater. Sci. Eng. A, vol. 711,* pp. 470-475 (2018)

58. Y. Zhang, S. W. Ryu, C. Yerino, B. Leung, Q. Sun, H. Cao, and J. Han, “A conductivity-based selective etching for next generation GaN devices,” *Phys. Status Solidi B, vol. 247, no. 7,* pp. 1713-1716 (2010)

59. S. S. Pasayat, C. Gupta, D. Acker-James, D. A. Cohen, S. P. DenBaars, S. Nakamura, S. Keller, and U. K. Mishra, "Fabrication of relaxed InGaN pseudosubstrates composed of micron-sized pattern arrays with high fill factors using porous GaN," *Semicond. Sci. Technol., vol. 34, no. 11,* pp. 115020 (2019)

60. S. S. Pasayat, C. Gupta, Y. Wang, S. P. DenBaars, S. Nakamura, S. Keller, and U. K. Mishra, "Compliant micron-sized patterned InGaN pseudo-substrates utilizing porous GaN," *Materials, vol. 13, no. 1,* pp. 213 (2020)

61. S. S. Pasayat, C. Gupta, M. S. Wong, Y. Wang, S. Nakamura, S. P. DenBaars, S. Keller, and U. K. Mishra, "Growth of strain-relaxed InGaN on micrometer-sized patterned compliant GaN pseudo-substrates," *Appl. Phys. Lett., vol. 116, no. 11,* pp. 111101 (2020)

62. S. S. Pasayat, R. Ley, C. Gupta, M. S. Wong, C. Lynsky, Y. Wang, M. J. Gordon, S. Nakamura, S. P. DenBaars, S. Keller, and U. K. Mishra, "Color-tunable < 10 µm square InGaN micro-LEDs on complaint GaN-on-porous GaN pseudo-substrates," *Appl. Phys. Lett., vol. 117, no. 6,* pp. 061105 (2020)

63. S. S. Pasayat, N. Hatui, W. Li, C. Gupta, S. Nakamura, S. P. DenBaars, S. Keller, and U. K. Mishra, "Method of growing elastically relaxed crack-free AlGaN on GaN as substrates for ultra-wide bandgap devices using porous GaN," *Appl. Phys. Lett., vol. 117, no. 6,* pp. 062102 (2020)

64. S. S. Pasayat, C. Gupta, M. S. Wong, R. Ley, M. J. Gordon, S. P. DenBaars, S. Nakamura, S. Keller, and U. K. Mishra, "Demonstration of ultra-small (< 10 µm) 632 nm red InGaN micro-LEDs with useful on-wafer external quantum efficiency (> 0.2%) for mini-displays," *Appl. Phys. Express, vol. 14, no. 1,* pp. 011004 (2021)

65. C. Zhang, G. Yuan, A. Bruch, K. Xiong, H. X. Tang, and J. Han, "Towards Quantitative Electrochemical Nanomachining of III-Nitrides," *J. Electrochem. Soc., vol. 165, no. 10,* pp. E513 (2018)

66. C. Gupta, Y. Tsukada, B. Romanczyk, S. S. Pasayat, D. A. James, E. Ahmadi, S. Keller, and U. K. Mishra, "First demonstration of improvement in hole conductivity in c-plane III-Nitrides through application of uniaxial strain," *Jpn. J. Appl. Phys., vol. 58, no. 3,* pp. 030908 (2019)

67. W. Li, S. S. Pasayat, M. Guidry, B. Romanczyk, X. Zheng, C. Gupta, N. Hatui, S. Keller, and U. K. Mishra, "First experimental demonstration and analysis of

electrical transport characteristics of a GaN-based HEMT with a relaxed InGaN channel," *Semicond. Sci. Technol., vol. 35, no. 7,* pp. 075007 (2020)

68. C. Zhang, S. H. Park, D. Chen, D. -W. Lin, W. Xiong, H. -C. Kuo, C. -F. Lin, H. Cao, and J. Han, "Mesoporous GaN for Photonic Engineering – Highly Reflective GaN Mirrors as an Example," *ACS Photonics, vol. 2, no. 7,* pp. 980-986 (2015)

69. K. Pantzas, Y. E. Gmili, J. Dickerson, S. Gautier, L. Largeau, O. Mauguin, G. Patriarche, S. Suresh, T. Moudakir, C. Bishop, A. Ahaitouf, T. Rivera, C. Tanguy, P. L. Voss, and A. Ougazzaden, "Semibulk InGaN: A novel approach for thick, single phase, epitaxial InGaN layers grown by MOVPE," *J. Cryst. Growth, vol. 370*, pp. 57-62 (2013)

70. D. Won, X. Weng, and J. M. Redwing, "Effect of indium surfactant on stress relaxation by V-defect formation in GaN epilayers grown by metalorganic chemical vapor deposition," *J. Appl. Phys., vol. 108, no. 9,* pp. 093511 (2010)

71. X. H. Wu, C. R. Elsass, A. Abare, M. Mack, S. Keller, P. M. Petroff, S. P. DenBaars, and J. S. Speck, "Structural origin of V-defects and correlation with localized excitonic centers in InGaN/GaN multiple quantum wells," *Appl. Phys. Lett., vol. 72, no. 6*, pp. 692 (1988)

72. A. Fischer, H. Kuhne, B. Roos, and H. Richter, "Elastic strain relaxation in patterned heteroepitaxial structures," *Semicond. Sci. Technol., vol. 9, no. 12*, pp. 2195–2198 (1994)

73. H. K. Cho, J. Y. Lee, C. S. Kim, G. M. Yang, N. Sharma, and C. Humphreys, "Microstructural characterization of InGaN/GaN multiple quantum wells with high indium composition," *J. Cryst. Growth, vol. 231, no. 4,* pp. 466-473 (2001)

74. S. L. Rhode, W. Y. Fu, M. A. Moram, F. C.-P. Massabuau, M. J. Kappers, C. McAleese, F. Oehler, C. J. Humphreys, R. O. Dusane, and S.–L. Sahonta, "Structure and strain relaxation effects of defects in $In_xGa_{1-x}N$ epilayers," *J. Appl. Phys., vol. 116,* pp. 103513 (2014)

75. C. -K. Li, C. -K. Wu, C. -C. Hsu, L. -S. Lu, H. Li, T. -C. Lu, and Y. -R. Wu, "3D numerical modeling of the carrier transport and radiative efficiency for InGaN/GaN light emitting diodes with V- shaped pits," *AIP Adv., vol. 6, no. 5,* pp. 055208 (2016)

76. X. Jiang, C. Zheng, C. Mo, X. Wang, J. Zhang, Z. Quan, J. Liu, and F. Jiang, “Study on the performance of InGaN based green LED by designing different preparing layers,” *Opt. Mater., vol. 89,* pp. 505-511 (2019)

77. F. Jiang, J. Zhang, L. Xu, J. Ding, G. Wang, X. Wu, X. Wang, C. Mo, Z. Quan, X. Guo, C. Zheng, S. Pan, and J Liu, “Efficient InGaN-based yellow-light-emitting diodes,” *Photonics Res., vol. 7, no. 2,* pp. 144 (2019)

78. L. C. Le, D. G. Zhao, D. S. Jiang, L. Li, L. L. Wu, P. Chen, Z. S. Liu, Z. C. Li, Y. M. Fan, J. J. Zhu, H. Wang, S. M. Zhang, and H. Yang, “Carriers capturing of v-defect and its effect on leakage current and electroluminescence in InGaN-based light-emitting diodes,” *Appl. Phys. Lett., vol. 101, no. 25,* pp. 252110 (2012)

79. A. I. Alhassan, R. M. Farrell, B. Saifaddin, A. Mughal, F. Wu, S. P. DenBaars, S. Nakamura, and J. S. Speck, “High luminous efficacy green light emitting diodes with AlGaN cap layer,” *Opt. Express, vol. 24, no. 16,* pp. 17868 (2016)

80. C. Gupta, C. Lund, S. H. Chan, A. Agarwal, J. Liu, Y. Enatsu, S. Keller, and U. K. Mishra, “In Situ Oxide, GaN Interlayer-Based Vertical Trench MOSFET (OG-FET) on Bulk GaN substrates,” *IEEE Electron Device Lett., vol. 38, no. 3*, pp. 353–355 (2017)

81. F. Olivier, A. Daami, C. Licitra, and F. Templier, “Shockley-Read-Hall and Auger non-radiative recombination in GaN based LEDs : A size effect study,”*Appl. Phys. Lett., vol. 111, no. 2,* pp. 022104 (2017)

82. P. Tian, J. J. D. McKendry, Z. Gong, B. Guilhabert, I. M. Watson, E. Gu, Z. Chen, G. Zhang, and M. D. Dawson, “Size dependent efficiency and efficiency droop of blue InGaN micro-light emitting dodes,” *Appl. Phys. Lett., vol. 101, no. 23,* pp. 231110 (2012)

83. J. M. Smith, R. Ley, M. S. Wong, Y. H. Baek, J. H. Kang, C. H. Kim, M. J. Gordon, S. Nakamura, J. S. Speck, and S. P. DenBaars, “Comparison of size-dependent characteristics of blue and green InGaN micro-LEDs down to 1μm in diameter” *Appl. Phys. Lett. 116, no. 7,* pp. 071102 (2020)

84. T. Mukai, M. Yamada, and S. Nakamura, “Characteristics of InGaN-Based UV/Blue/Green/Amber/Red Light-Emitting Diode,” *Jpn. J. Appl. Phys., vol 38, no. 7R,* pp. 3976 (1999)

85. M. Funato, M. Ueda, Y. Kawakami, Y. Narukawa, T. Kosugi, M. Takahashi,

and T. Mukai, “Blue, Green and Amber InGaN/GaN Light Emitting Diodes on Semipolar {11-22} GaN Bulk Substrates,” *Jpn. J. Appl. Phys., vol. 45, no. 7L,* pp. L659 (2006)

86. M. H. Crawford, “LEDs for Solid-State Lighting: Performance Challenges and Recent Advances,” *IEEE J. Sel. Top. Quantum Electron., vol. 15, no. 4,* pp. 1028 (2009)

87. S. S. Konoplev, K. A. Bulashevich, and S. Y. Karpov, “From large size to micro-LEDs: Scaling trends revealed by modeling,” *Phys. Status Solidi A, vol. 215, no. 10,* pp. 1700508 (2018)

88. Z. Gong, S. Jin, Y. Chen, J. McKendry, D. Massoubre, I. M. Watson, E. Gu, and M. D. Dawson, “Size-dependent light output, spectral shift, and self-heating of 400 nm InGaN light-emitting diodes,” *J. Appl. Phys., vol. 107, no. 1,* pp. 013103 (2010)

89. M. S. Wong, D. Hwang, A. I. Alhassan, C. Lee, R. Ley, S. Nakamura, and S. P. DenBaars, “High efficiency of III-nitride micro-light emitting diodes by sidewall passivation using atomic layer deposition,” *Opt. Express, vol. 26, no. 16,* pp. 21324 (2018)

90. S. P. Chang, C. H. Wang, C. H. Chiu, J. C. Li, Y. S. Lu, Z. Y. Li, H. C. Yang, H. C. Kuo, T. C. Lu, and S. C. Wang, “Characteristics of efficiency droop in GaN-based light emitting diodes with an insertion layer between the multiple quantum wells and n-GaN layer,” *Appl. Phys. Lett., vol. 97, no. 25,* pp. 251114 (2010)

91. M. Kneissl, T. Y. Seong, J. Han, and H. Amano, “The emergence and prospects of deep-ultraviolet light-emitting diode technologies,” *Nat. Photonics, vol. 13,* pp. 233–244

92. H. Amano, Y. Baines, E. Beam, M. Borga, T. Bouchet, P. R. Chalker, M. Charles, K. J. Chen, N. Chowdhury, R. Chu, C. D. Santi, M. M. D. Souza, S. Decoutere, L. D. Cioccio, B. Eckardt, T. Egawa, P. Fay, J. J. Freedsman, L. Guido, O. Hberlen, G. Haynes, T. Heckel, D. Hemakumara, P. Houston, J. Hu, M. Hua, Q. Huang, A. Huang, S. Jiang, H. Kawai, D. Kinzer, M. Kuball, A. Kumar, K. B. Lee, X. Li, D. Marcon, M. März, R. McCarthy, G. Meneghesso, M. Meneghini, E. Morvan, A. Nakajima, E. M. S. Narayanan, S. Oliver, T. Palacios, D. Piedra, M. Plissonnier, R. Reddy, M. Sun, I. Thayne, A. Torres, N. Trivellin, V. Unni, M. J. Uren, M. V. Hove, D. J. Wallis, J. Wang, J. Xie, S. Yagi, S. Yang, C. Youtsey, R. Yu, E. Zanoni, S. Zeltner, and Y. Zhang, “The 2018 GaN power electronics roadmap,” *J. Phys. D, vol. 51, no. 16,* pp. 163001 (2018)

93. K. Ban, J. Yamamoto, K. Takeda, K. Ide, M. Iwaya, T. Takeuchi, S. Kamiyama, I. Akasaki, and H. Amano, “Internal quantum efficiency of whole-composition-range AlGaN multiquantum wells,” *Appl. Phys. Express, vol. 4, no. 5,* pp. 052101 (2011).

94. O. Reentilä, F. Brunner, A. Knauer, A. Mogilatenko, W. Neumann, H. Protzmann, M. Heuken, M. Kneissl, M. Weyers, and G. Tränkle, “Effect of the AlN nucleation layer growth on AlN material quality,” *J. Cryst. Growth 310, no. 23,* pp. 4932–4934 (2008)

95. K. Ito, K. Hiramatsu, H. Amano, and I. Akasaki, “Preparation of $Al_xGa_{1-x}N$/ GaN heterostructure by MOVPE,” *J. Cryst. Growth, vol. 104, no. 2,* pp. 533–538 (1990)

96. J.-M. Bethoux, P. Vennéguès, F. Natali, E. Feltin, O. Tottereau, G. Nataf, P. De Mierry, and F. Semond, “Growth of high quality crack-free AlGaN films on GaN templates using plastic relaxation through buried cracks,” *J. Appl. Phys, vol. 94, no. 10,* pp. 6499 (2003)

97. T. Wang, J. Bai, P. J. Parbrook, and A. G. Cullis, “Air-bridged lateral growth of an $Al_{0.98}Ga_{0.02}N$ layer by introduction of porosity in an AlN buffer,” *Appl. Phys. Lett., vol. 87, no. 15,* pp. 151906 (2005)

98. R. S. Qhalid Fareed, V. Adivarahan, C. Q. Chen, S. Rai, E. Kuokstis, J. W. Yang, M. A. Khan, J. Caissie, and R. J. Molnar, “Air-bridged lateral growth of crack-free $Al_{0.24}Ga_{0.76}N$ on highly relaxed porous GaN,” *Appl. Phys. Lett., vol. 84, no. 5,* pp. 696 (2004)

99. M. A. Bergmann, J. Enslin, R. Yapparov, F. Hjort, B. Wickman, S. Mercinkevičius, T. Wernicke, M. Kneissl, and Å. Haglund, “Electrochemical etching of AlGaN for the realization of thin-film devices,” *Appl. Phys. Lett., vol. 115, no. 18,* pp. 182103 (2019)

100. R. T. Bondokov, S. G. Mueller, K. E. Morgan, G. A. Slack, S. Schujman, M. C. Wood, J. A. Smart, and L. J. Schowalter, “Large area AlN substrates for electronic applications: An industrial perspective,” *J. Cryst. Growth, vol. 310, no. 17,* pp. 4020–4026 (2008)

101. C. H. Chen, H. Liu, D. Steigerwald, W. Imler, C. P. Kuo, M. G. Craford, M. Ludowise, S. Lester, and J. Amano, “A study of parasitic reactions between NH_3 and TMGa or TMAl,” *J. Electron. Mater., vol. 25,* pp. 1004–1008 (1996)

102. J. Han, J. J. Figiel, M. H. Crawford, M. A. Banas, M. E. Bartram, R. M. Biefeld, Y. K. Song, and A. V. Nurmikko, "OMVPE growth and gas-phase reactions of AlGaN for UV emitters," *J. Cryst. Growth, vol. 195, no. 1-4,* pp. 291–296 (1998)

103. K. Matsumoto and A. Tachibana, "Growth mechanism of atmospheric pressure MOVPE of GaN and its alloys: Gas phase chemistry and its impact on reactor design*," J. Cryst. Growth, vol. 272, no. 1-4,* pp. 360–369 (2004)

104. D. Kapolnek, S. Keller, R. Vetury, R. D. Underwood, P. Kozodoy, S. P. DenBaars, and U. K. Mishra, "Anisotropic epitaxial lateral growth in GaN selective area epitaxy," *Appl. Phys. Lett., vol. 71, no. 9,* pp. 1204 (1997)

105. B. Beaumont, P. Vennéguès, and P. Gibart, "Epitaxial Lateral Overgrowth of GaN," *Phys. Status Solidi B, vol. 227, no. 1*, pp. 1–43 (2001)

106. Z. Chen, Y. Pei, S. Newman, D. Brown, R. Chung, S. Keller, S. P. DenBaars, S. Nakamura, and U. K. Mishra, "Growth of AlGaN/GaN/AlGaN double heterojunction field-effect transistors and the observation of a composition pulling effect," *Appl. Phys. Lett., vol. 94, no. 17,* 171117 (2009)

107. W. D. Nix and B. M. Clemens, "Crystallite coalescence: A mechanism for intrinsic tensile stresses in thin films," *J. Mater. Res., vol. 14, no. 8,* pp. 3467–3473 (1999)

108. A. Bell, R. Liu, U. K. Parasuraman, F. A. Ponce, S. Kamiyama, H. Amano, and I. Akasaki, "Spatial variation of luminescence form AlGaN grown by facet controlled epitaxial lateral overgrowth," *Appl. Phys. Lett., vol. 85, no. 16,* pp. 3417 (2004)

109. D. M. Follstaedt, A. A. Allerman, S. R. Lee, J. R. Michael, K. H. A. Bogart, M. H. Crawford, and N. A. Missert, "Dislocation reduction in AlGaN grown on patterned GaN," *J. Cryst. Growth, vol. 310, no. 4,* pp. 766–776 (2008)

110. X. A. Cao, S. J. Pearton, A. P. Zhang, G. T. Dang, F. Ren, R. J. Shul, L. Zhang, R. Hickman, and J. M. Van Hove, "Electrical effects of plasma damage in p-GaN," *Appl. Phys. Lett., vol. 75, no. 17,* pp. 2569 (1999)

111. K. Pantzas, Y. Gmili, J. Dickerson, S. Gautier, L. Largeau, O. Mauguin, G. Partriarche, S. Suresh, T. Moudakir, C. Bishop, A. Ahaitouf, T. Rivera, C. Tanguy, P. L. Voss, and A. Ougazaden, “Semibulk InGaN : A novel approach for thick, single phase, epitaxial InGaN layers grown by MOVPE,” *J. Cryst. Growth, vol. 370, no. 4*, pp. 57-62 (2013)

112. R. C. White, M. Khoury, F. Wu, S. Keller, M. Rozhavskaia, D. Sotta, S. Nakamura, and S. P. DenBaars, “MOCVD growth of thick V-pit free InGaN films on semi-relaxed InGaN substrates,” *Semicond. Sci. Technol., vol. 36, no. 1*, pp. 015011 (2020)

113. R. Czernecki, S. Kret, P. Kempisty, E. Grzanka, J. Plesiewicz, G. Targowski, S. Grzanka, M. Bilska, J. Smalc-Koziorowska, S. Krukowski, T. Suski, P. Perlin, and M. Leszczynski, “Influence of hydrogen and TMIn on indium incorporation in MOVPE growth of InGaN layers,” *J. Cryst. Growth, vol. 402*, pp. 330-336 (2014)

114. S. Saito, R. Hashimoto, J. Hwang, and S. Nunoue, “InGaN Light Emitting Diodes on c-Face Sapphire Substrates in Green Gap spectral range,” *Appl. Phys. Lett., vol. 6, no. 11*, pp. 111004 (2013)

115. J. Hwang, R. Hashimoto, S. Saito, and S. Nunoue, “Effects of local structure on optical properties in green-yellow InGaN/GaN quantum wells”, *Proc. SPIE Opto, Gallium Nitride Materials and Devices VIII, vol. 8625*, pp. 86251G (2013)

116. J. Hwang, R. Hashimoto, S. Saito, and S. Nunoue, “Development of InGaN-based red LED grown on (0001) polar surface,” *Appl. Phys. Express, vol. 7, no. 7*, pp. 071003 (2014)

117. D. Iida, Z. Zhuang, P. Kirilenko, M. Velazquez-Rizo, M. A. Najmi, and K. Ohkawa, “633-nm InGaN-based red LEDs grown on thick underlying GaN layers with reduced in-plane residual stress,” *Appl. Phys. Lett. 116*, 162101 (2020)

118. M. M. Braun and L. Pilon, “Effective optical properties of non-absorbing nanoporous thin films,” *Tin Solid Films, vol. 496, no. 2*, pp. 505-514 (2006)

119. G. Yu, G. Wang, H. Ishikawa, M. Umeno, T. Soga, T. Egawa, J. Watanabe, and T. Jimbo, “Optical properties of wurtzite structure GaN on sapphire around fundamental absorption edge (0.78-4.77 eV) by spectroscopic ellipsometry and the optical transmission method,” *Appl. Phys. Lett., vol. 70, no. 24*, pp. 3209 (1997)

120. R. T. Ley, J. M. Smith, M. S. Wong, T. Margalith, S. Nakamura, S. P. DenBaars, and M. J. Gordon, "Revealing the importance of light extraction efficiency in InGaN/GaN microLEds via chemical treatment and dielectric passivation," *Appl. Phys. Lett., vol. 116, no. 25*, pp. 251104 (2020)

121. A. T. Nettles, "Basic mechanics of Laminated Composite Planes," *NASA Reference Publication 1351* (1994)

122. M. -Y. Xie, F. Tasnádi, I. A. Abrikosov, L. Hultman, and V. Darakchieva, "Elastic constants, composition, and piezoelectric polarization in $In_xAl_{1-x}N$: From ab initio calculation to experimental implications for the applicability of Vegard's rule," *Phys. Rev. B, vol. 86, no. 15*, pp. 155310 (2012)

123. H. Qin, X. Luan, C. Feng, D. Yang, and G. Zhang, "Mechanical, Thermodynamic and Electronic Properties of wurtzite and zinc-blende GaN crystals," *Materials, vol.10*, pp. 1419 (2017)